Investigation of Ni_2MnGa based Shape Memory Alloys

by

Kristin Fröhlich

A Master's Thesis

Submitted in partial fulfilment of the requirements

for the award of

Master of Philosophy of Loughborough University

April 08, 2004

Abstract

Compounds with the general composition $Ni_{2+x}Mn_{1-x}Ga$ belong to the group of ferromagnetic shape memory alloys. These materials have recently attracted a considerable amount of interest due to their potential for applications. Ferromagnetic shape memory alloys, in contrast to conventional shape memory materials, offer the possibility to initiate a change of shape with the application of an external magnetic field of modest magnitude in addition to shape changes induced via a shift in temperature.

In this thesis the magnetic and crystallographic properties of $Ni_{2+x}Mn_{1-x}Ga$ alloys are investigated within the range $0 < x < 0.17$. Structural investigations using both X-ray as well as neutron scattering have been carried out. The low temperature phase has been determined and structural information has been obtained within the transition region for the first time. Magnetic properties have been investigated using a SQUID magnetometer within the temperature range of T = 2 K to 360 K and using magnetic fields up to 5.5 Tesla. The locations of phase transitions were investigated using DSC and resistivity measurements for both heating as well as cooling. The composition dependence of the martensitic and ferromagnetic transition temperatures have been confirmed. The first order nature of the martensitic phase transformation has been confirmed in DSC, magnetisation and resistivity measurements.

Some results of this thesis have already been used in the following publications:

- S. Becker, P.J. Brown, B. Dennis, K. Fröhlich, T. Kanomata, M. Matsumoto, K.-U. Neumann, B. Ouladdiaf, J. Rasch, N. Steinke, T. Stephens, O. Unverdi, K.R.A. Ziebeck, Int. J. Appl. Electrom. Mech., Proceedings of 1st INABIO, Sendai, Japan, 2004, (submitted for publication)

- K. Fröhlich, B. Dennis, T. Kanomata, M. Matsumoto, K.- U. Neumann, K. R. A. Ziebeck, Int. J. Appl. Electrom. Mech., Proceedings of 1st INABIO, Sendai, Japan, 2004, (submitted for publication)

- K.-U. Neumann, K.R.A. Ziebeck, K. Fröhlich, T. Hickel, P.J. Brown, B. Ouladdiaf, Proceedings of 15th Intern. Summer School of Condens. Matter Physics, Bialowieza, Poland, 2003, K. Perzynska, L. Dobrzynski (editors)

Table of Content

2) Introduction

Ferromagnetic shape memory materials (SMM) have recently attracted considerable interest as they are promising candidates for several new and exciting applications e.g. in medicine. The interest in shape memory alloys (SMA) arises due to their ability to remember the shape which they have had at higher temperatures after having been cooled down below the martensitic transformation temperature T_M and deformed. As indicated above the material undergoes a martensitic phase transformation. Huge changes in the lengths of cell parameters occur at this transformation. Although the lattice constants change there is almost no change in the volume of the unit cell [1]. The martensitic phase transformation is a 1^{st} order phase transition and it is fully reversible. Furthermore for materials of composition Ni_2MnGa the phase transformation can be cycled many times without a degradation of the sample, even for bulk material and single crystals [2].

Compared to ordinary shape memory alloys ferromagnetic SMAs have the advantage that the martensitic phase transformation may be controlled by the application of an external magnetic field. This yields a wider range of possibilities for applications, for example in the area of medicine, where a change of temperature is not always feasible. This is the case for a device which has been implanted inside a patient. Here a magnetic field of modest magnitude could be used for switching such a device. Furthermore since temperature changes are intrinsically slow a change of the external field can affect a form change much faster than a martensitic phase transformation driven by a change of temperature.

In this thesis ferromagnetic SMAs of composition $Ni_{2+x}Mn_{1-x}Ga$ ($0 < x < 0.2$) will be discussed. Ni_2MnGa was first discovered by Webster et al. [3]. The structure of pure Ni_2MnGa, the various phases occurring as a function of temperature and the magnetic properties have recently been clarified by P. J. Brown et al. [4]. The phase diagram of $Ni_{2+x}Mn_{1-x}Ga$ with increasing Ni-content in the region of $0 < x < 0.2$ has been determined by Matsumoto et al. [5]. With x increasing the martensitic transition temperature increases and the magnetic transition temperature decreases. They merge for $x = 0.18$.

Magnetisation measurements, differential scanning calorimetry (DSC) and electric resistance measurements have been carried out on samples of composition $Ni_{2+x}Mn_{1-x}Ga$ ($x = 0.05, 0.10, 0.17$) to determine the martensitic and magnetic transition temperatures. X-ray and neutron diffraction experiments have been undertaken in order to investigate the structure of the alloys at different temperatures and investigate the martensitic phase transition.

A brief, and simplified, description of the shape memory effect will be given next in an attempt to illustrate the main features. The description is aimed at indicating the important characteristics for the experimental investigations which form the basis of this thesis.

2.1) The Shape Memory Effect and the Martensitic Phase Transformation

As discussed in the previous section materials exhibiting the shape memory effect are able to remember the shape they have had prior to a deformation. The necessary condition for the occurrence of the shape memory effect is the presence of a martensitic phase transition. The characteristic of this kind of crystallographic phase transition is that it is diffusionless. Large changes in the unit cell are taking place but at the same time there are no changes in the volume of the unit cell. This feature distinguishes martensitic materials from other materials with crystallographic phase transitions. Figure (2.1) illustrates how the shape memory effect is being used in industry for an application in telecommunication. Here the shape memory alloy has been trained to be in the form of an antenna to be used on a satellite.

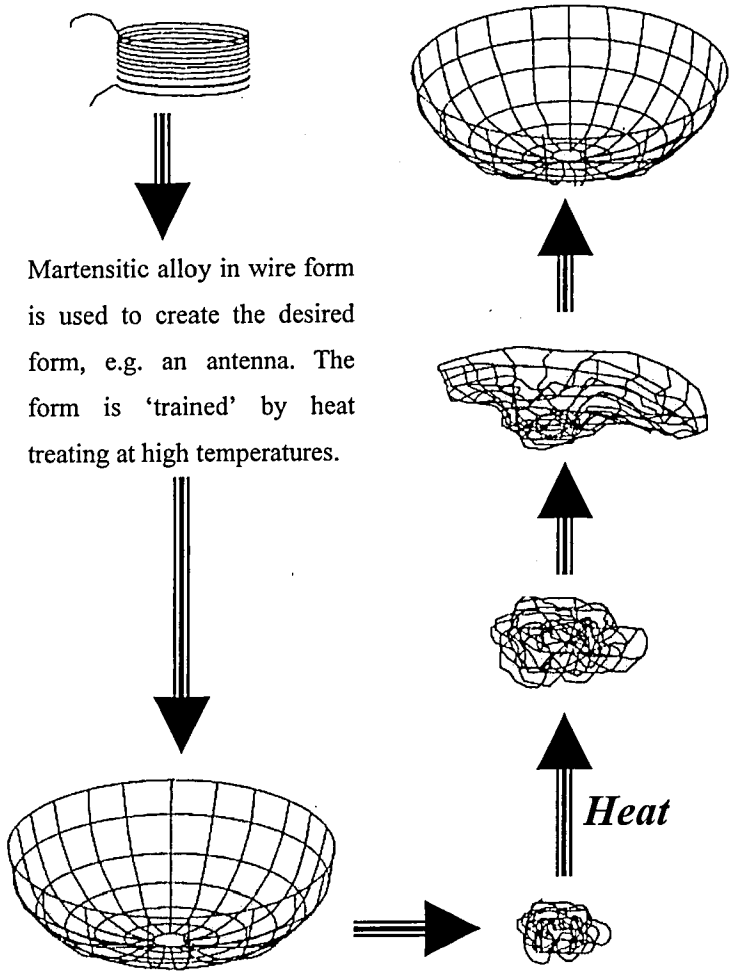

Martensitic alloy in wire form is used to create the desired form, e.g. an antenna. The form is 'trained' by heat treating at high temperatures.

The shape of the antenna is fully recovered once the transformation is completed. This is the case whenever all parts of the wire have attained a temperature above the martensitic phase transition temperature.

When heat is inputted into the system and when the temperature is raised above the martensitic phase transition temperature the material remembers its original shape (i.e. the form of the antenna) and reverts back to this form. The form transformation does not require the input of force from any external source.

Below the martensitic phase transition temperature the antenna can be deformed (e.g. it can be compressed into a small volume for transport into outer space) and stored in a satellite. This form is stable as long as the temperature is kept below the martensitic phase transition temperature.

Figure 2.1

Illustration of the behaviour of a shape memory alloy in a practical application. Here the use of a shape memory alloy as an antenna for a satellite is being considered. It has the particular advantage of allowing transport in a compact form and then, in outer space, it enables a form change without the need for motors. The illustration is taken from [2, 6].

The principle of the shape memory effect is illustrated in figure (2.3). The mechanism is described using a two-dimensional unit cell. At high temperatures the structure is considered to be represented by a square unit cell, as shown in figure (2.2a). As the temperature is lowered below the martensitic phase transformation temperature T_M, the crystallographic structure changes. The unit cell deforms to become rectangular, figure (2.2b). This happens either by shrinking the top and the bottom part and simultaneously extending the left and right sides of the unit cell or vice versa, i.e. by shrinking the left and right hand side and simultaneously extending the top and bottom part of the unit cell. Thus at low temperatures two crystallographic domains develop.

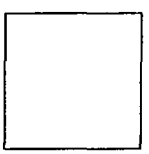

Figure 2.2a
Unit cell of the high temperature 'square' phase

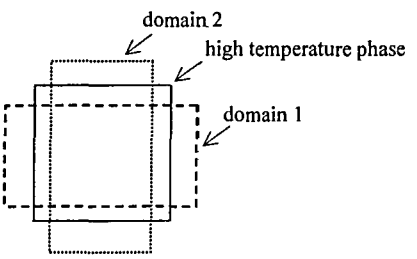

Figure 2.2b
Low temperature 'rectangular' phase. The rectangle can be deformed by either elongation of the square to the left and right (dashed rectangle) or, alternatively, to the top and bottom (dotted rectangle).

In principle, different parts of the crystal will develop into different crystallographic domains. The various domains are expected to occur with equal probabilities. In the low temperature phase the material may be deformed by the application of a force. The force causes the crystallographic domains to align. As the change of the unit cell

parameters may be large, a redistribution of crystallographic domains yields a macroscopic change of shape. If the temperature is kept below T_M this form change is permanent and the domain distribution is stable. If the material is heated above T_M it remembers the shape it has had before and it reverts back to its original form. This occurs as all rectangles revert back to their cubic form, which is independent of the orientation in the low temperature martensitic phase.

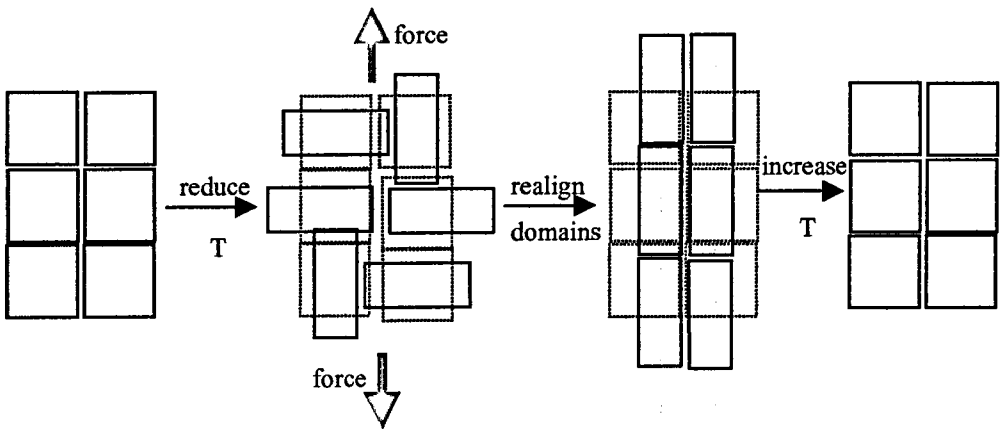

Figure 2.3
Illustration of one possible transformation mechanism for shape memory alloys. Within the low temperature (martensitic) phase the applied force is able to change the crystallographic domain distribution. Thus a macroscopic change of shape occurs. If the deformed material is warmed up again above the martensitic phase transition and the material reverts back to the square shape the sample is changed back to its original form. The illustration is taken from [2].

This simple model illustrated some essential features of SMAs. In order to understand the shape memory effect in Ni_2MnGa alloys it is important to establish the structural aspects of the alloys as well as details in the transition region, i.e. for T close to the martensitic phase transition temperature T_M.

References:

[1] P. J. Brown, B. Dennis, J. Crangle, T. Kanomata, M. Matsumoto, K.-U. Neumann, L. M. Justham, K. R. A. Ziebeck, J. Phys.: Condens. Matter **16**, 2004, 65-75

[2] K.-U. Neumann, K.R.A. Ziebeck, K. Fröhlich, T. Hickel, P.J. Brown, B. Ouladdiaf, Proceedings of 15th Intern. Summer School of Condens. Matter Physics, Bialowieza, Poland, 2003, K. Perzynska, L. Dobrzynski (editors)

[3] P. J. Webster, K. R. A. Ziebeck, S. L. Town, M. S. Peak, Phil. Mag. **B**, 1984, 49, 295-310

[4] P. J. Brown, J. Crangle, T. Kanomata, M. Matsumoto, K.-U. Neumann, B. Ouladdiaf, K. R. A. Ziebeck, J. Phys.: Condensed Matter **14**, 2002, 10159-10171

[5] M. Matsumoto, T. Takagi, T. Kanomata, N. Muramatsu, A. N. Vasil'ev, Mater. Science and Engineering **A273-275**, 1999, 326-328

[6] Shape Memory Materials: K. Otsuka, C.M. Wayman, Cambridge University Press, 1998

3) Theoretical Background and Experimental Set-up

3.1) Sample Preparation

Samples have been prepared using the following procedure: High purity metals of 3N purity have been used for preparing alloys of composition $Ni_{2.17}Mn_{0.83}Ga$, $Ni_{2.10}Mn_{0.90}Ga$ and $Ni_{2.05}Mn_{0.95}Ga$. The ingredients were weighed out with a precision of 0.00001 g. They were melted under a reduced atmosphere in an argon arc furnace. The weight loss after melting for each compound is listed below:

Composition	weight loss	sample size
$Ni_{2.17}Mn_{0.83}Ga$	0.13 %	20g
$Ni_{2.10}Mn_{0.90}Ga$	0.52 %	10g
$Ni_{2.05}Mn_{0.95}Ga$	1.10 %	10g

Table 3.1

Part of each ingot was powdered to a grain size of less than 250 μm. Both the powder and the remainder were annealed for 4 days at T = 800 °C under a reduced argon atmosphere and subsequently quenched into ice water.

After heat treatment a small piece in the form of a long thin bar was spark eroded from the solid part of the ingot of $Ni_{2.17}Mn_{0.83}Ga$ and polished. The sample dimensions were determined to $(24.27 \pm 0.01)mm$ for its length, $(0.97 \pm 0.01)mm$ for its height and $(2.20 \pm 0.01)mm$ for its width. The bar was used for resistivity measurements.

Specific heat measurements were carried out using differential scanning calorimetry both for powder samples and polished plates which had been spark eroded from the solid ingot. The details are given later in the appropriate chapter.

The annealed powder was used for structural investigations using X-ray diffraction experiments as well as for magnetisation measurements. In addition to the sample of $Ni_{2.17}Mn_{0.83}Ga$ listed in table (3.1) a second sample of $Ni_{2.17}Mn_{0.83}Ga$ prepared earlier has been used for magnetisation experiments. The conditions of the preparation of this sample were identical to the conditions described above in terms of weighing, melting and powdering. The weight loss for this sample was less than 1%. The heat treatment was different as it was heat treated for 5 days at T = 800 °C. After annealing it was quenched into ice water.

Neutron diffraction experiments were carried out on a sample of $Ni_{2.17}Mn_{0.83}Ga$ heat treated for 2 days at T = 800 °C and quenched into ice water. The weight loss of this sample was less than 1%.

3.2) Experimental Techniques

The experimental techniques used for the investigation of the SMAs $Ni_{2+x}Mn_{1-x}Ga$ have been electrical resistivity, specific heat using differential scanning calorimetry, magnetisation measurements as well as structural investigations using both X-ray diffraction and neutron scattering.

In the following section the physical background of the various techniques used for this thesis is presented. Particular emphasis is placed on the structural investigations and on magnetisation measurements.

3.2.1) Resistivity

Background

If a conductor is connected to leads with an electrical potential difference U (measured in Volt V) an electric current I (measured in Ampère A) will flow. The current is proportional to U. The factor of proportionality is the electric resistance R (measured in Ohm Ω). This quantity is a measure of the ability of a material to conduct an electrical current. The relationship is given by Ohm's law:

$$U = R \cdot I \,. \qquad (3.1)$$

The electrical resistance depends on the material properties and on geometric factors. For example for a uniform rectangular bar R depends on the length L and the cross section A.

$$R = \rho \frac{L}{A}. \qquad (3.2)$$

The value ρ is called the resistivity or specific resistance. The resistivity is a characteristic of the material. It is sensitive to atomic and magnetic disorder, strain and band structure effects [1]. Resistance can be thought of as arising due to friction of electrons as they flow to equalise the potential difference. Electrons scatter because of deviations of atoms (or magnetic moments) from a periodic structure. Deviations of the nuclear structure (phonons, atomic disorder, dislocations, strain) or the arrangement of magnetic moments (spin waves, magnetic defects) make a contribution to the electric resistance. With changes in the electric resistance as a function of temperature it is possible to identify structural or magnetic phase transitions. Therefore a change in slope of the resistivity may be connected to a change in the crystallographic or magnetic structure of the material being tested.

Experimental set-up

The resistivity of $Ni_{2.17}Mn_{0.83}Ga$ was measured using the conventional four-point method as shown in figure (3.1). The sample is situated on a non-conducting sapphire plate in an evacuated space. The set-up is located on the cold finger of a displex (a closed cycle He-gas cooling device). A heater and a temperature sensor are connected to the sapphire plate. External leads are connected to the wire of the sample: 2 leads for the electric current and 2 leads for measuring the voltage drop across a known length of the sample. The current, which is flowing through the sample, and the voltage across the sample were determined using an ammeter and a voltmeter. Power was provided by a dc power supply. In order to eliminate contact voltages and thermal emfs the current direction

was reversed. The voltage drop across the sample was obtained as the appropriately average voltage for both current directions.

Experimentally the electric resistivity was determined as a function of temperature. In general measurements were carried out while heating as well as cooling. This allows the investigation of hysteretic properties for phase transitions of 1st order.

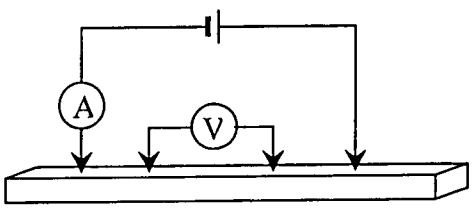

Figure 3.1

The schematic set-up of the four-point-resistivity measurement. The outer connections are the current leads and the inner connections are the voltage probes.

3.2.2) Specific Heat

The determination of the specific heat, or heat capacity, of a material enables phase transitions to be identified and to obtain information on the properties (e.g. lattice vibrations) of the material. Phase transitions manifest themselves as anomalies in the specific heat. At higher temperatures the "background" level of the specific heat, as provided by lattice vibration or magnetic contribution, will be a slowly varying function of temperature. Their contribution is described using some simple models such as the Einstein model or the Debye model for the lattice contribution to the specific heat. First the phenomenological description of the specific heat, and its connections to entropy S(T), is briefly described. Thereafter the Einstein and Debye models will be introduced, before the theory of differential scanning calorimetry measurements is presented.

Definition of heat capacity and specific heat

Adding an infinitesimal amount of heat dQ to a macroscopic system usually results in an infinitesimal change in temperature dT. This gives rise to a value called "heat capacity" c as the ratio of added heat to temperature rise.

$$c = \frac{dQ}{dT}. \qquad (3.3)$$

The specific heat $C = \frac{1}{N}\frac{dQ}{dT}$ is defined as the heat capacity per unit volume or per unit mass or per mole, where N is the appropriate number of units [2]. One has to distinguish between the heat capacity at constant volume and the heat capacity at constant pressure. This will be indicated in the formula using a subscript V (constant volume) or P (constant pressure).

Usually the heat capacity of a solid is measured at constant pressure. Thus the system is free to expand and thereby does mechanical work. This means that part of the heat input is used to do the mechanical work. Therefore more heat has to be added to achieve the same rise in temperature as compared to a specific heat measurement at constant volume:

$$C_P = \frac{dU + pdV}{dT}. \qquad (3.4)$$

Theoretically the more fundamental entity is the specific heat at constant volume since no work is done by the system and all added heat contributes fully to the rise in temperature. Therefore a heat input dQ is used entirely for increasing the internal energy dU:

$$C_V = \frac{dU}{dT}. \qquad (3.5)$$

The difference between these two quantities C_V and C_P is usually small for metals.

$$C_P = C_V + \frac{pdV}{dT}$$

$$= C_V + \frac{T \cdot V \cdot \alpha^2}{N \cdot \kappa_T}. \qquad (3.6)$$

Here $\kappa_T = -\frac{1}{V}\left(\frac{\partial V}{\partial p}\right)_T$ is the adiabatic compressibility and $\alpha = \frac{1}{V}\left(\frac{\partial V}{\partial T}\right)_p$ is the coefficient of thermal expansion. T is the temperature and V is the volume of the sample [3].

The second law of thermodynamics states that

$$dQ = T \cdot dS, \qquad (3.7)$$

where S is the entropy. Thus it follows that

$$C_V = \frac{dU}{dT} = T\frac{dS}{dT} \qquad (3.8)$$

which yields an expression for the entropy itself

$$S(T) = \int_0^T \frac{C(\tilde{T})}{\tilde{T}} d\tilde{T}. \qquad (3.9)$$

Contribution to the Heat Capacity

In general there are three contributions to the heat capacity of a solid, which arise from the lattice, the conduction electrons and from magnetic

moments ordering [5]. Here the contribution due to the lattice will be discussed first. Two approximate models, the Einstein and the Debye model, are useful for this purpose.

Einstein Model

Consider a crystal lattice. Atoms located at their respective equilibrium positions oscillate around the reference points. This motion contributes to the specific heat. If one assumes that all atoms vibrate independently of one another and with the same frequency then one arrives at the Einstein model. It has to be noted that with these assumptions no propagating modes exist. Despite this the Einstein model gives a fairly satisfactory description of the main features of the specific heat. In the Einstein model the thermal energy U of a sample containing N atoms is given by

$$U = 3N\left(\frac{\hbar\omega}{e^{\left(\frac{\hbar\omega}{k_B T}\right)}-1}+\frac{1}{2}\hbar\omega\right), \tag{3.10}$$

where $\hbar\omega$ is the energy of one oscillating atom and the factor $\frac{1}{e^{\left(\frac{\hbar\omega}{k_B T}\right)}-1}$ is the Bose factor. The Bose factor yields the average occupancy of a phonon mode in thermal equilibrium at temperature T. The second term proportional to $\frac{1}{2}\hbar\omega$ arises due to the zero point motion of atoms. This contribution is constant and independent of temperature. It vanishes when the internal energy is being differentiated with respect to temperature.

Since the heat capacity is defined as the derivative of internal energy with respect to temperature one arrives at

$$C_V = \left(\frac{dU}{dT}\right)_V = 3N \cdot k_B \left(\frac{\hbar\omega}{k_B T}\right)^2 \frac{e^{\frac{\hbar\omega}{k_B T}}}{\left(e^{\frac{\hbar\omega}{k_B T}} - 1\right)^2}. \qquad (3.11)$$

For low temperatures, i.e. $\frac{\hbar\omega}{k_B T} >> 1$, the specific heat predicted by the Einstein model tends to zero. This is in agreement with experimental observations. For high temperatures, i.e. $\frac{\hbar\omega}{k_B T} << 1$, the specific heat becomes temperature independent and constant. It then follows the Dulong and Petit value which is

$$C_V(T >> \frac{\hbar\omega}{k_B}) = 3N \cdot k_B. \qquad (3.12)$$

The Einstein temperature $\theta_{Einstein}$ is identified as $\theta_{Einstein} = \frac{\hbar\omega}{k_B}$. It indicates the point where the Einstein model "begins" to follow the law of Dulong and Petit. [2, 5].

Debye-Model

One shortcoming of the Einstein model is the absence of collective modes. This is rectified in the Debye model which takes into account that oscillators which contribute to the specific heat affect each other. This

gives rise to sound waves in a solid. To simplify the model the Brillouin zone is approximated by a sphere. Propagating modes are describes as

$$\omega = v \cdot k, \tag{3.13}$$

where $v = |\vec{v}|$ is the sound velocity and k a wave vector in the first Brillouin zone. The energy E of the modes is given by

$$E = v \cdot k \cdot \hbar. \tag{3.14}$$

If needed the model can be extended to include longitudinal and transverse oscillations. The dispersion of sound waves is linear up to a cut-off. Waves of frequencies greater than

$$\omega_D = v * \sqrt[3]{6\pi^2 \frac{N}{V}} \tag{3.15}$$

are not allowed [5]. This frequency ω_D is called the Debye frequency. Here N is the number of unit cells contained in the sample (equal to the number of acoustic phonon modes) and V is its volume. The number of modes per frequency range is given by the density of states for phonons. It is defined as

$$D(\omega) = \frac{V^2 \omega^2}{2\pi^2 v^3}. \tag{3.16}$$

ω and v are the frequency and the sound velocity as already defined in equation (3.13). The thermal energy due to 3 independent modes of vibration is given by

$$U = \frac{3V\hbar}{2\pi^2 v^3} \int_0^{\omega_D} d\omega \frac{\omega^3}{e^{\frac{\hbar\omega}{k_B T}} - 1} \tag{3.17}$$

and with the substitution $x \equiv \frac{\hbar\omega}{k_B T}$ it follows that

$$U = \frac{3Vk_B^4 T^4}{2\pi^2 v^3 \hbar^3} \int_0^{x_D} dx \frac{x^3}{e^x - 1}, \tag{3.18}$$

where $x_D \equiv \frac{\hbar\omega_D}{k_B T} \equiv \frac{\theta_D}{T}$. Hereby $\theta_D = \frac{\hbar v}{k_B} \cdot \left(\frac{6\pi^2 N}{V}\right)^{\frac{1}{3}}$ is called the Debye temperature. Therefore the internal energy can be written as

$$U = 9N_A k_B T \left(\frac{T}{\theta}\right)^3 \int_0^{x_D} dx \frac{x^3}{e^x - 1}. \tag{3.19}$$

Accordingly the heat capacity is given by

$$C_V = 9N_A k_B \left(\frac{T}{\theta}\right)^3 \int_0^{x_D} dx \frac{x^4 e^x}{\left(e^x - 1\right)^2}. \tag{3.20}$$

At high temperatures, i.e. $x << 1$, each mode contributes k_B to the heat capacity [3]. Therefore the high temperature limit of the heat capacity is $3N_A k_B$. At low temperatures, i.e. $x >> 1$, the upper limit in the integral

can be replaced by infinity. Since the integral $\int_0^{x_D} dx \frac{x^4 e^x}{(e^x - 1)^2}$ is a definite integral, it has a constant value. Therefore in the low temperature region the heat capacity behaves as T^3. In the following figure a superposition of the Einstein model and the Debye model is shown. The Einstein model agrees well with the experimental observation for higher temperatures, whereas for low temperatures the Debye model is more appropriate since the heat capacity approaches zero as T^3.

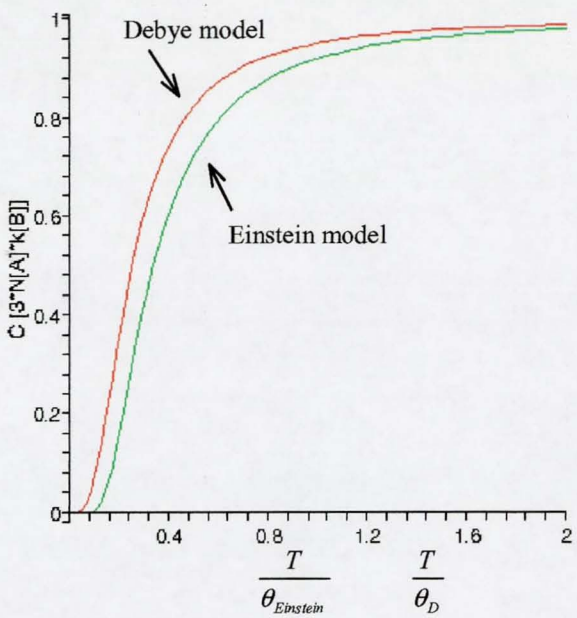

Figure 3.2

A comparison of the specific heat using the Einstein and the Debye models. At high temperatures the specific heat is normalized to 1. The temperature axis is in units of the Debye temperature θ_D or alternatively the Einstein temperature $\theta_{Einstein}$, respectively. For the calculation it has been assumed that $\theta_D = \theta_{Einstein}$.

3.2.2.1) Experimental Set-up and Background of the DSC Measurements

DSC is an abbreviation for Differential Scanning Calorimetry. The differential scanning calorimetry is a method that determines the heat flow to the specimen whilst being heated or cooled using a constant heating or cooling rate. The heat flow is determined by comparing the heat flow to or from the sample to that of a reference object (which exhibits a linear temperature rise and heat input relationship). The sample is situated in a standard aluminium pan. The reference object is an empty aluminium pan. This procedure ensures that the difference in heat flow is only due to the heat that goes into the sample. A sketch of the experimental set-up is shown in figure (3.3).

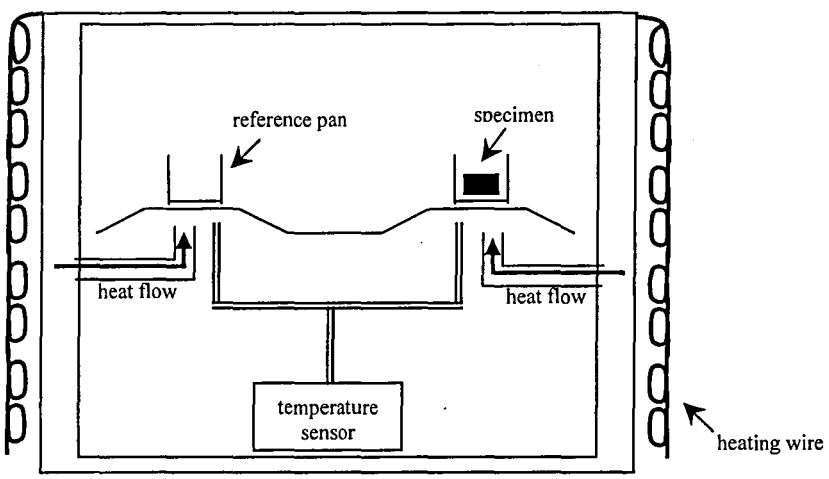

Figure 3.3

Experimental set-up of the DSC. The measurement takes place in an isolated environment (a cylinder surrounded by a heating wire). Both the reference pan (empty sample holder) and the sample holder including the specimen are supplied with an equal amount of heat. A temperature sensor measures the temperature difference of the reference and the sample holder including the specimen.

The heat flow to the sample is determined using the equivalent of Ohm's law for heat flow:

$$U = R \cdot I . \tag{3.21}$$

For electrical transport measurements U is the electric potential and $I = \dot{Q}$ is the electric current. For the case of an ohmic resistance, R is a constant. This principle can be translated to the case of heat transport [6]. Then the variables are interpreted as

$$\dot{Q} = \frac{T_1 - T_2}{R_{th}} . \tag{3.22}$$

Hereby $\dot{Q}$ is the heat transport, $T_1 - T_2$ is the temperature difference and R_{th} is the thermal resistance. The temperature difference $T_1 - T_2$ is the driving force behind every heat transport. The thermal resistance R_{th} can be determined in a calibration measurement using a substance with well known thermodynamic behaviour.

If T_F is the temperature of the furnace, T_S the temperature of the sample holder including the specimen and T_R the temperature of the reference object, the difference in heat flow to the sample and the reference object can be rewritten as

$$\dot{Q} = \frac{T_F - T_S}{R_{th}} - \frac{T_F - T_R}{R_{th}} . \tag{3.23}$$

Here it is assumed that the thermal resistances are equal for both the sample pan and the reference pan and that the temperature of the furnace is also the same for sample and reference. Simplifying equation (3.23) one arrives at

$$\dot{Q} = \frac{T_R - T_S}{R_{th}}. \qquad (3.24)$$

The physical quantity of interest for phase transitions is the specific heat. In the sample a phase transition gives rise to a change in heat flow. The heat flow $\dot{Q} = \frac{dQ}{dt}$ and the heating rate $\dot{T} = \frac{dT}{dt}$ are a direct measure for the specific heat C_p according to

$$C_P = \frac{dQ}{dT} = \frac{dQ}{dt} \cdot \frac{dt}{dT} = \frac{\dot{Q}}{\dot{T}}. \qquad (3.25)$$

Once $C_P(T)$ has been determined other quantities, such as the entropy as a function of T, can be obtained using equation (3.8).

3.2.3) Magnetism and Magnetic Moments

Introduction to Magnetism

Magnetism arises due to either the motion of an electron or due to the spin of the electron. These give rise to a magnetic moment $\vec{m}$ of a free atom. The macroscopic magnetisation $\vec{M}$ is defined as the magnetic moment per unit volume or per unit mass.

There are three possible contributions to the magnetic moment [5]:

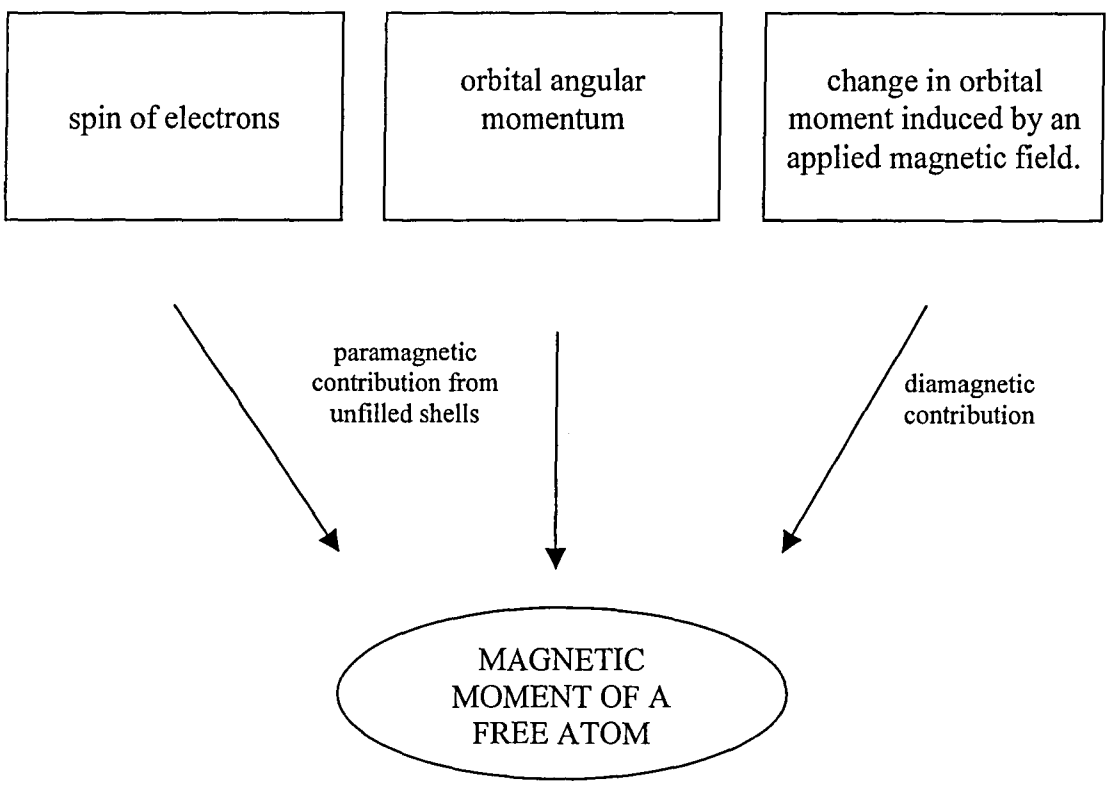

Figure 3.4

Before discussing the actual contributions to the magnetisation the various types of magnetic response will be briefly described. To

distinguish between these different contributions to the magnetic signal one can consider the magnetic susceptibility χ per unit volume or per unit weight (in short: susceptibility). It is defined as

$$\chi = \frac{1}{\mu_0} \cdot \frac{M}{H} \quad \text{(SI units)}, \tag{3.26}$$

$$\chi = \frac{M}{H} \quad \text{(cgs units)}, \tag{3.27}$$

where H is the macroscopic magnetic field (in the following SI units will be used). Often the susceptibility is referred to per unit mass or per mole (or formula unit) of the substance [5].

Diamagnetism

The susceptibility of a diamagnetic substance is negative and its magnitude is very small [4, 5]. Diamagnetism arises from complete electronic shells of atoms in response to the application of an external magnetic field. It is an induction phenomenon for which the induced magnetic moment is oriented antiparallel to the applied magnetic field direction. This applies to the orbital currents in complete shells of atoms as well as to conduction electrons in metals. For free atoms and insulators this is known as Langevin diamagnetism and for metals as Landau diamagnetism. The diamagnetic contribution is only detectable if other contributions, e.g. those arising due to local magnetic moments, are either zero or small (e.g. only arising from impurities).

Pauli Paramagnetism

The conduction electrons of metals give rise to Pauli paramagnetism. Here the spin is relevant [5]. If no magnetic field is applied there are as many electrons with spin up as there are with spin down in the conduction band. Thus there is no net magnetic moment. If a magnetic field is applied the electrons receive a small change in energy depending on whether their spin is oriented parallel or antiparallel to the applied magnetic field. The requirement of a common chemical potential (Fermi energy at T = 0) changes the numbers of electrons in the "up" band and "down" band. They adjust to equalize the chemical potential for both bands. Hence there are more electrons with a parallel than antiparallel spin orientation. Thus a net magnetisation results. The macroscopic magnetic moment can be described by

$$M = \chi_{pp} \cdot \mu_o H \,. \qquad (3.28)$$

The susceptibility χ_{pp} is known as the Pauli paramagnetic susceptibility. It is positive and essentially temperature independent. The contribution of conduction electrons is three times bigger than the contribution of the Landau diamagnetism.

Paramagnetism

The susceptibility of a paramagnet is positive. For many substances the paramagnetic signal arises due to localised magnetic moments [4]. Paramagnetism occurs in atoms when the outer shell is partially filled. It also arises in metals for which some ions carry a net magnetic moment.

If some inner shells of a metal ion are only partially filled (as for example for rare earth ions) there is a permanent magnetic moment. In a magnetic field and at finite temperatures these moments are partially aligned with respect to the applied field. But at elevated temperatures the thermal motion introduces disorder into the magnetic subsystem. Temperature randomises the orientation of magnetic moments and, without an external magnetic field, the macroscopic magnetisation vanishes:

$$\vec{M} = \chi_p \cdot \mu_0 \vec{H} . \qquad (3.29)$$

For small applied fields the magnetisation is a linear function of the applied magnetic field H. The susceptibility χ_p is strongly temperature dependent:

$$\chi_p = \chi_p(T). \qquad (3.30)$$

Ferromagnetism of localised moments

Ferromagnetism is an example of collective magnetism. The following discussion focuses on systems with a well defined local magnetic moment. For collective magnetism there exists a critical temperature below which the magnetic moments are ordered even without an applied magnetic field [4, 5, 7].

For ferromagnetic substances the critical temperature is called the Curie temperature T_C. For T = 0 K all magnetic moments are oriented

parallel. With increasing temperature disorder increases. The average angle between magnetic moments on neighbouring atoms increases until all moments are randomly oriented. The overall magnetisation vanishes at T_C. Above T_C the ferromagnet behaves like an ordinary paramagnet.

The Magnetic Moment and a Model of a Ferromagnetic Phase Transition

For this thesis the case of a ferromagnetic sample, namely Ni_2MnGa, will be of interest. Therefore it is appropriate to discuss in some detail a model for which all relevant entities can be calculated. The model considered here is one of magnetic moments of fixed magnitude created by one electron per atom. The moments interact with one another within a mean field model. Such a model system captures some essential features of the actual Ni_2MnGa system to be discussed later.

The magnetic energy E of an atom in an external field is given by

$$E = -\vec{M} \cdot \left(\mu_0 \vec{H}\right) = -\vec{M} \cdot \vec{B}, \qquad (3.31)$$

where $\vec{M}$ is the magnetic moment, $\vec{H}$ is the magnetic field and $\vec{B} = \mu_0 \vec{H}$ is the magnetic induction. μ_0 is the vacuum permeability and its value is

$$\mu_0 = 4\pi \cdot 10^{-7} \frac{T \cdot m}{A}. \qquad (3.32)$$

The magnetic moment is given by

$$\vec{M} = -\mu_B \cdot g \cdot \vec{S}, \tag{3.33}$$

where μ_B, the Bohr magneton, is the magnetic moment of a single electron. The value of μ_B is

$$\mu_B = \frac{e\hbar}{2m} = 9.2741 \cdot 10^{-24} \frac{J}{T} \tag{3.34}$$

(or in cgs units: $\mu_B = 9.2741 \cdot 10^{-21} \frac{erg}{G}$).

g is the Landé factor. For a free atom it is given by

$$g = 1 + \frac{J(J+1) + S(S+1) - L(L+1)}{2J(J+1)}. \tag{3.35}$$

Here $\hbar S$ is the spin, $\hbar L$ the angular momentum and the total angular momentum $\hbar J = \hbar L \pm \hbar S$. For a free electron $g = 2$ and $L = 0$ [4, 5, 7].

If S_z is the projection of the spin onto the axis of quantisation (which will be takes as the z-axis for all calculations carried out in this thesis), then one can express the magnetic moment with respect to the z-axis as

$$M_z = -\mu_B \cdot g \cdot S_z. \tag{3.36}$$

Energy levels

The energy levels of a system in a magnetic field B may be described by modifying equation (3.31):

$$E = g \cdot \mu_B \cdot m_j \cdot B, \qquad (3.37)$$

where m_j consists of all values $-J, -J+1, \ldots, J-1, J$

and $J = L \pm S$ according to Hund`s rules.

Example: Non-interacting electrons with spin $\frac{1}{2}$ in a magnetic field $\vec{B}$,

$\vec{B} = (0 \quad 0 \quad B_0)$. With L = 0

$J = L + S = S = \frac{1}{2} \quad \Rightarrow$ There exist two values of $m_{\uparrow,\downarrow}$: $+\frac{1}{2}, -\frac{1}{2}$.

Here "↑" indicates that the spin direction is parallel to the applied field.

$$E_{\uparrow} = g \cdot m_{\uparrow} \cdot \mu_B \cdot B = 2 \cdot \frac{1}{2} \cdot B \cdot \mu_B = B \cdot \mu_B ,$$

$$E_{\downarrow} = g \cdot m_{\downarrow} \cdot \mu_B \cdot B = 2 \cdot \left(-\frac{1}{2}\right) \cdot B \cdot \mu_B = -B \cdot \mu_B .$$

The effect of applying a magnetic field on the energy levels is shown in figures (3.5) and (3.6) [5].

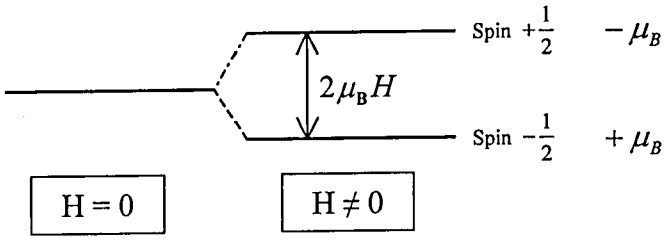

Figure 3.5

Splitting of energy levels for one electron due to the application of a magnetic field. The magnetic moment is opposite in sign to the spin direction.

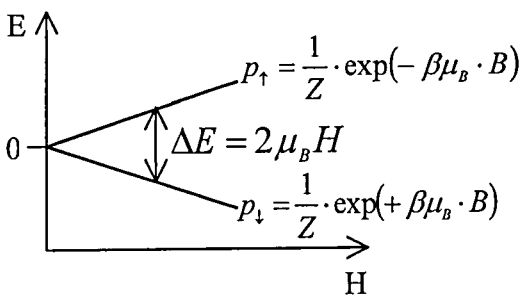

Figure 3.6

Splitting of energy levels as a function of applied field. The occupation probabilities $p_\uparrow$ and $p_\downarrow$ are also given.

The entity Z is the partition function and will be explained in the following part. $p_{\uparrow,\downarrow}$ are the occupation probabilities of the energy levels "up" and "down", respectively.

Thermodynamics

All equilibrium thermodynamic entities can be calculated once the partition function of the system is known. For a system of non-interacting magnetic moments the partition function is given by

$$Z = \sum_{\nu} e^{-\beta \cdot \varepsilon_\nu} , \qquad (3.38)$$

Here the sum runs over all energy states ν with energy ε_ν. $\beta = \frac{1}{k_B T}$, where $k_B = 1.381 \cdot 10^{-23} \frac{J}{K}$ is the Boltzmann constant [3]. For a spin $\frac{1}{2}$ system and an external applied field B equations (3.31), (3.36) and (3.38) yield an explicit expression for the partition function:

$$\begin{aligned} Z &= \sum_{S_z=-\frac{1}{2}}^{+\frac{1}{2}} e^{-\beta \cdot g \cdot \mu_B \cdot S_z \cdot B} = e^{-\beta \cdot \mu_B \cdot B} + e^{\beta \cdot \mu_B \cdot B} \\ &= 2\cosh(\beta \cdot \mu_B \cdot B) \ . \end{aligned} \qquad (3.39)$$

With the expression for the free energy F , which is given by

$$F = -k_B T \cdot \ln Z , \qquad (3.40)$$

the magnetic moment M in an applied field B can be obtained as

$$M_z = -\frac{\partial F}{\partial B}. \qquad (3.41)$$

An explicit calculation yields the following expression for the magnetic moment:

$$M_z = M_{0z} \tanh(\beta \cdot M_{0z} \cdot B), \qquad (3.42)$$

where $M_{0z} = \frac{g\mu_B}{2}$ is the saturation moment at T = 0 K. This expression determines the magnetisation as a function of temperature T and applied magnetic field B. For a small argument, that is $\beta M_{0z} B << 1$, an expansion of equation (3.42) yields the Curie susceptibility as

$$M = M_z = M_{0z} \frac{M_{0z} B}{k_B T} = \frac{M_{0z}^2}{k_B T} B = \chi \cdot B. \qquad (3.43)$$

With $M_{0z}^2 = \frac{1}{3} M_0^2$ one obtains for the susceptibility $\chi = \frac{M_0^2}{3k_B T}$.

This model is one of non-interacting magnetic moments. For such a model the thermodynamics of a system of magnetic moments in thermal equilibrium at temperature T can be analysed without problems. However, due to the absence of interactions, phase transitions cannot be explained within such a model. Next the model is extended to take into account interactions between magnetic moments. This is done within a mean field approximation. Such a model is able to explain some

important features of real systems. The mean field model for interacting magnetic moments of spin $\frac{1}{2}$ will be discussed next.

Interacting Magnetic Moments in Mean Field Approximation

Magnetic interactions between the microscopic magnetic moments in a solid are included in a model description using a mean field approximation. It is assumed that for a given magnetic moment an effective internal field exists [5]. This field is proportional to the polarisation of the magnetic moments in the immediate neighbourhood of the magnetic moment which is being considered:

$$\vec{B}_{\text{int}} = \lambda \cdot \vec{M}_z . \tag{3.44}$$

λ determines the strength of the interaction. It is also a function of the number of nearest neighbours. Taking into account the internal magnetic field as well as the external magnetic field, one arrives at

$$M_z = M_{0_z} \tanh\left(\beta \cdot M_{0_z}\left(B + \lambda \cdot M_z\right)\right). \tag{3.45}$$

This is a self-consistent equation for which a solution can be found either numerically or graphically. If there is more than one solution one has to take the one which minimises the free energy. Equation (3.45) can be rewritten as

$$\tanh^{-1}\left(\frac{M_z}{M_{0_z}}\right) = \beta \cdot M_{0_z}\left(B + \lambda \cdot M_z\right). \tag{3.46}$$

If no external field is applied equation (3.46) can be expressed as

$$\frac{M_z}{M_{0z}} = \tanh\left(\frac{m}{t}\right) = m . \qquad (3.47)$$

Here $m = \frac{M_z}{M_{0z}}$ is the magnetic moment measured in units of the saturation magnetisation at T = 0 K. It depends on the reduced temperature $t = \frac{T}{T_C}$. The identity $k_B T_C \equiv \lambda M_{0z}^2$ has been used for the calculation. Here T_C is the ferromagnetic transition temperature. The magnetisation as a function of reduced temperature is shown in figure (3.7). Details of the calculation will be discussed below.

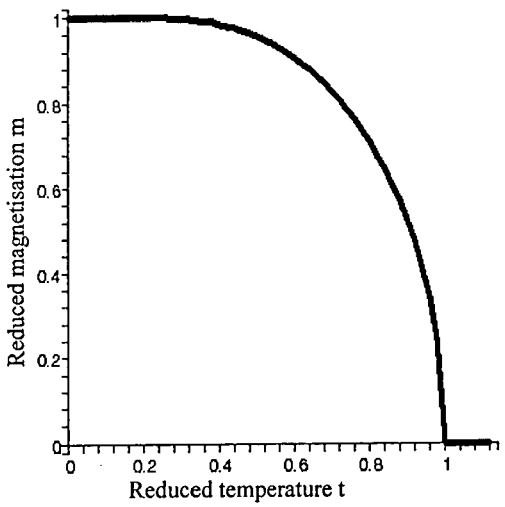

Figure 3.7
The magnetisation as a function of temperature. Interactions between magnetic moments are taken into account within a mean field approximation as given by equation (3.47). No external magnetic field is applied.

This shows that a ferromagnetic phase transition is possible if an interaction between magnetic moments is included. For a measurement using an external magnetic field equation (3.45) has to be used.

For $M << M_0$ the left-hand side of equation (3.46) can be expanded in a Taylor series, such that

$$\frac{M_z}{M_{0z}} + \frac{1}{3}\left(\frac{M_z}{M_{0z}}\right)^3 + \frac{1}{5}\left(\frac{M_z}{M_{0z}}\right)^5 + ... = \beta \cdot M_{0z}(B + \lambda \cdot M_z) \ . \quad (3.48)$$

Using $b = \frac{B}{\lambda M_{0z}}$ and the reduced variables already employed in equation (3.47) and equation (3.48) one obtains

$$m + \frac{m^3}{3} + \frac{m^5}{5} + ... = \frac{b+m}{t} . \quad (3.49)$$

Neglecting terms of higher order (beyond $\frac{m^5}{5}$) equation (3.49) can be rewritten as

$$m^2 = \frac{3}{t} \cdot \frac{b}{m} + 3(\frac{1}{t} - 1) \quad (3.50)$$

For small fields this is a linear equation in $\frac{b}{m}$ and m^2. Its slope is $\frac{3}{t}$ and its intersection with the m^2-axis is $3(\frac{1}{t} - 1)$. Since for paramagnetic phase the magnetisation is directly proportional to the applied magnetic field, the intersection with the $\frac{b}{m}$-axis yields the inverse susceptibility $\frac{1}{\chi}$.

$$m^2 = 0 \quad \Rightarrow \quad \frac{b}{m} = t - 1 = \frac{T - T_C}{T_C} \quad (3.51)$$

$$\Rightarrow \quad \frac{1}{\chi} = \frac{T - T_C}{T_C} \tag{3.52}$$

Without using the reduced parameters equation (3.48) can be expressed as

$$\frac{M_z^2}{M_{0z}^2} = 3\beta M_{0z}^2 \frac{B}{M_z} + 3\left(\beta\lambda M_{0z}^2 - 1\right). \tag{3.53}$$

The inverse susceptibility is then given by

$$\frac{1}{\chi} = \frac{B}{M_z} = \lambda k_B \frac{T - T_C}{T_C}. \tag{3.54}$$

Using the entity $M_{0z}^2 = g^2\mu_B^2 S_z^2 = \frac{1}{3} g^2 \mu_B^2 \hat{S}^2 = \frac{1}{3} g^2 \mu_B^2 S(S+1)$ the inverse susceptibility can be represented as

$$\frac{1}{\chi} = \frac{B}{M_z} = \frac{3k_B(T - T_C)}{g^2\mu_B^2 S(S+1)}. \tag{3.55}$$

Arrott plots

The graph of the linear part given by equation (3.53) is called Arrott plot. It is named after A. Arrott who developed this method in 1957 in order to identify the transition temperature T_C [8]. It is also a valid method to determine the magnetic moment $\vec{m}$ in zero-applied field at T = 0 K. If the magnetisation as a function of external applied magnetic field is

measured for fixed values of temperature (isotherms), one can plot the square of the magnetisation against the ratio of applied field B and magnetisation M for each isotherm. The intersection of the linear part of the isotherms with the positive $\frac{B}{M_z}$ – axis yields the inverse susceptibility for the appropriate isotherm. A plot of the inverse susceptibility against temperature enables the magnetic transition temperature T_C to be identified.

$$\frac{1}{\chi} = 0 = \frac{3k_B(T - T_C)}{N_A \mu_B \cdot g^2 S(S+1)}. \qquad (3.56)$$

Here the inverse susceptibility is expressed in terms of the number of atoms which are contained in one mole. N_A is the Avogadro constant. If the extrapolation of the Arrott plots intersects with the positive $\frac{B}{M_z}$-axis, the material is in the paramagnetic phase at that temperature. If it intersects with the positive M^2-axis, then it is in the ferromagnetic phase. For T_C the isotherm of the Arrott plot goes through the origin. Plotting the intersections of the linear part of the isotherms with the positive M_z^2-axis against temperature yields the spontaneous magnetic moment as well as the Curie temperature.

Model Solution for Spin $\frac{1}{2}$

A small C^{++} program was written in order to solve the self-consistent equation (3.53) giving the magnetisation M_z as a function of temperature T, applied magnetic field B and internal magnetic field λM_z. This program can be found in the appendix. The variables have been scaled as already introduced in equations (3.47) and (3.49):

$$m = \frac{M_z}{M_{0z}}, \quad b = \frac{B}{\lambda M_z|_{T=0}}, \quad t = \frac{T}{T_C}.$$

The magnetisation against applied magnetic field is plotted in figure (3.8). It can be seen that for temperatures significantly greater than T_c the magnetisation only saturates for very high fields. In fact, the external applied field B has to be more than 3 times greater than the internal field λM_{0z} for temperatures greater than 2.5 times the transition temperature T_c.

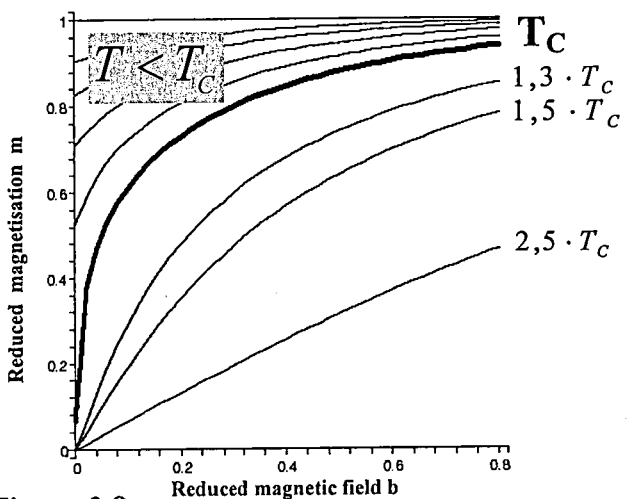

Figure 3.8

Magnetisation curves for isotherms in paramagnetic phase as well as in the ferromagnetic phase. They have been normalized to 1.

At T = 0 K the strength of the internal magnetic field is determined as

$$B_{\text{int}}\big|_{T=0K} = \frac{k_B T_C}{g\mu_B S}. \qquad (3.57)$$

For a sample with $T_C = 360K$ and spin $\frac{1}{2}$ the internal magnetic field is evaluated to $B_{\text{int}} = 536\ Tesla$. The figure below shows Arrott plots for the case of S = $\frac{1}{2}$ in mean field description as discussed above. The same model data points have been used as for figure (3.8).

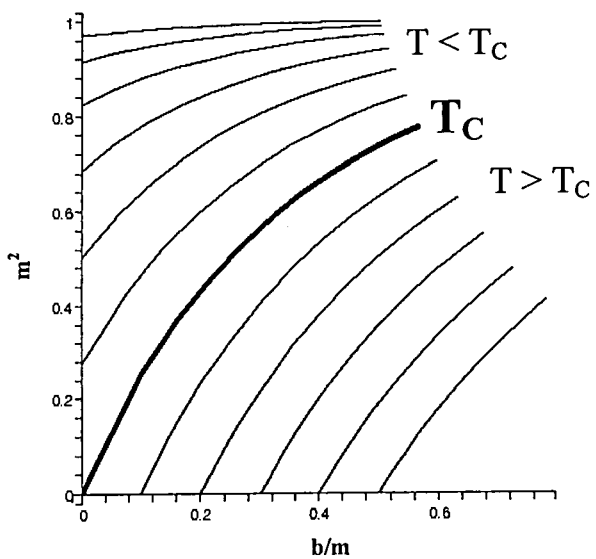

Figure 3.9

Arrott plots which belong to the magnetisation curves shown in figure (3.8). The magnetisation B is measured in units of the saturation magnetisation M_0. The magnetic field is measured in units of the internal magnetic field B_{int}.

3.2.4) Powder diffraction

Introduction

A crystal can be understood in terms of a three-dimensional lattice. Each lattice point is attached to a basis of atoms such that the basis is identical in composition, arrangement and orientation for every lattice point [5]. Every lattice point is taken to be the origin of a unit cell. A lattice point is not necessarily occupied by an atom. However atoms are distributed within the unit cell. The crystal is then build up by translations of unit cells. The translation vectors are determined by the lattice translations of the three dimensional lattice. A unit cell can be identified as the basic building block.

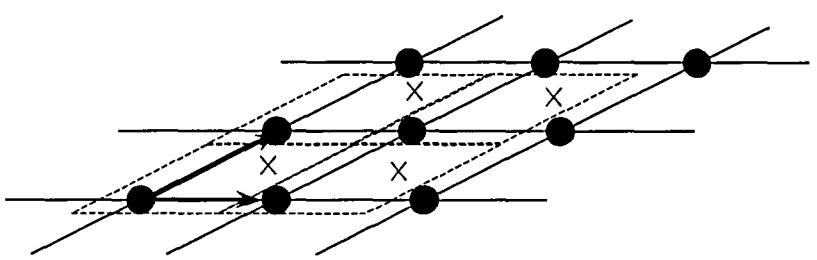

Figure 3.10

A two-dimensional array of atoms. The straight lines are the lattice. The dotted lines mark the unit cell which does not necessarily coincide with the lattice. The circles and crosses present atoms.

The choice of a unit cell is arbitrary. Usually there is more than one possibility to find a basis which describes the lattice. The only restriction for choosing the primitive unit cell is given by the requirement that the primitive unit cell contains the smallest possible number of atoms.

However, sometimes it is more convenient to choose a larger unit cell such that it reflects the full symmetry of the lattice. Independent of the choice of the unit cell the atomic arrangement looks the same from every lattice point $\vec{r}$ and $\vec{r}'$ which is related to one another by a lattice translation:

$$\vec{r}' = \vec{r} + u \cdot \vec{a} + v \cdot \vec{b} + w \cdot \vec{c} \,. \qquad (3.58)$$

Here $\vec{a}, \vec{b}, \vec{c}$ are the fundamental lattice translation vectors which belong to the chosen basis and u, v, w are integers. The position of the atoms inside the unit cell can be identified with respect to the translation vectors $\vec{a}, \vec{b}, \vec{c}$:

$$\vec{r}_j = x_j \vec{a} + y_j \vec{b} + z_j \vec{c} \,, \qquad (3.59)$$

Here $\vec{r}_j$ is the position of atom j in the unit cell. $0 \le x_j, y_j, z_j < 1$. The reference point is taken to be the origin of the unit cell which is being considered.

For a periodic crystal one can identify planes on which atoms are located. A plane is usually indexed using "Miller indices" (h k l). In order to obtain these values the intercepts of the plane with the $\vec{a}$, $\vec{b}$, $\vec{c}$ -axes of the coordinate system need to be determined. The Miller indices are the three smallest numbers which have the same ratio as the reciprocals of these intercepts. In figure (3.11) an example is shown of the identification of Miller indices.

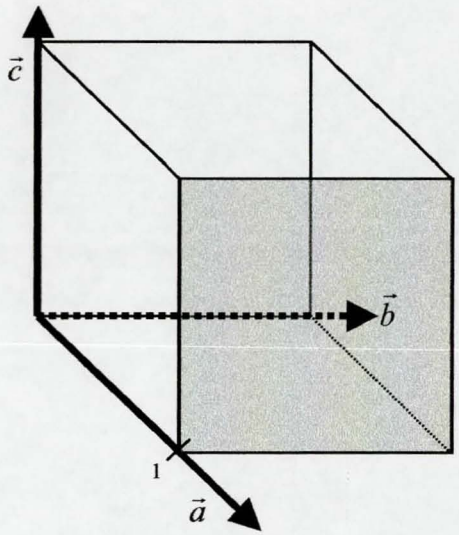

Figure 3.11

Identification of crystal planes with Miller indices. The shaded plane cuts the $\vec{a}$- axis at 1, but it does not cut the $\vec{b}$ - and $\vec{c}$ - axes. Hence the intercepts are 1, ∞, ∞ for the $\vec{a}, \vec{b}, \vec{c}$ - axes.

Evaluating the reciprocals of these numbers, one arrives at (1 0 0). These are the (h k l)-values for this particular plane.

Bragg's law

If a plane wave with wave vector $\vec{k}$ falls onto one of these crystal planes, it will be partly reflected. Part of it penetrates into the crystal and is then reflected by parallel planes below the surface.

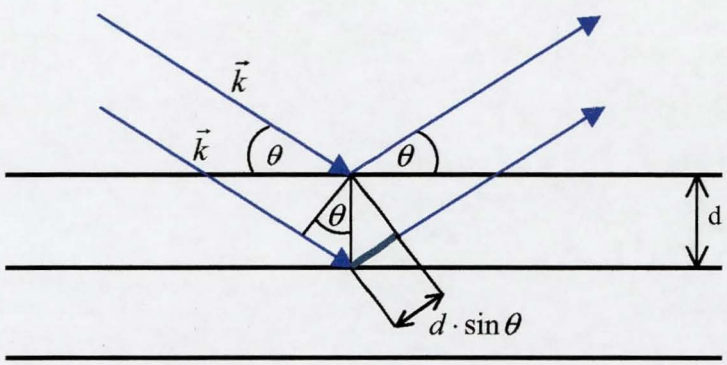

Figure 3.12

Coherent scattering of a wave on crystal planes. The distance between the scattering planes is d. The angle of the incoming and outgoing beam is θ.

Since for an ideal crystal the distances between the planes are constant and of atomic order, $\approx 10^{-8}$ m, the outgoing waves are coherent and have a fixed path difference. Hence interference occurs. For neutrons this can be used to determine the magnetic and nuclear structure of a crystal.

Suppose that a wave is incident onto a crystal such that the angle between the plane and the incident beam is θ with $0 < \theta < \frac{1}{2}\pi$. The angle between incident and outgoing beam is 2θ. The path difference δ between two waves reflected by two parallel planes is

$$\delta = 2 \cdot d \cdot \sin\theta . \qquad (3.60)$$

If the path difference between the interfering waves is an integer multiple of the wavelength λ, the outgoing waves are in phase and interfere constructively. This can be expressed using the formula

$$2 \cdot d \cdot \sin\theta = n \cdot \lambda . \qquad (3.61)$$

Here n is an integer. Destructive interference occurs if the path difference between the interacting waves equals $\frac{2n+1}{2}\lambda$. Equation (3.61) is called Bragg's law. The investigation of Bragg reflections enables the crystal structure to be determined. Bragg diffraction can be observed using powder samples as well as single crystals employing X-ray diffraction, neutron scattering or other particles (e.g. electrons). In the following, the experimental and theoretical background for the case of powder diffraction will be explained in more detail.

A powder contains grains with a random orientation. Thus if a beam (X-rays or neutrons) falls onto the powder there is no preferred direction in which the crystal is oriented with respect to the beam direction. Thus in a powder there will always be grains with the correct orientation for Bragg reflections to occur. Therefore a single wavelength can be used for powder diffraction. The intensity of the reflected beam is then measured as a function of scattering angle 2θ. The materials of interest for this thesis are Heusler alloys. At high temperatures, i.e. for $T > T_M$, they have the face centred cubic $L2_1$ Heusler structure. The Heusler structure is build up of four interpenetrating fcc sub-lattices. In the following the physics of a diffraction pattern of a cubic structure will be explored in more detail. This includes a discussion of how (h k l) values can be assigned to an observed Bragg peak. This indicates the crystallographic plane giving rise to constructive inference at a particular scattering angle in the diffraction pattern. The scattering angle 2θ is related to a scattering vector $\vec{k}$ as indicated in figure (3.14).

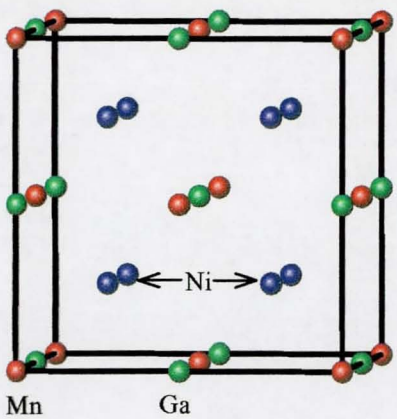

Figure 3.13
The Heusler structure.

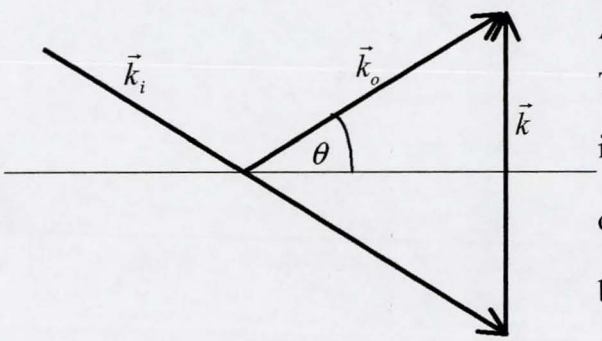

Figure 3.14
A wave hits a plane and is reflected. The wave vector of the incident beam is $\vec{k}_i$ and the wave vector of the outgoing beam is $\vec{k}_o$. The difference between $\vec{k}_i$ and $\vec{k}_o$ is the scattering vector $\vec{k}$.

The wave vector $\vec{k}$ is a reciprocal lattice vector with dimension $\frac{1}{length}$.

If $\vec{a}^*$, $\vec{b}^*$, $\vec{c}^*$ are unit vectors of reciprocal space and $\vec{a}$, $\vec{b}$, $\vec{c}$ are vectors of real space, then the following conditions are fulfilled:

$$\vec{a}^* \cdot \vec{b} = \vec{a}^* \cdot \vec{c} = \vec{b}^* \cdot c = 0 \ , \tag{3.62}$$

$$\vec{a}^* \cdot \vec{a} = \vec{b}^* \cdot \vec{b} = \vec{c}^* \cdot \vec{c} = 2\pi \ . \tag{3.63}$$

The wave vector $\vec{k}$ may be parameterised as

$$\vec{k} = h \cdot \vec{a}^* + k \cdot \vec{b}^* + l \cdot \vec{c}^* \ . \tag{3.64}$$

Here *h, k, l* are the same Miller indices as have been used for the indexation of lattice planes. Using equations (3.63) and (3.64) the magnitude of the wave vector $\vec{k}$ can be written as

$$\left|\vec{k}\right| = \sqrt{h^2\left|\vec{a}^*\right|^2 + k^2\left|\vec{b}^*\right|^2 + l^2\left|\vec{c}^*\right|^2}$$

$$= \sqrt{h^2 \cdot \frac{4\pi^2}{a^2} + k^2 \cdot \frac{4\pi^2}{b^2} + l^2 \cdot \frac{4\pi^2}{c^2}}$$

$$= 2\pi \cdot \sqrt{\frac{h^2}{a^2} + \frac{k^2}{b^2} + \frac{l^2}{c^2}} \ . \tag{3.65}$$

For the cubic lattice (a = b = c) this formula takes the form

$$\left|\vec{k}\right| = \frac{2\pi}{a} \cdot \sqrt{h^2 + k^2 + l^2} \ . \tag{3.66}$$

As may be seen from figure (3.14) there is the following relationship between the incident wave vector $\vec{k}_i$ and the scattering wave vector $\vec{k}$:

$$2 \cdot \sin\theta = \frac{|\vec{k}|}{|\vec{k}_o|}. \qquad (3.67)$$

The magnitude of the wave vector $\vec{k}_0$ of the outgoing wave is defined by the wavelength: $|\vec{k}_0| = \frac{2\pi}{\lambda}$. Therefore the wave vector $\vec{k}$ can be expressed in terms of the scattering angle:

$$2 \cdot \sin\theta = \frac{|\vec{k}|}{\frac{2\pi}{\lambda}} \quad \Rightarrow \quad |\vec{k}| = \frac{4\pi}{\lambda}\sin\theta. \qquad (3.68)$$

Equations (3.66) and (3.68) lead to a condition for the cubic unit cell which enables the lattice parameter and the scattering planes to be determined:

$$\sin\theta = \frac{\lambda}{2a}\sqrt{h^2 + k^2 + l^2}. \qquad (3.69)$$

Using equation (3.69) the high temperature phases of the Ni-rich compounds $Ni_{2.05}Mn_{0.95}Ga$, $Ni_{2.10}Mn_{0.90}Ga$ and $Ni_{2.17}Mn_{0.83}Ga$ have been investigated. Table (3.2) contains data of an X-ray diffraction pattern at room temperature of $Ni_{2.10}Mn_{0.90}Ga$. The wavelength used was λ = 1.54 Å. A picture of the X-ray diffraction pattern is shown in figure (3.15). Table (3.2) contains peak positions, their respective Miller

indices and the lattice constant obtained from a calculation employing equation (3.69).

One possible procedure for numerically identifying the peak indices is the following: For each peak position θ_i, which can be read of the diffraction pattern, the $\sin\theta_i$ - and $\sin^2\theta_i$ - values are calculated. According to equation (3.69) this corresponds to

$$\sin^2\theta_i = \left(\frac{\lambda}{2a}\right)^2 \left(h^2 + k^2 + l^2\right). \tag{3.70}$$

The ratios of the $\sin^2\theta_i$ - values can then be calculated. The constant factor $\left(\frac{\lambda}{2a}\right)^2$ drops out. This procedure yields the ratios of Miller indices:

$$\frac{(\sin\theta_i)^2}{(\sin\theta_j)^2} = \frac{h_i^2 + k_i^2 + l_i^2}{h_j^2 + k_j^2 + l_j^2}. \tag{3.71}$$

Bragg peaks can be indexed using equation (3.71). Each Bragg reflection is characterised by a single integer $(h^2 + k^2 + l^2)$. Equation (3.69) then enables the lattice constant to be determined.

i	Peak Position in $2\theta_i$ [deg]	$\sin^2\left(\frac{2\theta\cdot\pi}{360}\right)$	$\frac{\sin^2(2\theta_i)}{\sin^2(2\theta_1)}$	$\frac{\sin^2(2\theta_i)}{\sin^2(2\theta_2)}$	$\frac{\sin^2(2\theta_i)}{\sin^2(2\theta_3)}$	$\frac{\sin^2(2\theta_i)}{\sin^2(2\theta_4)}$	(h k l)	Lattice Constant [Å]
1	26.50	0.0525	1	0.37	0.19	0.12	(1 1 1)	5.82
2	44.01	0.1404	2.67	1	0.50	0.33	(2 2 0)	5.81
3	64.00	0.2808	5.34	2.00	1	0.67	(4 0 0)	5.81
4	80.89	0.4209	8.01	3.00	1.50	1	(4 2 2)	5.81

Table 3.2

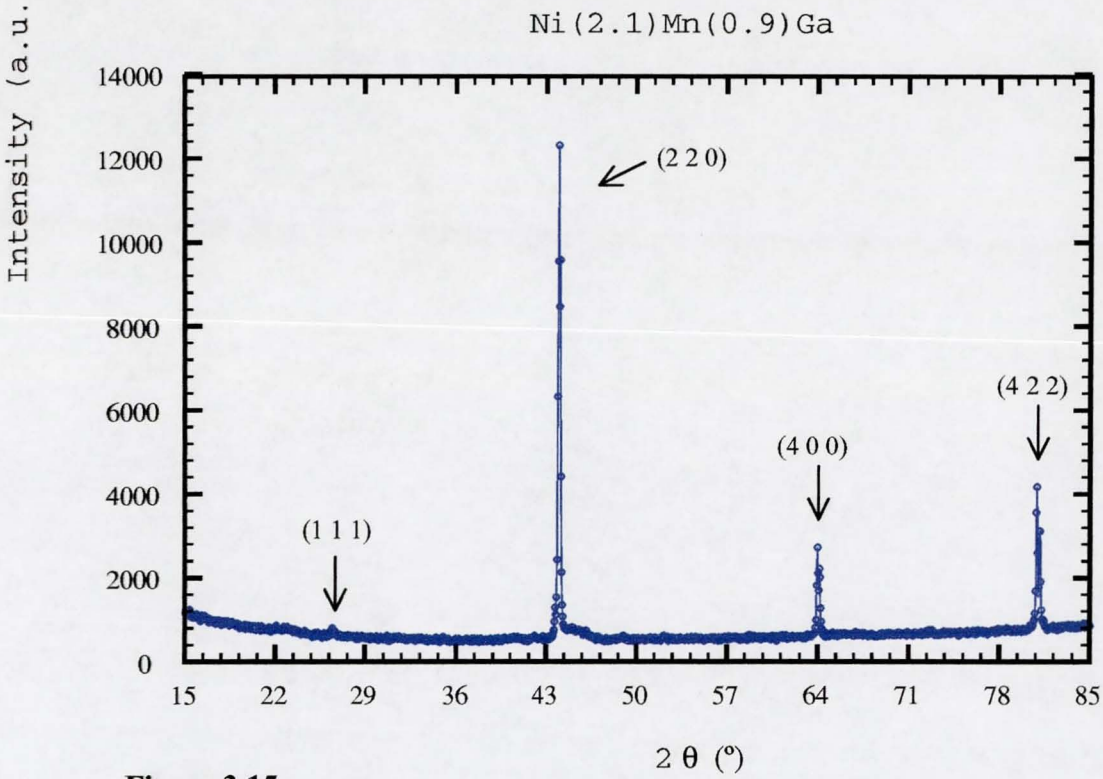

Figure 3.15

An X-ray diffraction pattern of $Ni_{2.10}Mn_{0.90}Ga$ at room temperature. The (h k l) values given by table (3.2) are also given.

Whereas the peak position is only a function of the lattice parameter and symmetry (the effect of symmetry will be discussed in the experimental section), the intensity of a Bragg reflection is a function of the atomic positions. These are taken into account in the structure factor F_{hkl}. The intensity is determined by the following relationship:

$$I \propto N \cdot \left|F_{hkl}\right|^2. \qquad (3.72)$$

Here N is the number of unit cells in the sample. In general the structure factor is a complex entity. It is given by

$$F_{hkl} = \sum_j b_j \cdot \exp\left(i \cdot \vec{k} \cdot \vec{r}_j\right). \qquad (3.73)$$

Here b_j is the scattering length of atom j. $\vec{k}$ is the wave vector as given by equation (3.64) and $\vec{r}_j$ is the position of atom j. The summation j is carried out over all atoms within the unit cell.

The structure factor takes into account the phase difference of waves scattered from the various atoms located within the unit cell. If a plane wave falls onto a crystalline sample a spherical wave develops at each atom position. As indicated in figure (3.16) for the whole crystal it is the superposition of the spherical waves which is registered in the detector (located far away from the sample) as a plane wave emerging from the crystal. The emerging wave front can be described as a plane wave using

$$\varphi = A \cdot \exp\left(i \cdot \vec{k} \cdot \vec{r}\right) \qquad (3.74)$$

where A is the complex amplitude and $\exp\left(i \cdot \vec{k} \cdot \vec{r}\right)$ represents the phase factor.

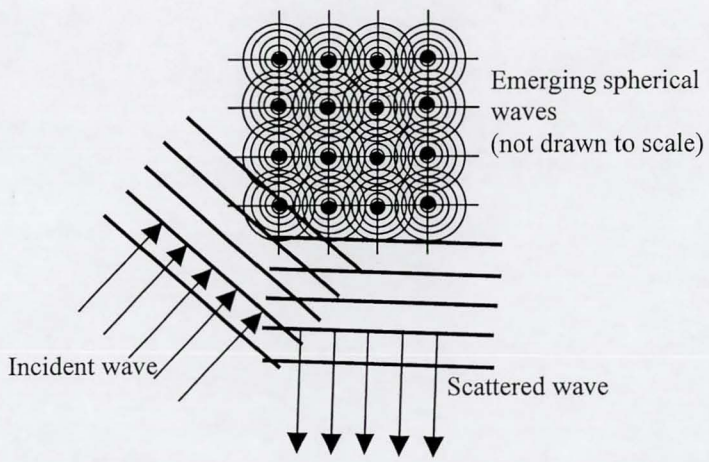

Figure 3.16
Schematic figure of a plane wave scattered by the atoms of a crystal.

As seen from the indexation of the Bragg reflections shown in figure (3.15) not all Bragg reflections are observed. In the pattern only those reflections have non-zero intensity for which (h k l) is either all odd or all even. This occurs due to centring translations within the unit cell. These symmetry operations are reflected in systematic absences (i.e. zero scattering intensities for some Bragg reflections).

The centring translations which are relevant for a cubic structure are the bcc and fcc centring translations. For a body centred lattice each atom at position (x, y, z) has a symmetry related atom sitting at ($x+\frac{1}{2}$, $y+\frac{1}{2}$, $z+\frac{1}{2}$). For a fcc lattice an atom at (x, y, z) has identical atoms sitting at ($x+\frac{1}{2}$, $y+\frac{1}{2}$, z), ($x+\frac{1}{2}$, y, $z+\frac{1}{2}$) and (x, $y+\frac{1}{2}$, $z+\frac{1}{2}$). The consequences for the structure factor will be analysed next.

For a bcc lattice one obtains

$$
\begin{aligned}
F_{hkl} &= \sum_j b_j \cdot \exp\left(i \cdot \vec{k} \cdot \vec{r}_j\right) \\
&= \sum_{j'} \left(b_{j'} e^{2\pi i (h\ k\ l) \cdot \begin{pmatrix} x_{j'} \\ y_{j'} \\ z_{j'} \end{pmatrix}} + b_{j'} e^{2\pi i (h\ k\ l) \cdot \begin{pmatrix} x_{j'}+\frac{1}{2} \\ y_{j'}+\frac{1}{2} \\ z_{j'}+\frac{1}{2} \end{pmatrix}} \right) = \sum_{j'} \left(b_{j'} e^{2\pi i (h\ k\ l) \cdot \begin{pmatrix} x_{j'} \\ y_{j'} \\ z_{j'} \end{pmatrix}} \left(1 + e^{\pi i (h+k+l)}\right) \right) \\
&= \sum_{j'} \left(b_{j'} e^{2\pi i \left(h \cdot x_{j'} + k \cdot y_{j'} + l \cdot z_{j'}\right)} \left(1 + e^{\pi i (h+k+l)}\right) \right)
\end{aligned}
\qquad (3.75)
$$

Here the sum over j' runs over a reduced set of atoms (reduced by a factor of 2 for a bcc lattice) within the unit cell. For (h + k + l) even $\exp(\pi \cdot i(h+k+l)) = +1$ while for (h + k + l) odd one obtains $\exp(\pi \cdot i(h+k+l)) = -1$. Thus the structure factor $F_{hkl} \equiv 0$ for (h + k + l) odd.

For a fcc lattice one obtains:

$$
\begin{aligned}
F_{hkl} &= \sum_j b_j \cdot \exp\left(i \cdot \vec{k} \cdot \vec{r}_j\right) \\
&= \sum_{j'} \left(b_{j'} e^{2\pi i (h\ k\ l) \cdot \begin{pmatrix} x_{j'} \\ y_{j'} \\ z_{j'} \end{pmatrix}} + b_{j'} e^{2\pi i (h\ k\ l) \cdot \begin{pmatrix} x_{j'}+\frac{1}{2} \\ y_{j'}+\frac{1}{2} \\ z_{j'}+0 \end{pmatrix}} + b_{j'} e^{2\pi i (h\ k\ l) \cdot \begin{pmatrix} x_{j'}+\frac{1}{2} \\ y_{j'}+0 \\ z_{j'}+\frac{1}{2} \end{pmatrix}} + b_{j'} e^{2\pi i (h\ k\ l) \cdot \begin{pmatrix} x_{j'}+0 \\ y_{j'}+\frac{1}{2} \\ z_{j'}+\frac{1}{2} \end{pmatrix}} \right) \\
&= \sum_{j'} \left(b_{j'} e^{2\pi i (h\ k\ l) \cdot \begin{pmatrix} x_{j'} \\ y_{j'} \\ z_{j'} \end{pmatrix}} \left(1 + e^{\pi i (h+k)} + e^{\pi i (h+l)} + e^{\pi i (k+l)}\right) \right) \\
&= \sum_{j'} \left(b_{j'} e^{2\pi i (h\ k\ l) \cdot \begin{pmatrix} x_{j'} \\ y_{j'} \\ z_{j'} \end{pmatrix}} \cdot \begin{cases} \cdot 4 & \text{if h, k, l are all even or all odd} \\ \cdot 0 & \text{all other cases} \end{cases} \right).
\end{aligned}
\qquad (3.76)
$$

Here j' runs over a reduced set of atoms of the unit cell. For a fcc structure the reduction factor is 4. For (h, k, l) all even the {} brackets yield a factor of 4, while for the case of 2 even and 1 odd or 1 even and 2 odd the summation in {} yields zero. Thus for a fcc structure only those Bragg reflections occur for which the (h k l)-values are all even or all odd.

Thus the diffraction pattern of $Ni_{2.10}Mn_{0.90}Ga$ as shown in figure (3.15) is expected to exhibit all reflections with the Miller indices either all even or all odd. However, as seen from table (3.2) and figure (3.15) the peaks indexed with values of the form (4*n-2 0 0), where n is an integer, do not occur in the pattern with an appreciable intensity. By contrast peaks such as the (4 0 0) reflection, are observed as intense peaks. In order to understand the reason for this relation one has to analyse the Heusler structure in more detail.

The Heusler lattice is build up of four interpenetrating ffc sublattices. The sublattices are shifted with respect to one another. This influences the intensity of Bragg reflections such that particular reflections are either week or strong. By denoting the structure factor of each sublattice X as F_X the combined structure factor $\widetilde{F}$ can be written in the following form:

$$\widetilde{F}=F_{Mn}+e^{2\pi i\left(\frac{h}{4}+\frac{k}{4}+\frac{l}{4}\right)}\cdot F_{Ni}+e^{2\pi i\left(\frac{h}{2}+\frac{k}{2}+\frac{l}{2}\right)}\cdot F_{Ga}+e^{2\pi i\left(\frac{3h}{4}+\frac{3k}{4}+\frac{3l}{4}\right)}\cdot F_{Ni}. \tag{3.77}$$

For the particular case of a (2 0 0) reflection, or more generally for a reflection of the form (4*n-2 0 0), it follows that

$$\widetilde{F} = F_{Mn} + F_{Ga} - 2F_{Ni}\,. \tag{3.78}$$

The structure factor is proportional to the scattering length, and $\widetilde{F} \propto b_{Mn} + b_{Ga} - 2 \cdot b_{Ni}$. Since for X-rays the scattering lengths are

fairly similar the difference is small. Thus in a diffraction experiment one can not easily distinguish between the scattering lengths of manganese, gallium and nickel. As a consequence the (2 0 0) reflection, and more generally the (4*n-2 0 0) reflections, are weak.

For a single cubic structure there are no centering translations. As a consequence all Bragg reflections are possible. A comparison with the indexation deduced in table (3.2) confirms that Ni_2MnGa compounds have a fcc structure.

References:

[1] The electrical resistivity of metals and alloys: P. L. Rossiter, Cambridge Solid State Science Series, 1991

[2] Fundamentals of Statistical and Thermal Physics: Frederick Reif, MaGraw-Hill Kogakusha, LTD, International Student Edition, 1965

[3] Thermodynamics and an Introduction to Thermostatistics: H.B. Callen, John Wiley and Sons, 2nd edition, 1985

[4] Solid State Magnetism: J. Crangle, Edward Arnold, 1991

[5] Introduction to Solid State Physics: C. Kittel, John Wiley and Sons, 5th edition, 1976

[6] DSC operating instructions, TA3000 System: Mettler Instrumente AG, 1984

[7] Quantentheorie des Magnetismus 1: W. Nolting, Teubner Studienbücher, 1986

[8] A. Arrott, Phys. Rev. **180**, 1394-1396, 1957

4) Experimental Results

4.1) Resistivity

Resistivity in the low temperature phase

The resistivity of $Ni_{2.17}Mn_{0.83}Ga$ was determined in the temperature range from T = 320 K to T = 50 K whilst cooling and heating. For a virgin sample measured for the first time with the temperature range from T = 320 K to T = 50 K the resistivity varies continuously with no discontinuity for either cooling or heating.

Contributions to the resistivity of a metal may arise from different sources. A temperature independent contribution arises due to disorder frozen into a lattice by quenching or equilibrium disorder. Thermal excitations of the lattice as well as magnetic excitations for a magnetically ordered sample contribute temperature dependent terms to the resistivity. All contributions to the resistivity add according to Matthiessen's rule [1]:

$$\rho_{tot}(T) = \rho_0 + \rho_p(T) + \rho_m(T). \qquad (4.1)$$

Here ρ_0 is the temperature independent term arising from atomic disorder. The temperature dependent contributions $\rho_p(T)$ and $\rho_m(T)$ originate from thermal excitations in the nuclear and magnetic subsystems, respectively.

The lattice contribution to the resistivity has a simple power law dependence expressed by the "Bloch T^5 law" [2]:

$$\rho_p(T) \propto T^5 . \qquad (4.2)$$

This expression is valid for low temperatures, i.e. $T << \theta_D$. It will be argued below that the lattice contribution is not the dominating influence on the resistivity for $Ni_{2.17}Mn_{0.83}Ga$.

The contribution to resistivity arising from magnetic disorder can be obtained using a simple model. A fixed magnetic moment system is considered with long-range magnetic interactions. For magnetic moments determined by a spin S and in the ferromagnetically ordered state the following expression for the resistivity has been derived [1, 3]:

$$\rho_m(T) = const.\left(1 - \frac{\langle S \rangle^2}{S(S+1)}\right). \qquad (4.3)$$

The resistivity was measured for $Ni_{2.17}Mn_{0.83}Ga$ below 300 K and within the ferromagnetically ordered state. Magnetisation measurements have been used to determine the spontaneous ferromagnetically ordered moment as a function of temperature using Arrott plots. This information can be used to model the magnetic contribution to the resistivity. This is done by replacing the square of the expectation value of the spin S, namely $\langle S \rangle^2$, by the experimentally determined square of the magnetic moment $M^2(T)$ and S(S+1) by an appropriate function of the moment at T = 0 K. Thus equation (4.3) becomes

$$\rho_m^{theory}(T) \cong const.\left(1-\frac{M^2}{M_0^2}\right), \qquad (4.4)$$

where $M_0^2 = M^2(T=0)$.

From equation (4.4) and using a power series expansion one can derive the following relationship:

$$\rho_m^{theory}(T) = const.\left(1-\frac{M^2(T)}{M_0^2}\right) = -aT^n, \qquad (4.5)$$

which is an approximate expression for modelling the magnetic contribution to the resistivity. a and n are the parameters which are determined by fitting the expression to an experimental observation. This has been done for a $Ni_{2.17}Mn_{0.83}Ga$ sample. Magnetisation data, obtained from Arrott plots, were taken and inserted into equation (4.4). In figure (4.1) a superposition is shown of the data obtained from the Arrott plots and a model calculation given by equation (4.5).

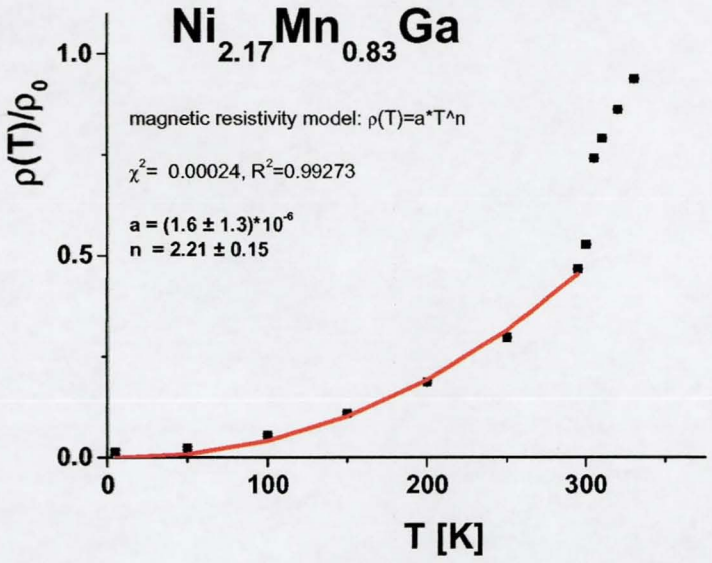

Figure 4.1

The magnetic contribution to the resistivity as obtained from Arrott plots (points) is fitted by the model given in equation (4.5). The fitted values for the parameters a and n are:

$a = (1.6 \pm 1.3) \cdot 10^{-6}$,

$n = 2.21 \pm 0.15$.

For the fit only the first 7 points have been taken into account because at higher temperatures the structural transition around T = 300 K changes the atomic configuration. Thus at temperatures above 300 K the resistivity is a more complicated function involving the various contributions with changed constants. The fit as presented in figure (4.1) yields a power of T with **n = (2.21 ± 0.15)**. This is the temperature dependence of the magnetic contribution to the resistivity expected for the temperature dependent static magnetic contribution.

Spin waves also contribute to the resistivity. This contribution involves inelastic scattering. It is expected to be proportional to T^2 [1]. In addition the magnetic moment correlations have contributions arising from pair correlations which are not taken into account properly by the simple model used here. Therefore slight deviations of the exponent are to be expected.

Both the power of T of the static contribution and the magnetic spin wave contribution are consistent with an expression for the resistivity which has the following power law:

$$\rho(T) = \rho_0 + a \cdot T^n \qquad n \approx 2. \qquad (4.6)$$

Within the magnetically ordered phase, and away from the temperature region where the structural phase transition takes place, one can attempt to fit the experimentally observed resistivity using a power law dependence. Such a fit is shown below:

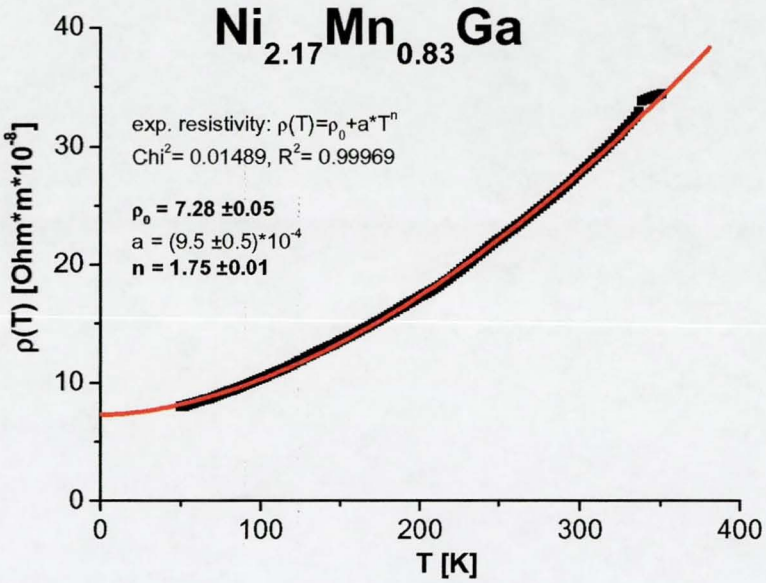

Figure 4.2

A fit of the experimental observation of the resistivity according to equation (4.6). The temperature independent term and the parameters a and n are also given.

The exponent obtained by fitting a power law to the temperature dependence of the resistivity at low temperatures is broadly consistent with the value obtained on the basis of spin waves and for a magnetic contribution. However, it is pointed out that the different estimates of the parameter n obtained using the different models do not coincide within the error bars.

In order to test the hypothesis that there may be other contributions to the resistivity (e.g. due to phonons) a different model has also been investigated. According to Matthiessen's rule [1] the resistivity has been taken to have the following contributions:

$$\rho(T) = \rho_0 + a \cdot T^{2.21} + b \cdot T^n . \qquad (4.7)$$

Here the additional term $b \cdot T^n$ takes into account other possible contributions to the resistivity. The magnetic contribution was included with an exponent of T as defined by the fit to the magnetisation model. The parameters ρ_0, a, b and n have been taken as adjustable parameters to be fitted to the temperature dependence of the observed resistivity. The resulting fit and the parameters are shown below:

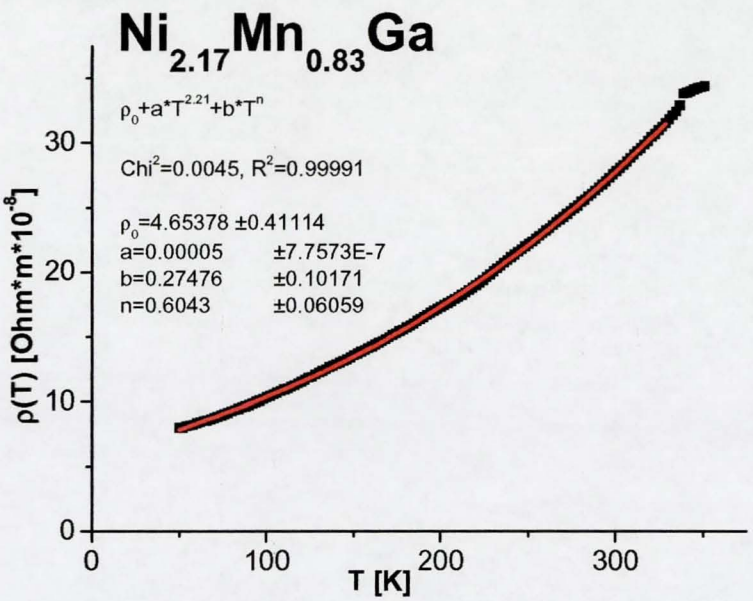

Figure 4.3

A fit of the resistivity fixing the parameter n to 2.21 and including an additional term $b*T^n$, where n is fitted to the experimental observation.

The fit indicates that a possible 2nd contribution might have a $T^{0.6}$ dependence. However, the amplitude of such a term is close to zero as measured in terms of its error value. Therefore such a contribution does not have an immediate physical significance. In particular, the data do not support a model with a T^5 contribution.

Rather it is argued here that the temperature dependence of the resistivity is close to the temperature dependence expected on the basis of the magnetisation model, as given by equation (4.5) with n = 1.75. This dependence minimises the change of the magnetic order using the experimentally observed magnetisation values as obtained using Arrott plots.

The Resistivity in the Transition Region

In the following section the experimental data will be discussed in the transition region at approximate T = 300 K. At these temperatures the resistivity for the $Ni_{2.17}Mn_{0.83}Ga$ sample is strongly influenced by structural changes. In figure (4.4) a comparison is shown between the resistivity for the virgin sample and the sample which has been heated through the transition for the first time. The data for the cooling and heating cycle at low temperatures is also included (hollow symbols) together with the measurement to higher temperatures above the structural phase transition (full symbols).

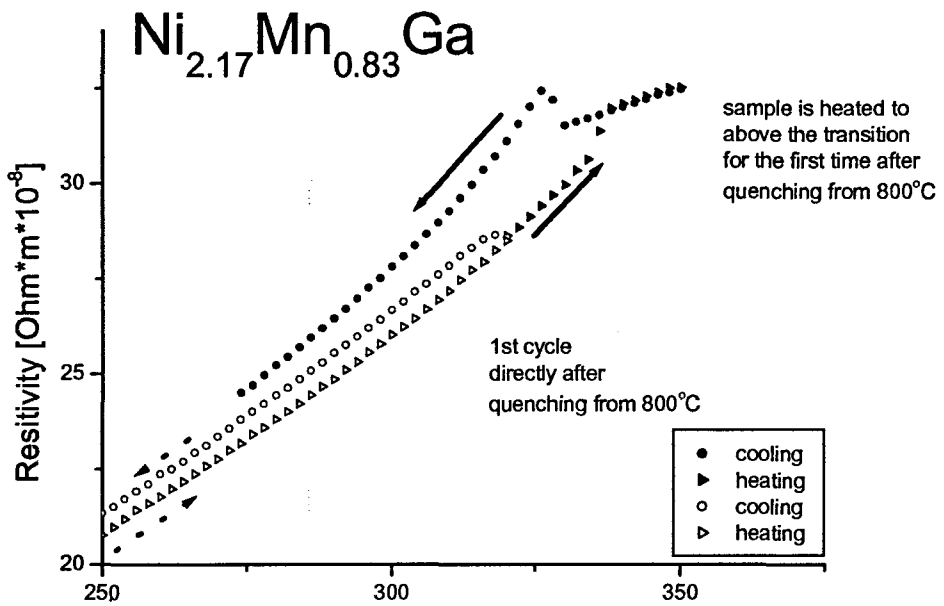

Figure 4.4

Resistivity of $Ni_{2.17}Mn_{0.83}Ga$ in the temperature range from T = 50 – 350 K.

For the investigation in the temperature range below room temperature the virgin sample shows the same behaviour for both heating and cooling. The experimentally observed data points are found to be essentially identical for the cooling and heating investigations. However, as the sample is heated to temperatures above room temperature and through the structural phase transition, anomalies occur. A distinct anomaly is observed which is identified as the structural phase transition. As the sample is cooled again the data taken during cooling show an anomaly at a different temperature indicating thermal hysteresis of the structural transition. Furthermore the anomaly is associated with a discontinuous increase of the resistivity at the transition, contrary to a distinct change of slope only on heating. After the transition has been traversed on cooling the resistivity is slightly higher than before.

On heating from room temperature at approx. T = 337 K a distinct change of slope of the resistivity is observed. This is the temperature where the sample is believed to undergo the structural phase transition on the heating part of the cycle. For temperatures larger than 337 K the slope is smaller than for lower temperatures. At higher temperatures the temperature variation of the resistivity is smooth and continuous up to 350 K the highest temperature employed for these measurements.

On cooling from T = 350 K to T = 338 K the resistivity retraces the same curve as was obtained for the heating cycle. It decreases further down to T = 330 K. At this temperature the resistivity begins to increase sharply and has a local maximum at 335 K. As the temperature is lowered further the resistivity decreases again. Both the peak on cooling and the change of slope on heating are interpreted as arising from the structural phase transition in the material. The transition is of first order with a temperature hysteresis of approximately $\Delta T = 10$ K.

In order to determine the behaviour of the sample and the characteristics of the phase transition the sample was repeatedly (3 times) cycled through the transition within the temperature interval of T = 250 K to T = 350 K. When the sample was cooled from T = 350 K down to T = 250 K the phase transition was observed at the same temperature as before. On further heating to T = 350 K the phase transition occurs at the same temperature as observed during the first heating cycling, albeit with slightly increased value of the resistivity. This confirms that on multiple cycling the temperature hysteresis of the phase transition is a reproducible feature.

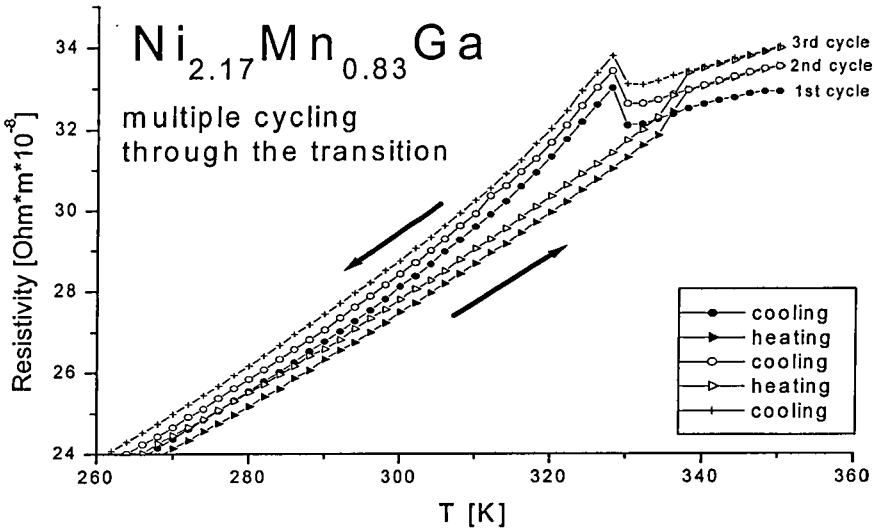

Figure 4.6

Resistivity of $Ni_{2.17}Mn_{0.83}Ga$ during multiple cycling through the transition temperature.

If the heating and cooling cycle is repeated the sample exhibits the same behaviour as it has shown before. With decreasing temperature, a peak occurs at T = 328 K indicating the onset of the phase transition. On the heating part of the cycle a change in the temperature slope of the resistivity occurs at T = 337 K. For each cycle the resistivity is observed to increase slightly. This is a known feature for shape memory alloys as the repeated cycling of samples through the phase transition while mechanically constraining the sample gives rise to forces which slightly change the experimental conditions for each cycle. Ideally a measurement of the resistivity of shape memory materials would require a method without the need to make electrical (and mechanical) contact to the sample. This, however, has not been part of this investigation. Therefore the unconstrained measurement of electrical resistivity will not be pursued further here.

4.2) Differential Scanning Calorimetry

DSC measurements have been carried out on samples of $Ni_{2.17}Mn_{0.83}Ga$, $Ni_{2.10}Mn_{0.90}Ga$ and $Ni_{2.05}Mn_{0.95}Ga$. In the following table the properties of the respective samples and the experimental details are given:

Sample $Ni_{2+x}Mn_{1-x}Ga$	Weight	Constitution	Annealing	Heating rate	Scanned temperature range
x = 0.05	56.16 mg	powder	4 d , 800 °C	10 K/min	heating: (-120) -> 300 °C cooling: 300 -> (-120) °C
x = 0.10	60.00 mg	powder	4 d , 800 °C	10 K/min	heating: (-120) -> 250 °C cooling: 250 -> (-120) °C
x = 0.17	15.90 mg	polished disk	4 d , 800 °C	10 K/min	heating: 0 -> 200 °C cooling: 120 -> 0 °C

Table 4.1

Sample characterisation

The sample with composition $Ni_{2.05}Mn_{0.95}Ga$ exhibits two distinct peaks in the DSC response. On cooling there is one peak at T = -58 °C and one smaller enhancement in the form of an asymmetric peak at T = 60 °C. The 2 peaks also occur during heating and with hysteresis.

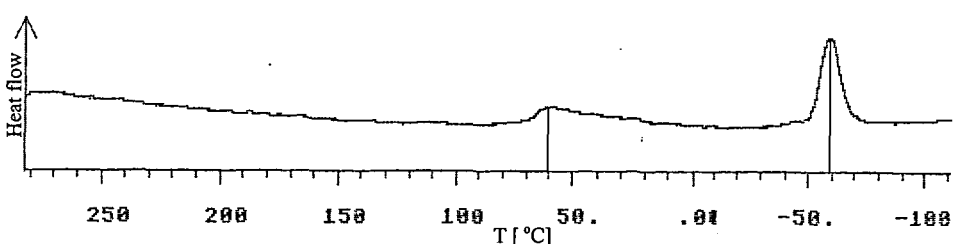

Figure 4.7

A temperature scan of $Ni_{2.05}Mn_{0.95}Ga$ during cooling. Two peaks appear at T = 60 °C and –58 °C which corresponds to T = 333 K and 215 K, respectively.

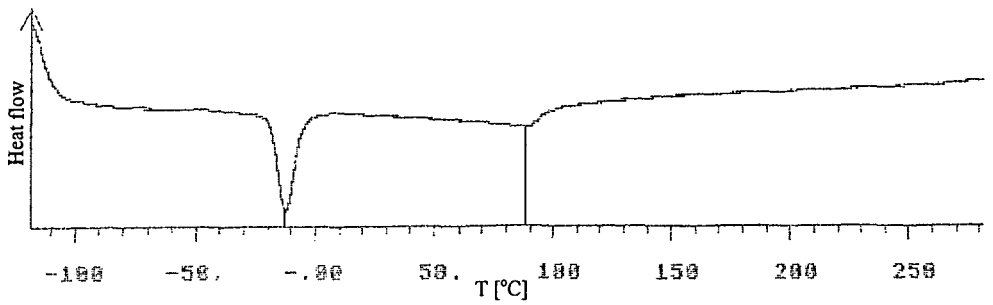

Figure 4.8

A temperature scan of $Ni_{2.05}Mn_{0.95}Ga$ during heating. Two peaks occur at T = 88 °C and –12 °C. This corresponds to 361 K and 261 K, respectively.

The heat flow to the sample is measured in terms of the heat flow to a reference object. If an endothermal phase transition occurs in the sample while heating the heat input to the sample is not used for an increase of its temperature. Thus the temperature of the sample lags behind and for some time it is lower than the temperature of the reference object. This is interpreted as a decrease in heat flow and the response given by the DSC is a dip in the heat flow curve. If a exothermal phase transition occurs during cooling the sample liberates heat and transfers it to the sample holder. Thus for the time of this phase transition the temperature of the sample is higher than the temperature of the reference object. Consequently the response given by the DSC is a positive peak.

Figures (4.9) and (4.10) show temperature scans for $Ni_{2.10}Mn_{0.90}Ga$ during cooling and heating. This sample shows two broad anomalies in the temperature scans. The response is only small.

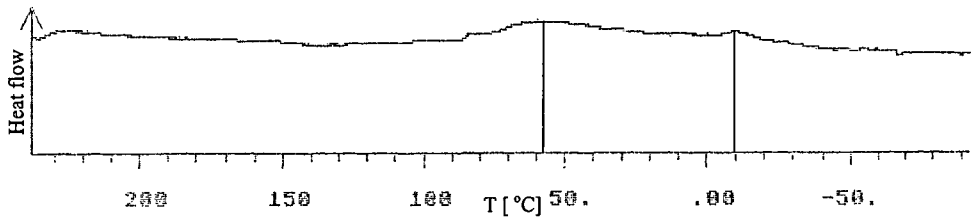

Figure 4.9

A temperature scan of $Ni_{2.10}Mn_{0.90}Ga$ during cooling. Two peaks occur at T = 58 °C and –10 °C. This corresponds to 331 K and 263 K, respectively.

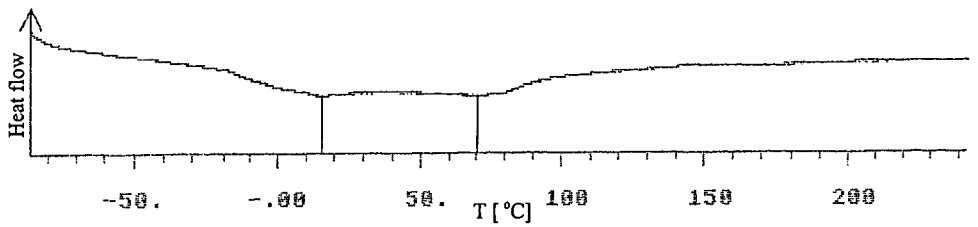

Figure 4.10

A temperature scan of $Ni_{2.10}Mn_{0.90}Ga$ during heating. Two peaks occur at T = 70 °C and 15 °C. This corresponds to 343 K and 288 K, respectively.

While $Ni_{2.17}Mn_{0.83}Ga$ exhibits two peaks on cooling, on heating only one single peak is observed. The peaks shown on cooling are small and broad, but in contrast to the response of $Ni_{2.10}Mn_{0.90}Ga$ these peaks show a clear maximum. The single peak exhibited on heating is more intense than the small peaks on cooling.

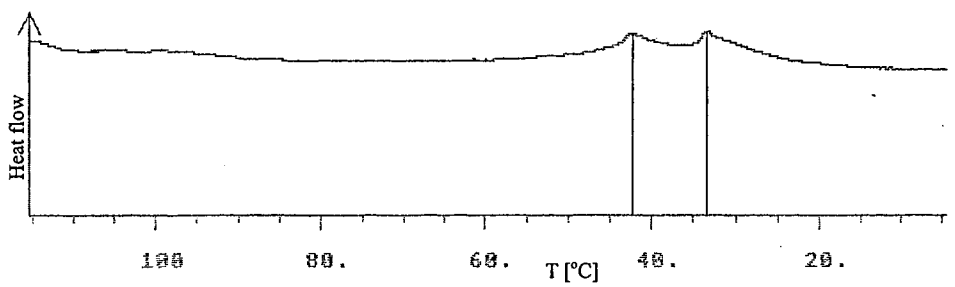

Figure 4.11

A temperature scan of $Ni_{2.17}Mn_{0.83}Ga$ during cooling. Two peaks occur at T = 42 °C and 33 °C. This corresponds to 315 K and 306 K, respectively.

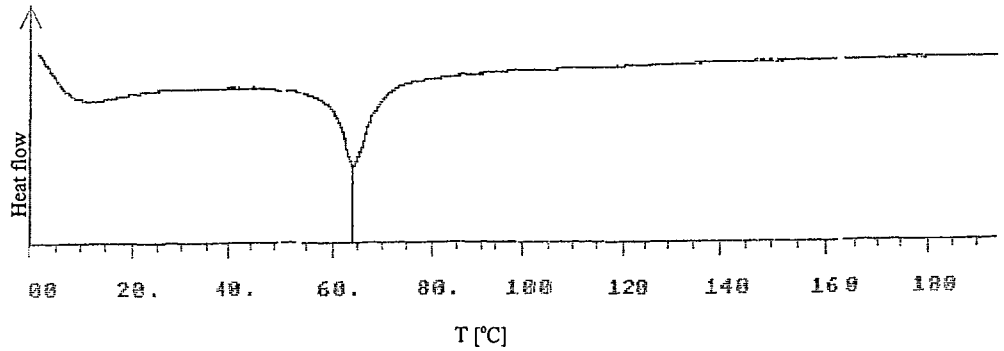

Figure 4.12

A temperature scan of $Ni_{2.17}Mn_{0.83}Ga$ during heating. One peak occurs at T = 64 °C . This corresponds to 337 K.

The peak positions are summarised in the table (4.2).

Composition		Peak Position	Peak Position
$Ni_{2.05}Mn_{0.95}Ga$	Heating	261 K	361 K
	Cooling	215 K	333 K
$Ni_{2.10}Mn_{0.90}Ga$	Heating	288 K	343 K
	Cooling	263 K	331 K
$Ni_{2.17}Mn_{0.83}Ga$	Heating	337 K	-
	Cooling	306 K	315 K

Table 4.2

Experimental results of the DSC measurements.

The compositional dependence of the phase transitions is shown in the figure (4.13). The high temperature anomalies, marked with ▲, ▼ in figure (4.13), are associated with the ferromagnetic transition temperature T_C. The ferromagnetic transition temperature is found to decrease with increasing Ni-content. This phase transition is expected to be of second order. However, experimentally hysteresis is found for this transition. The transition at lower temperatures, marked with △, ▽ in figure (4.13), is associated with the martensitic phase transition for which

thermal hysteresis is expected on the ground of this transition being of 1st order.

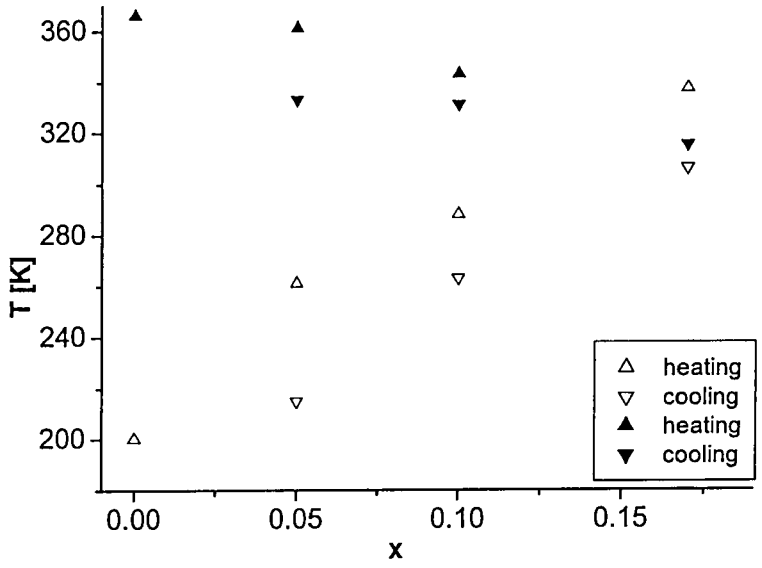

Figure 4.13

Phase transitions as a function of Ni-content. The open and filled triangles correspond to one transition, respectively. The data for the pure compound with x = 0 is taken from [4].

This phase diagram indicates the changes of transition temperatures as a function of increasing Ni content for $Ni_{2+x}Mn_{1-x}Ga$. The phase diagram obtained here is entirely consistent with the phase diagram given by Matsumoto et al. [5].

4.3) Magnetisation measurements using a SQUID magnetometer

Magnetisation measurements have been carried out on the following powdered samples using a SQUID magnetometer (Quantum Design):

Composition	Annealing [days, °C]	Mass [mg]	Molar weight [g/mol]
$Ni_{2.05}Mn_{0.95}Ga$	4, 800	3.80	242.2356
$Ni_{2.10}Mn_{0.90}Ga$	4, 800	1.49	242.4233
$Ni_{2.17}Mn_{0.83}Ga$ (A)	4, 800	4.10	242.6863

Table 4.3

Sample characteristics.

A second sample of composition $Ni_{2.17}Mn_{0.83}Ga$ was prepared at an earlier stage for a different set of measurements (for details see paragraph (3.1)). The characteristics of sample B are presented in table (4.4). The measuring conditions for the magnetic investigations were identical for all samples.

Composition	Annealing [days, °C]	Mass [mg]	Molar weight [g/mol]
$Ni_{2.17}Mn_{0.83}Ga$ (B)	5, 800	5.19	242.6862

Table 4.4

Sample characteristics of sample B.

Initially the magnetisation was measured as a function of temperature, for T = 5 – 360 K, in magnetic fields of B = 0.1 and 5.5 Tesla. The magnetisation data for $Ni_{2.17}Mn_{0.83}Ga$ was obtained in two subsequent sets of measurements. Magnetic isotherms were determined over the same temperature range in fields up to 5.5 Tesla.

Temperature scans of $Ni_{2.17}Mn_{0.83}Ga$

In figures (4.14) to (4.16) temperature scan are shown of the two different samples with the nominal composition of $Ni_{2.17}Mn_{0.83}Ga$.

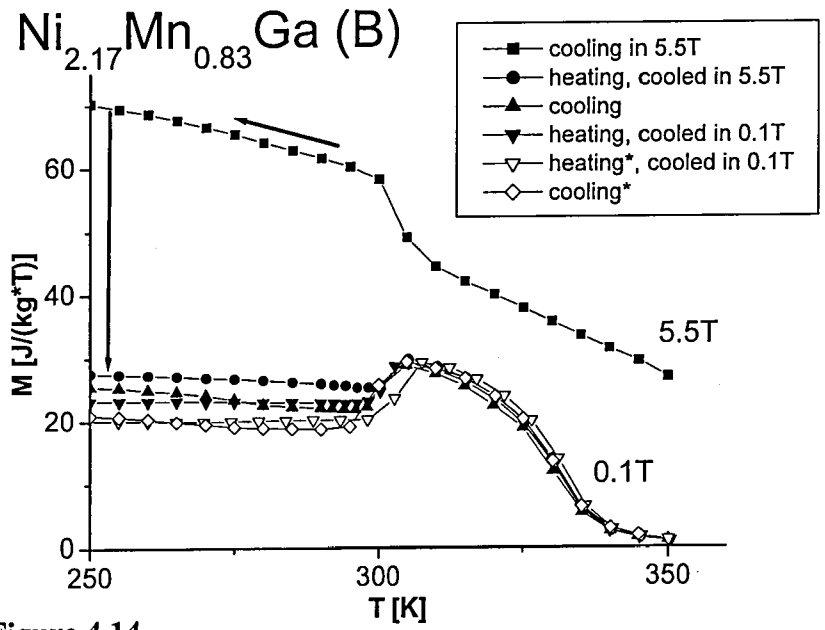

Figure 4.14

Temperature scans of $Ni_{2.17}Mn_{0.83}Ga$ (B) at different fields and whilst cooling and heating. Magnetisation data on heating was obtained from the sample when it was cooled down in high and low fields. Measurements indexed with * were taken earlier than measurements with no index.

Figure (4.14) shows temperature scans for sample B. The sample was heated to 350 K and a field of 5.5 Tesla was applied. Measurements were taken while cooling in a field to 250 K (■). At T = 250 K the field was changed to 0.1 Tesla (as indicated by an arrow in figure 4.3), and the magnetisation was determined while heating to 350 K (●). For comparison a measurement was also taken for the sample cooled from

350 K in a low field (0.1 T) to 250 K while heating in a field of 0.1 Tesla to 350K (▼). Subsequently field-cooled measurements in a field of 0.1 Tesla were obtained. These are displayed in figure (4.14) using ▲ symbols. The results of previous measurements are indicated by hollow symbols. The same sample was cooled in low field and measured while heating in a field of 0.1 Tesla (▽) and cooling (◊).

The magnetisation shows a discontinuity at approximately 310 K. With decreasing temperature an increase occurs for measurements in high magnetic fields, while for low fields the magnetisation decreases. Such behaviour is connected with the structural phase transition. The decrease of the magnetisation at higher temperatures arises due to the ferromagnetic phase transition at approximately 340 K.

There is a distinct difference of magnitude of the magnetisation at low temperatures between high field (5.5 Tesla) cooled and low field (0.1 Tesla) cooled measurements. For the measurements in fields of 0.1 Tesla the magnetisation is observed to be higher by $\approx$ 15 % for samples which were cooled in a high field than for the low field cooled cases.

For comparison measurements on sample A were also taken. These are shown in figure (4.15). The measurement cycle was identical for sample A as for sample B.

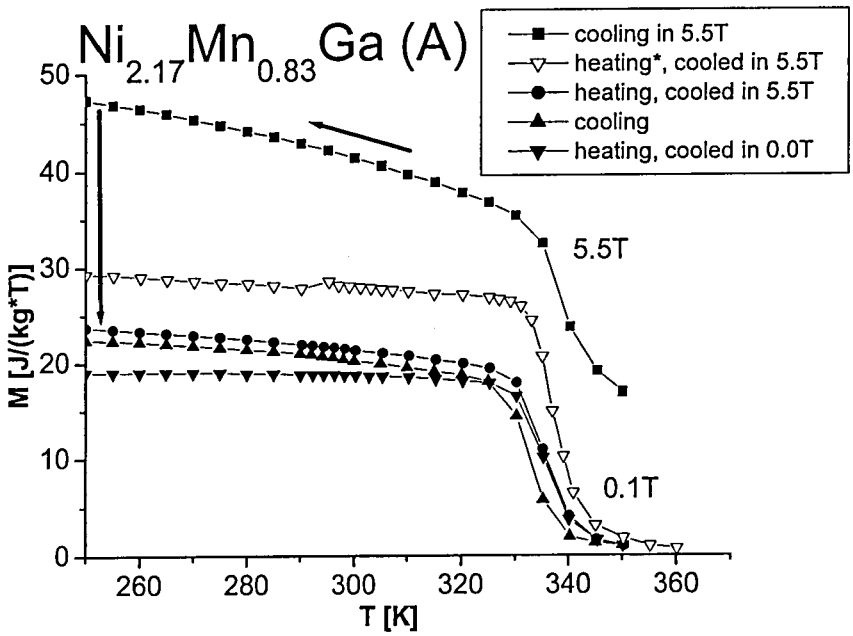

Figure 4.15

Temperature scans of $Ni_{2.17}Mn_{0.83}Ga$ at 5.5 Tesla and 0.1 Tesla applied magnetic for cooling and heating. The measurements on heating were taken when the sample was cooled down on high and low field previously. The measurement indexed with * was taken in advance to the other measurements.

Sample A shows the same gross features under high field and low field cooling as does sample B. However, the discontinuity as a function of temperature in the magnetisation data is not observed for sample A. The onset of the magnetically ordered phase is accompanied by a steeper increase of the magnetisation with reducing temperature for sample A compared to sample B.

The reason for the difference in the magnetisation is attributed to a shift in the martensitic phase transformation. For sample A the ferromagnetic and structural transitions coincide while for sample B the martensitic phase transformation takes place at a slightly reduced temperature of

310 K. It is argued that despite the nominally identical composition sample B has a slightly different Mn content. The weight loss for sample A was only 0.13% while for sample B it was higher, but still below 1%. The transformation temperatures observed in the magnetisation measurements are consistent with the phase diagram of Matsumoto et al. [5] for sample A. However, for sample B to agree with the phase diagram the composition has to be richer in Mn by approximately 0.02 compared to the nominal composition. According to Matsumoto et al. for a composition of approximately $Ni_{2.14}Mn_{0.86}Ga$ the structural transformation occurs at $\approx$ 310 K. Such a change in composition is entirely within the error and the weight loss of the sample preparation process for sample B. Therefore it is argued here that sample B has a true composition which is richer in Mn and poorer in Ni than is indicated by the nominal value. This interpretation is supported by the observation that the high field magnetisation is larger for sample B compared to sample A.

An interesting observation is made on these measurements with respect to the difference of results as a function of time. There is a distinct variation on the same sample for measurements taken at different points in time. For sample B the magnetisation for the low field cooled case in a field of 0.1 Tesla increases while for sample A a substantial reduction is observed. There seems to be an aging effect. This may arise either due to the presence of the martensitic phase or due to, for example, oxidation. This observation should form the basis for a future study.

In order to see the difference of the measurements more clearly the heating curves only are shown for both the A and the B samples in

figure (4.16). All measurements have been carried out in a field of 0.1 Tesla.

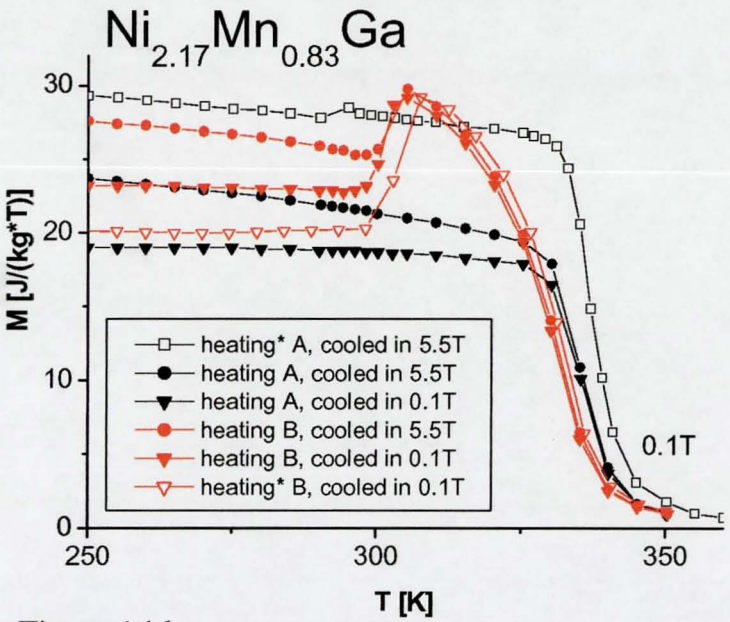

Figure 4.16

A comparison is shown of the magnetisation of the two samples of $Ni_{2.17}Mn_{0.83}Ga$ for heating in external applied field of B = 0.1 Tesla. The red data points belong to sample B. Measurements indexed with * were taken earlier than the other measurements.

For these measurements the magnitudes of magnetic moments are comparable. A variation of up to 15 % is observed in the size of the macroscopic magnetic moment depending on the conditions leading up to the measurement. This dependence reflects the hysteretic nature of the martensitic phase transformation.

The step like feature in the magnetisation data at the structural phase transition arises due to the formation of domains. The decrease in symmetry from the high temperature cubic phase to a phase of lower

symmetry is accompanied by a significant rearrangement of magnetic moments. This occurs due to the appearance of an easy axis of magnetisation for the phase of lower symmetry in the martensitic phase. For low fields the magnetic moments are not pulled into the external magnetic field direction, but are rather aligned along the easy axis of magnetisation. This results in a decrease of the magnetic moment projection onto the external magnetic field direction which is observed as a reduction of the macroscopic magnetic moment. By contrast if the phase transition occurs in the presence of a strong magnetic field the applied field is strong enough to select those crystallographic and magnetic domains which are aligned favourably to the external magnetic field direction. If the sample is cooled down in low fields the external applied magnetic field can only exert a limited influence on the orientation of the crystallographic domains in the low temperature phase. In this case in the high temperature phase the magnetic moments are partially aligned parallel to the external magnetic field direction. At the structural transition the structural domains pull the magnetic moments into the magnetically easy direction, thus reducing the effective number of magnetic moments which are aligned parallel to the external field direction. This increases the disorder of magnetic moments and reduces the macroscopic magnetisation. This situation is depicted in figure (4.17).

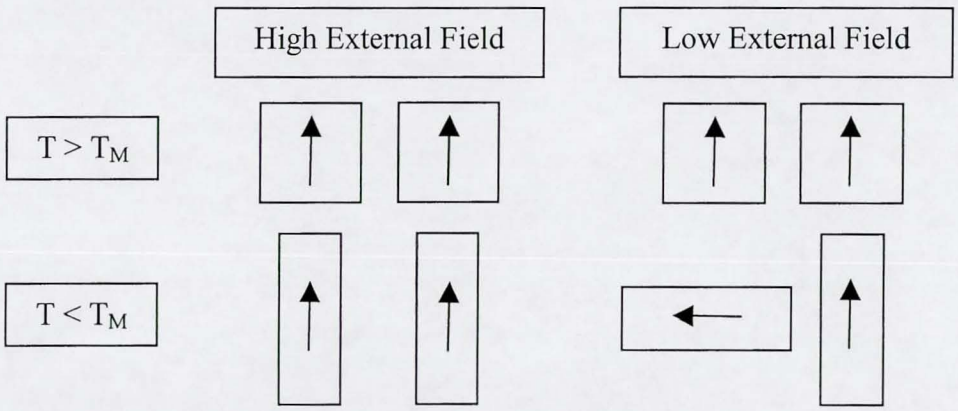

Figure 4.17

Domain distribution for external fields of different magnitude.

Temperature scans of $Ni_{2.05}Mn_{0.95}Ga$ and $Ni_{2.10}Mn_{0.90}Ga$

Figure (4.18) shows temperature scans of the magnetisation for the samples with composition $Ni_{2.05}Mn_{0.95}Ga$ and $Ni_{2.10}Mn_{0.90}Ga$. To ease the comparison for $Ni_{2+x}Mn_{1-x}Ga$ samples as a function of Ni-content x sample B of composition $Ni_{2.17}Mn_{0.83}Ga$ is also displayed. For these measurements the external magnetic field was fixed in magnitude to 0.1 Tesla.

Temperature scans have been measured while heating from low temperatures. At low temperatures the magnetisation is only weakly temperature dependent. At temperatures between 250 K and 300 K, and depending on composition, a sudden increase in the magnetisation is observed for all samples before the magnetisation starts to fall off more rapidly towards zero with a further increase of temperature.

Figure (4.18) shows that as a function of temperature the magnetisation decreases with increasing Ni-content. This is consistent with the notion that it is the Mn atoms which carry the main contribution to the macroscopic magnetic moment. Therefore a decrease of the Mn-content should be mirrored by a decrease of the macroscopic magnetic moment. At the same time, the peak, which occurs just below the magnetic phase transition, shifts to higher temperatures with increasing Ni-content. As argued more fully below this peak is related to the structural phase transition. With increasing Ni content the temperature for the structural transition increases, and the ferromagnetic transition temperature decreases.

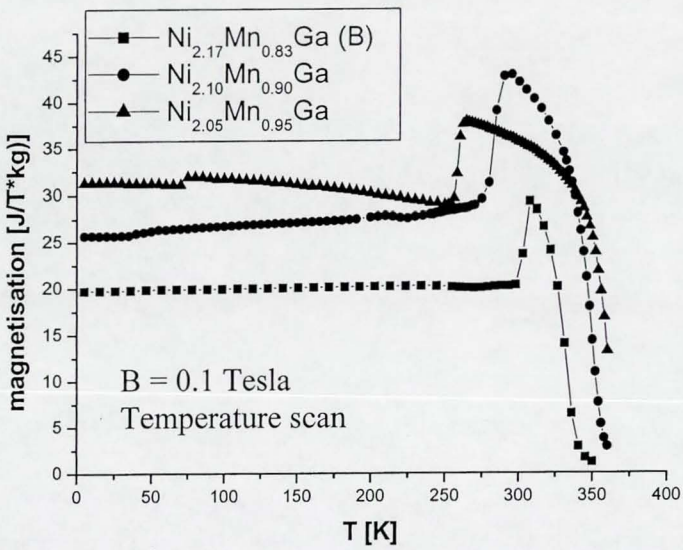

Figure 4.18

A superposition of the magnetisation is shown as a function of temperature in an applied field of B = 0.1 Tesla for $Ni_{2.05}Mn_{0.95}Ga$, $Ni_{2.10}Mn_{0.90}Ga$ and $Ni_{2.17}Mn_{0.83}Ga$ (B).

Next the magnetisation measurements are discussed which have been obtained as a function of applied magnetic field and at different temperatures. From these isotherms Arrott plots were constructed. With the help of Arrott plots the magnetisation was obtained at zero external field and as a function of temperature.

$Ni_{2.05}Mn_{0.95}Ga$ was measured as a function of applied field between 0.01 and 5.5 Tesla and within the temperature range from 5 K to T = 360 K. For a selection of the measured isotherms the magnetisation is shown in figure (4.19) and the Arrott plots are displayed in figure (4.20). The spontaneous magnetisation was obtained by fitting the high field part of the Arrott plot by a straight line and extrapolating it back to the M^2-axis. Figure (4.21) shows the spontaneous magnetisation obtained for $Ni_{2.05}Mn_{0.95}Ga$ as a function of temperature.

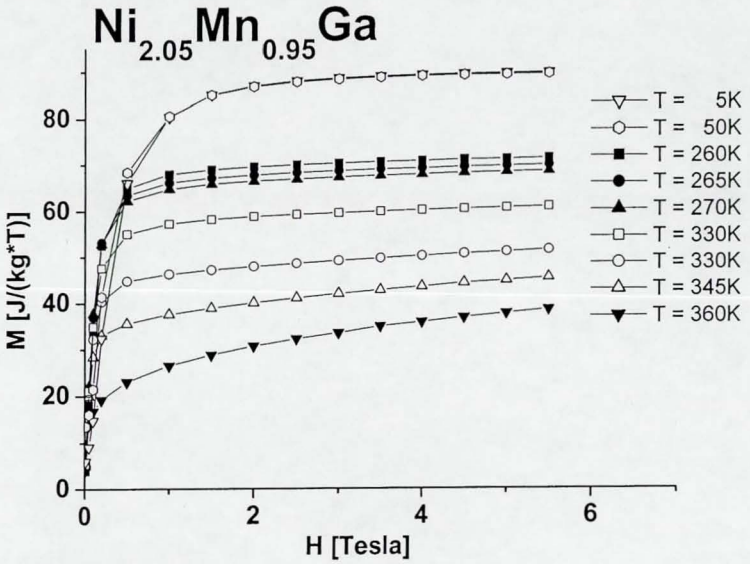

Figure 4.19

Magnetisation as a function of applied magnetic field for $Ni_{2.05}Mn_{0.95}Ga$.

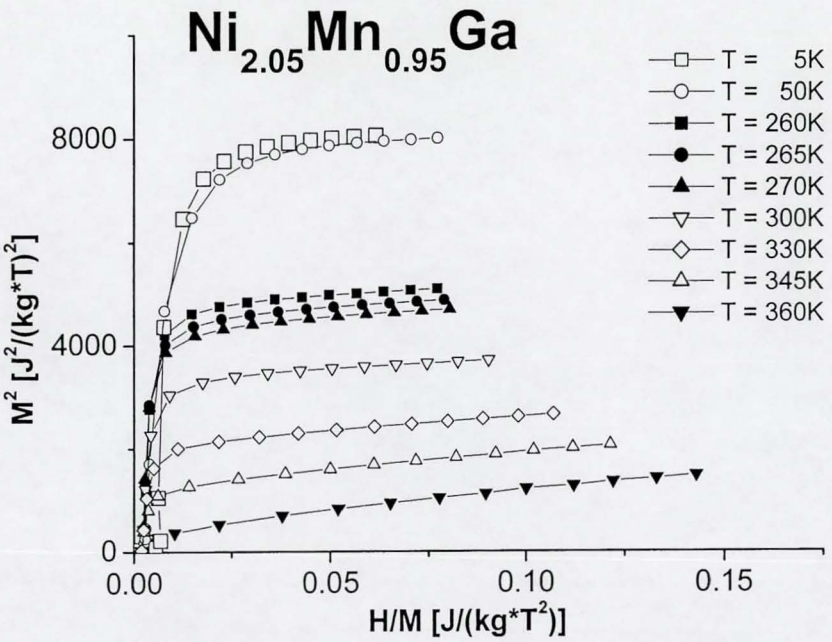

Figure 4.20

Arrott plots for $Ni_{2.05}Mn_{0.95}Ga$ using the magnetisation data of figure (4.19).

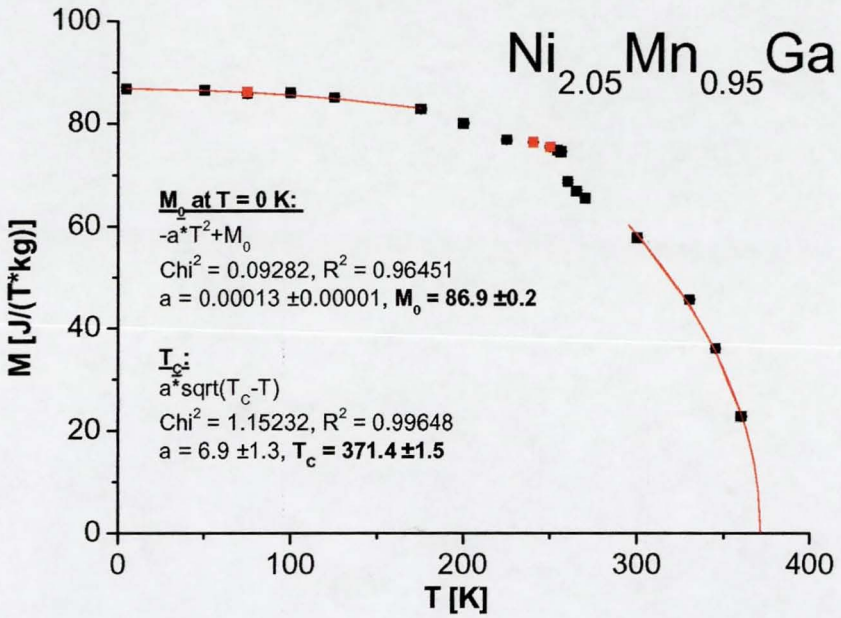

Figure 4.21

Magnetisation as a function of temperature as obtained from the Arrott plots. The saturation magnetic moment and the Curie temperature are fitted. The red data points belong to Arrott plots which were measured after cooling the sample.

A fit of the magnetisation at low and at high temperatures has been carried out and is also shown in figure (4.21). These fits yield the saturation magnetisation at T = 0 K and the Curie temperature T_C. For $Ni_{2.05}Mn_{0.95}Ga$ a transition temperature of T_C = (371.4 ± 1.5) K and a ground state magnetisation of $M_0 = (86.2 \pm 0.2)\ \frac{J}{T \cdot kg}$ is obtained. In the temperature region between approximately T = 200 K and 300 K an anomaly appears in the magnetisation. This anomaly is due to a structural phase transition which according to DSC measurements occurs at T = 260 K during heating. This corresponds well to the anomaly obtained from the Arrott plots.

Next the results of the measurements on the sample with composition $Ni_{2.10}Mn_{0.90}Ga$ are presented.

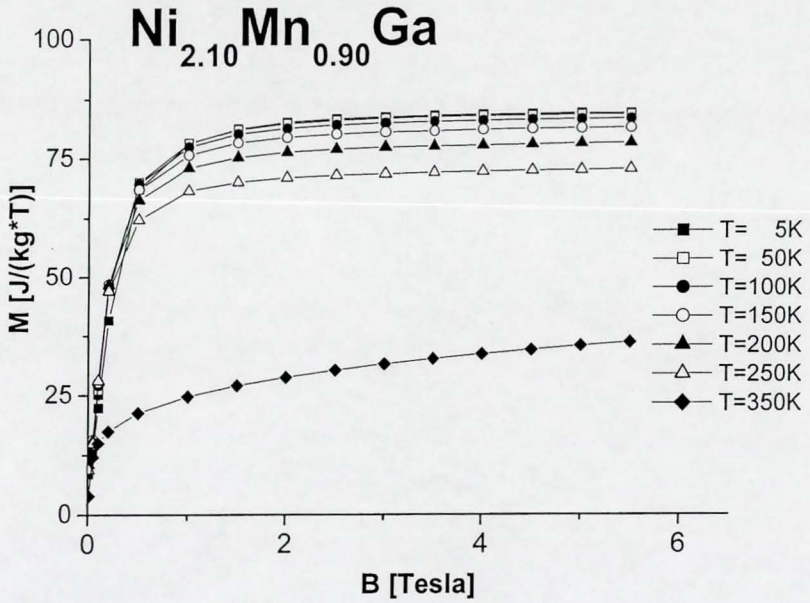

Figure 4.22

Magnetisation as a function of applied field of $Ni_{2.10}Mn_{0.90}Ga$. Isotherms were measured between T = 5 K and 350 K.

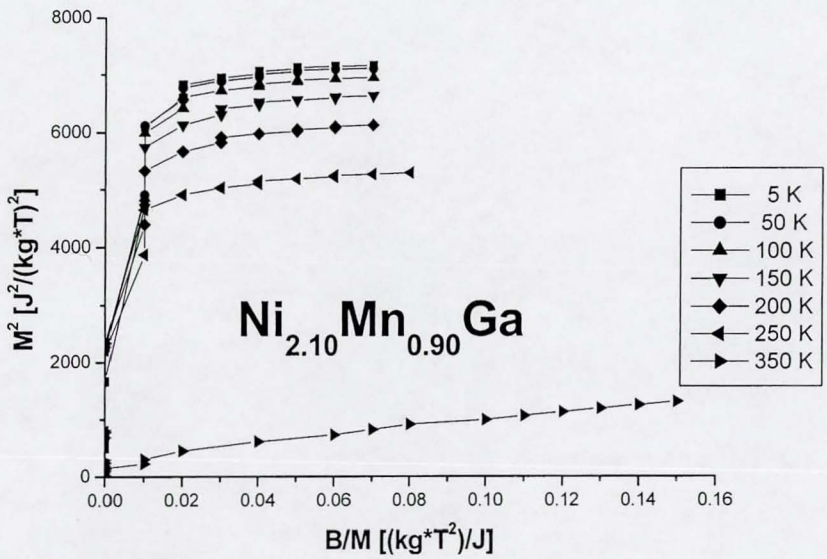

Figure 4.23

Arrott plots of $Ni_{2.10}Mn_{0.90}Ga$.

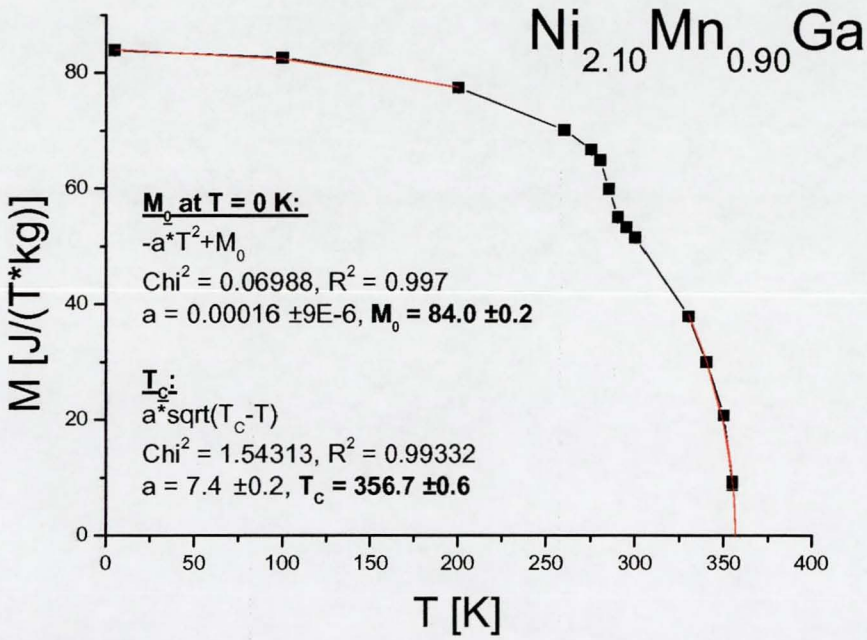

Figure 4.24

Magnetisation of $Ni_{2.10}Mn_{0.90}Ga$ as a function of temperature as obtained from the Arrott plots. Fits of the saturation magnetisation M_0 and T_C are also included.

For $Ni_{2.10}Mn_{0.90}Ga$ the temperature dependent spontaneous magnetic moment at zero applied field as obtained from the Arrott plots is shown in figure (4.12). A fit to the low temperature data yields a ground state moment of $M_0 = (84.0 \pm 0.2)\ \frac{J}{T \cdot kg}$. The ferromagnetic transition occurs at $T_C = (356.7 \pm 0.6)$ K. The isotherms were measured with increasing temperature. Thus the anomaly which occurs at T = 284 K corresponds to the structural phase transition during heating. The transition temperature obtained from magnetisation measurements is in agreement with DSC results which yield a martensitic transition temperature of 288 K.

Next measurements are presented on the Ni-rich sample with composition $Ni_{2.17}Mn_{0.83}Ga$ (sample B).

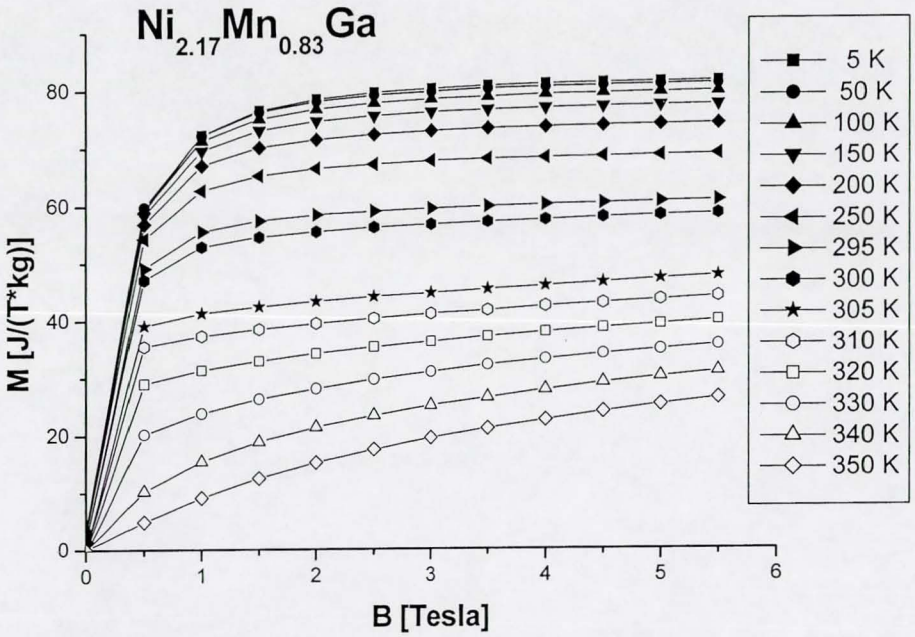

Figure 4.25

Magnetisation as a function of applied magnetic field. Isotherms were measured between T = 5 K and 350 K.

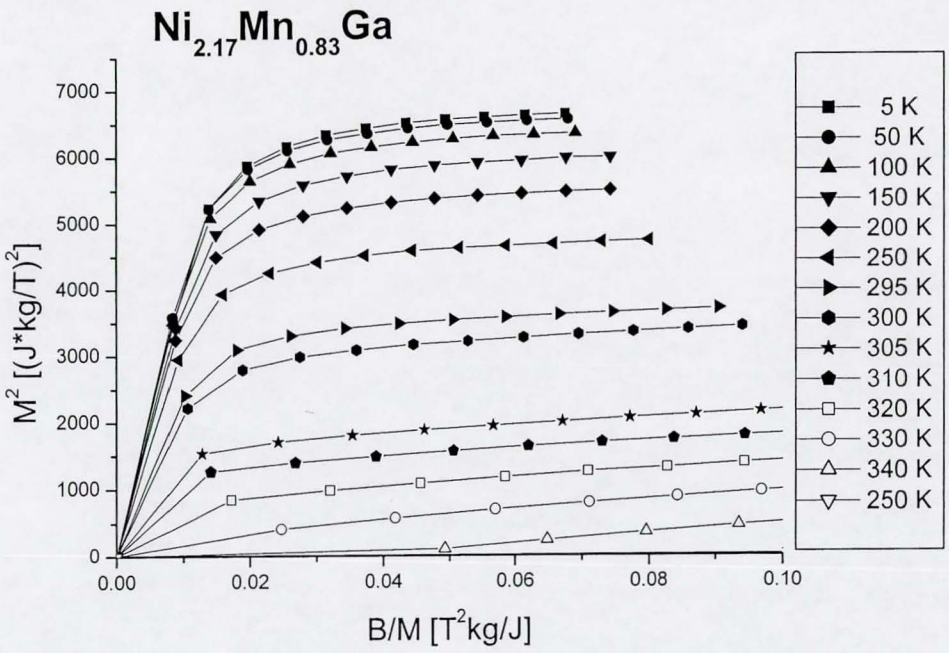

Figure 4.26

Arrott plots of $Ni_{2.17}Mn_{0.83}Ga$.

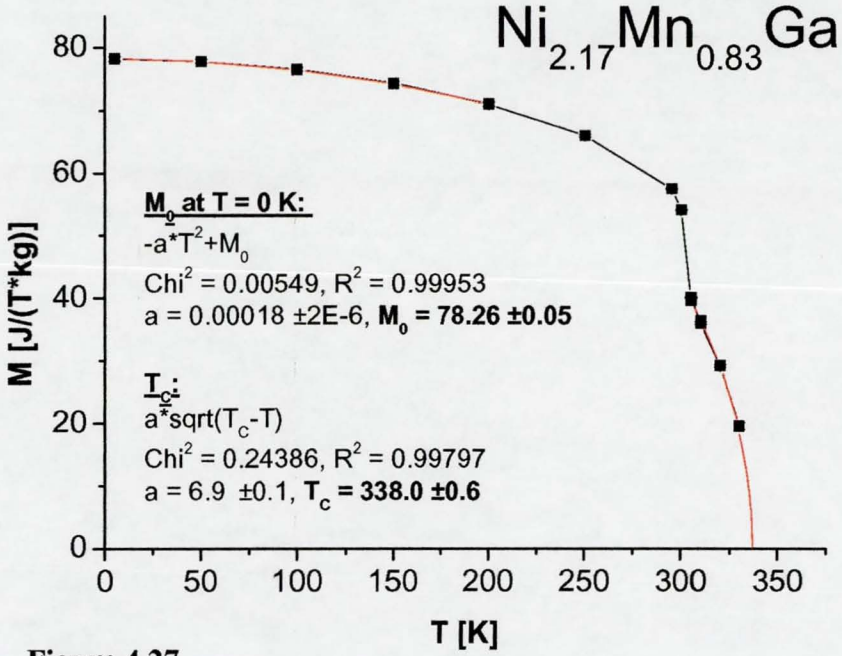

Figure 4.27

Magnetisation as a function of temperature of $Ni_{2.17}Mn_{0.83}Ga$ obtained from Arrott plots.

The magnetisation is presented in figure 4.25 and the Arrott plots of the same data are shown in figure 4.26. The thermal variation of the spontaneous magnetisation obtained from Arrott plots are given in figure (4.27). Fits of the low temperature data indicate that the ground state magnetisation is $M_0 = (78.3 \pm 0.2)\ \frac{J}{T \cdot kg}$. The ferromagnetic transition is determined to be $T_C = (338.0 \pm 0.6)$ K. An anomaly related to a structural phase transition occurs at T = 305 K.

A summary of the magnetic and structural transition temperatures as obtained from the zero applied field magnetisation and the temperature scans at 0.1 T is given in table (4.5).

Sample $Ni_{2+x}Mn_{1-x}Ga$		**structural transition** T_M	**magnetic transition** T_C [K]
X=0.05	Arrott plot	260 K	372 ± 2
	0.1 T	260 K	357.4 ± 0.2
X=0.10	Arrott plot	284 K	357 ± 1
	0.1 T	280 K	349.5 ± 0.2
X=0.17 (B)	Arrott plot	305 K	338.4 ± 0.3
	0.1 T	310 K	337.2 ± 0.5
X=0.17 (A)	Arrott plot	-	-
	0.1 T	330 K	339.2 ± 0.6

Table 4.5

Magnetic and nuclear transition temperatures obtained from temperature scans and Arrott plots.

With increasing Ni-content the structural transition temperature also increases, but the magnetic transition temperature decreases. This is consistent with the data obtained from the Arrott plots as well as with the data obtained from temperature scans at B = 0.1 Tesla.

Magnetic Moment and Spin

In order to calculate the magnetic moment m at zero applied field and $T = 0K$ the Arrott plots have been evaluated for each sample. The magnetic moment is calculated using the following formula:

$$m = \frac{M_0 \cdot m_w}{1000 \cdot N_A \mu_B \cdot C_{Mn}}, \qquad (4.8)$$

M_0 is the spontaneous magnetisation at T = 0 K in units of $\left[\frac{J}{T \cdot kg}\right]$,

m_w is the molar weight of the sample in units of $\left[\frac{g}{mol}\right]$,

$N_A = 6.022 \cdot 10^{23}$ is the number of atoms per mole,

$\mu_B = 9.27 \cdot 10^{-24}$ is the Bohr magneton in units of $\left[\frac{J}{T}\right]$ and

C_{Mn} is the content of Mn in one formula unit.

The spin S_z can be obtained from equation (4.8) using

$$m = g \cdot S_z . \qquad (4.9)$$

The effective magnetisation is given by

$$p_{eff}^2 = 4S(S+1). \qquad (4.10)$$

In table (4.6) the spontaneous magnetisation per Mn-atom in units of one Bohr magneton, the spin and effective magnetisation per Mn-atom are summarised. Here g was taken to be g = 2.

Sample $Ni_{2+x}Mn_{1-x}Ga$	$M_0 [\frac{J}{kgT}]$	$M [\mu_B]$	S_z	$p_{eff} [\mu_B]$
X = 0.05	86.2	3.94	1.97	4.83
X = 0.10	84.0	4.05	2.03	4.95
X = 0.17	78.3	4.10	2.05	5.00

Table 4.6

Magnetic moments obtained from Arrott plots.

4.4) Determination of the Structure of $Ni_{2.17}Mn_{0.83}Ga$ using Neutron Powder Diffraction

Introduction

At high temperatures, i.e. $T > T_M$, alloys with the composition $Ni_{2+x}Mn_{1-x}Ga$ have the cubic $L2_1$ Heusler structure. When the temperature is lowered below T_M the alloys undergo a martensitic phase transition to a structure with lower symmetry. Knowledge of the crystal structure at high temperatures enables appropriate candidates for the low temperature structure to be identified. Using symmetry and group theory a crystal lattice can be described using one of the 230 different space groups. The symmetry operations, which generate the atom positions within the unit cell, are elements of that particular space group. A phase transition will remove some of the symmetry elements such that the lower symmetry phase is characterised by a reduced set of symmetry operations. According to group theory there is a group – subgroup – relationship. Group **A'** is called a subgroup of group **A** if each element of **A'** is also present in group **A**. Since the subgroup usually contains fewer symmetry elements than its supergroup the removal of symmetry constraints allows more flexibility in the positioning of atoms and/or lattice parameters.

In order to identify an appropriate space group to describe the low temperature martensitic structure (which has a lower symmetry than the high temperature austenite) one has to start with the space group describing the high temperature phase. For $Ni_{2.17}Mn_{0.83}Ga$ this corresponds to $Fm\bar{3}m$ with a lattice parameter of $a = 5.79\,\text{Å}$. Reducing the symmetry means choosing a subgroup of the space group $Fm\bar{3}m$.

The choice of subgroup is guided by comparison with experimental observation. Usually the low temperature phase will have more Bragg peaks than the higher symmetry phase. The position of Bragg reflections will allow the translation symmetry of the lattice to be identified, while the actual intensity of a peak is mostly affected by the atom positions.

After having established the description of different phases at high and low temperatures by comparison with the experimental neutron diffraction patterns the transition region will be investigated in more detail. This will be followed by a discussion of the relationships between the various space groups relevant for the structure of $Ni_{2.17}Mn_{0.83}Ga$. A table will be given of atomic positions of the relevant space groups as a supplement to these discussions.

Experimental details

Neutron scattering diffraction experiments have been carried out on annealed powder samples at the ILL using the instrument D2b with a wavelength of 1.59 Å. The refinement was carried out using the FullProf program [1]. All parameters needed for the model calculation are contained in a file with extension pcr. A copy of the pcr-files used in the refinements is given in the appendix.

The diffraction experiments on $Ni_{2.17}Mn_{0.83}Ga$ have been carried out at different temperatures but otherwise under identical conditions and using the same diffractometer. Measurements were taken at T = 250 K, 295 K, 300 K, 305 K and 310 K. This temperature range covers the low temperature phase at 250 K and the high temperature phase at 310 K.

High temperature phase

At 310 K $Ni_{2.17}Mn_{0.83}Ga$ has a cubic $L2_1$ Heusler structure (fcc). It is well described using the space group $Fm\bar{3}m$ with lattice constant $a = (5.79 \pm 0.01)$Å. The accuracy of the lattice parameter is determined by the precision of the wavelength which is given by $\lambda = (1.59 \pm 0.01)$Å. The unit cell volume is V_{310K} = 194 Å^3. Since the magnetic transition temperature is close to 330 K the compound is still ferromagnetic at 310 K. Therefore magnetic as well as nuclear scattering has to be included for the neutron powder refinement. A model using the cubic $Fm\bar{3}m$ structure only accounted for all major peaks in the observed pattern but failed to predict intensity for two small peaks in the pattern. These additional peaks could be explained with the onset of the phase transition whereby the most intense Bragg reflections of the low temperature phase start to emerge from the background. The low temperature phase is most intense in the diffraction pattern measured at 250 K. It will be explored in a separate section. Including the low temperature phase in the powder refinement *R-factors* of less than 5 and less than 8 have been achieved for nuclear and magnetic scattering, respectively. This refinement had an overall χ^2 value of ≈ 7. Such a χ^2 value is a good indication for the quality of the fit and the accuracy of the proposed structures.

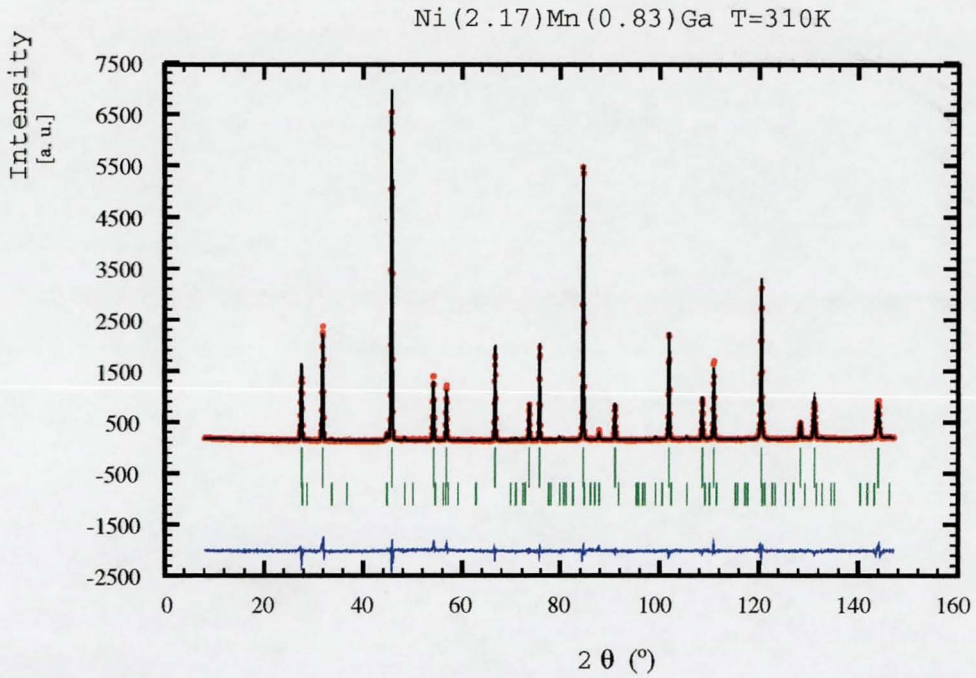

Figure 4.28

The experimental observation and the refinement of $Ni_{2.17}Mn_{0.83}Ga$ at 310 K is shown in the picture above. The red dots are the observed data points. The superimposed black line is the calculated model. The blue line below shows the difference between observation and calculation. The green bars indicate peak positions of Bragg peaks according to the phases used to describe the structure (from top to bottom: cubic nuclear, cubic magnetic and low temperature nuclear phase).

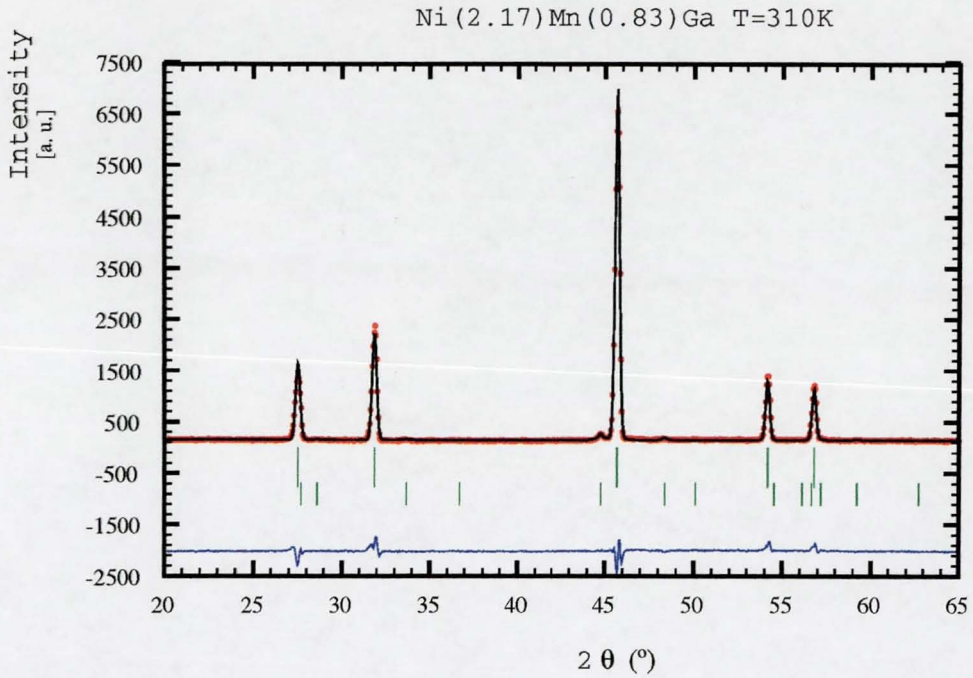

Figure 4.29

This picture shows a small section of the neutron diffraction patterns. At 45 ° in 2θ one can see a small peak emerging from the background. This peak is not accounted for by the cubic phase but it belongs to the low temperature tetragonal phase.

Occupation numbers for each atom type

The sample investigated here has the chemical composition $Ni_{2.17}Mn_{0.83}Ga$. Therefore there is a surplus of Ni- and a deficiency of Mn-atoms compared to stoichiometric Ni_2MnGa. It is assumed that the surplus Ni-atoms occupy vacant Mn-sites. Thus the effective occupation of Mn-sites is 0.83 Mn and 0.17 Ni.

In the pcr-file, one can find the occupation value of each lattice site under the heading "occ". This value accounts for the actual occupation of atoms on their respective lattice sites. The occupation of atoms can be refined using the FullProf program according to the experimental observation. It is generally expected that the occupation numbers will mirror the

composition of the samples. Therefore for Ni_2MnGa one would expect to have the occupation numbers:

Ni	2.00000
Mn	1.00000
Ga	1.00000

Table 4.7
Occupation numbers for Ni_2MnGa.

The deviation in composition for $Ni_{2.17}Mn_{0.83}Ga$ can be modelled either by having an occupation of Mn (0.83) and Ni (0.17) on the Mn-sites or, alternatively, by an effective Mn occupation. This effective occupation has to take into account the difference in scattering lengths of Mn and Ni. Therefore the effective Mn occupation of the manganese position is given by

$$\tilde{p}_{Mn}^{eff} = \frac{p_{Mn} \cdot b_{Mn} + p_{Ni} \cdot b_{Ni}}{b_{Mn}}, \qquad (4.9)$$

where $p_{Mn/Ni}$ is the occupation of the manganese site with manganese and nickel atoms, respectively. Using $b_{Mn} = -0.373 \cdot 10^{-12}\ cm$ and $b_{Ni} = 1.03 \cdot 10^{-12}\ cm$ [2] one obtains $\tilde{p}_{Mn}^{eff} = 0.36056$ as the effective occupation of Mn on Mn-sites. In essence this occupation number takes into account the surplus of nickel atoms in the alloy. The scattering length of gallium is given by $b_{Mn} = 0.7288 \cdot 10^{-12}\ cm$ [6]. For the refinement of the magnetic scattering contribution the Mn-site occupation has to be fixed to 0.83 per Mn-site. This assumes that Mn carries a moment and that any Ni atom located on the Mn-site does not.

For a ferromagnetically ordered sample the ferromagnetic scattering contribution can be treated as an additional phase. The unit cell of the magnetic phase is the same as for the nuclear scattering, but only Mn-atoms are included as magnetic atoms. In addition the scale factors of the two phases have to be matched. This is done by adjusting the occupation numbers. The occurrence of each kind of atom (more general: atom position) has to be divided by the number of symmetry elements within the space group. By taking the ratio of these two parameters (occurrence of atom position / number of symmetry elements) for both nuclear and magnetic phases, and for all atoms, the same overall scale factor can be used for both contributions.

Values of occupation numbers for the atom positions of $Ni_{2.17}Mn_{0.83}Ga$ are given in the table below for the cubic space group $Fm\bar{3}m$:

atom (atom position)	according to one formula unit (nuclear)	according to symmetry elements (nuclear)	according to symmetry elements (magnetic)
Ni	2.00000	0.416666	
Mn	0.36056	0.075117	8.300000
Ga	1.00000	0.208333	

Table 4.8

Occupation numbers for $Ni_{2.17}Mn_{0.83}Ga$.

The occupation numbers in table (4.8) are listed according to two different models. The second column shows the occupation numbers of Ni, Mn and Ga in terms of one formula unit. Here 0.36056 is the effective Mn-atom occupation of Mn-sites. The third and fourth columns display

the occupation numbers in terms of symmetry elements describing the full symmetry of the unit cell. At high temperatures the nuclear structure of $Ni_{2.17}Mn_{0.83}Ga$ is described using the space group $Fm\bar{3}m$. This space group contains a total of 192 symmetry elements. The unit cell contains 4 Mn atoms at position (4a) in the unit cell at (0, 0, 0). The ratio of $4 \cdot \tilde{p}_{Mn}^{eff}$ to 192 yields 0.0075117. This is the occupation number for a Mn-site. The magnetic unit cell contains only Mn atoms. The set of symmetry operations can be reduced to 4 symmetry elements. The ratio of 4 to 4 yields one. This has to be multiplied with the actual occupation of Mn sites by Mn atoms. Thus in the magnetic unit cell the occupation number of Mn sites is 0.83.

Magnetic moment obtained from the diffraction experiment

The magnetic moment obtained from the refinement at 310 K is $(1.54 \pm 0.06)\mu_B$ per Mn-atom. This takes into account the occupation of Mn atoms on Mn sites. The value of the magnetic moment has to be compared to the moment obtained in magnetisation measurements. Using Arrott plots for 310 K a magnetisation of (36.0 ± 0.3) $\frac{J}{kg \cdot T}$ is obtained. This value corresponds to a magnetic moment of (1.89 ± 0.02) μ_B per Mn-atom. Thus the magnetic moment is higher for the macroscopic magnetic moment by a margin which is significantly larger than the errors of the individual measurements.

In order to resolve this discrepancy the observations by Brown et al. [7] have to be consulted. Brown et al. measured the magnetisation density in Ni_2MnGa at 100 K and 230 K. The diffraction experiment allowed the determination of lattice site-specific magnetic moments. For a

measurement at 230 K and under the assumption that Ga does not carry a magnetic moment a Ni-moment for Ni-atoms located on Ni-sites was refined. Its magnitude was determined as 0.22 μ_B. For the Mn-moment a value of 2.30 μ_B was obtained.

It is not unreasonable to assume that a similar situation prevails for the Ni-rich compounds. Thus the difference may be attributed to a Ni-atom polarisation parallel to the Mn moment and with a magnitude of ≈ 0.09 μ_B per Ni-atom on Ni-sites. The temperature of 310 K is higher than the temperature at which the measurement in [7] was carried out. The smaller Mn moment and the reduced moment on Ni-sites is therefore consistent with the measurements on pure Ni_2MnGa.

Including a small moment on Ni-sites for the neutron refinement is not feasible, as the sensitivity of the powder refinement for such a small moment is not sufficient. Macroscopic magnetisation measurements, however, are sensitive to the total moment. Such a moment will also include a contribution from Ni-atoms should these atoms carry a magnetic moment. It is therefore concluded that under the assumption of a small magnetic moment on Ni-atoms, which are located on Ni-sites, the macroscopic magnetisation measurements and the neutron results are in good agreement.

Low temperature phase

Below the martensitic transformation temperature, at T = 250 K, $Ni_{2.17}Mn_{0.83}Ga$ has a tetragonal non-modulated body centred structure. The atomic arrangement can be described well using the space group $I4/mmm$. This is the same low temperature phase which started to emerge in the diffraction pattern at 310 K. On transforming from the high temperature cubic phase to the low temperature tetragonal phase the lattice parameters undergo a significant change in length.

As discussed above, at high temperatures $Ni_{2.17}Mn_{0.83}Ga$ has a fcc Heusler structure with the space group $Fm\bar{3}m$. A subgroup of $Fm\bar{3}m$ is the tetragonal body centred space group $I4/mmm$. The tetragonal setting can be constructed from the Heusler structure by choosing a different unit cell. The construction is indicated graphically in figure (4.30). The new unit cell is body centred and it contains two formulae units per unit cell. This is only half the number of atoms compared to the fcc unit cell. Figure (4.30) shows an arrangement of 4 cubic unit cells (top view) using a solid line, while a broken line indicates the unit cell for the setting of space group $I4/mmm$. The lattice parameters of the tetragonal cell are $a_{tetra} = b_{tetra} = \frac{1}{\sqrt{2}} a_{cubic}$ and $c_{tetra} = a_{cubic}$.

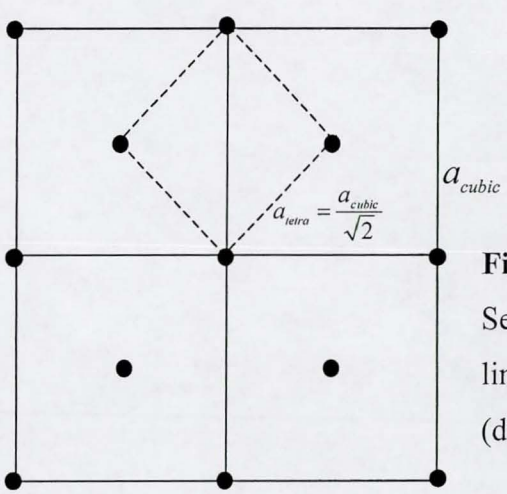

Figure 4.30
Setting of 4 face centred cubic (solid line) cells and one tetragonal cell (dashed line).

For the tetragonal setting the explicit value of the lattice parameters of the high temperature phase would be:

$$a_{tetra} = b_{tetra} = \frac{5.79}{\sqrt{2}} = 4.09\text{Å}$$
$$c_{tetra} = c_{cubic} = 5.79\text{Å} .$$

The diffraction pattern taken at a temperature of T = 250 K indicates that the low temperature phase can be described using a tetragonal unit cell as given above. However, the lattice parameters are drastically changed. Lattice parameters for the low temperature martensite were refined to:

$$a' = b' = (3.87 \pm 0.01)\text{Å}$$
$$c' = (6.47 \pm 0.01)\text{Å} .$$

The correctness of the description is mirrored by *R-factors* of 4.2 for both nuclear and magnetic scattering.

Although the low temperature phase is described correctly using a tetragonal unit cell at low temperatures and despite the neutron diffraction measurement having been carried out at a temperature of T = 250 K (a temperature significantly lower than the martensitic transition temperature of T_M = 301 K) some minor Bragg peaks remain unaccounted for by such a model. Therefore a contribution was included of the intermediate meta-stable phase which has been identified in diffraction patterns at temperatures located within the martensitic transition region. This phase essentially accounted for the additional peaks both in intensity as well as in peak position. The details of diffraction pattern in the transition region and the intermediate phase will be discussed in the following section. For the pattern at T = 250 K including both the low

temperature tetragonal phase as well as remnants of the phase identified for the transition region resulted in an acceptable fit. For the refinement a χ^2 -value of $\chi^2 \approx 9$ was obtained. The *R-factor* for the refinement of the low temperature phase is $R \approx 4$, while for the intermediate phase a value of $R \approx 11$ was obtained. These results indicate that the model for the intermediate phase is able to account for all significant features of the pattern, such as peak positions and intensities of Bragg reflections. However, some finer aspects (mainly connected to the form of Bragg peaks of the intermediate phase) remain unresolved. This shortcoming is responsible for the slightly enhanced χ^2-value at 250 K. However, the overall analysis shows that the structural model proposed here for the low temperature phase is the correct description.

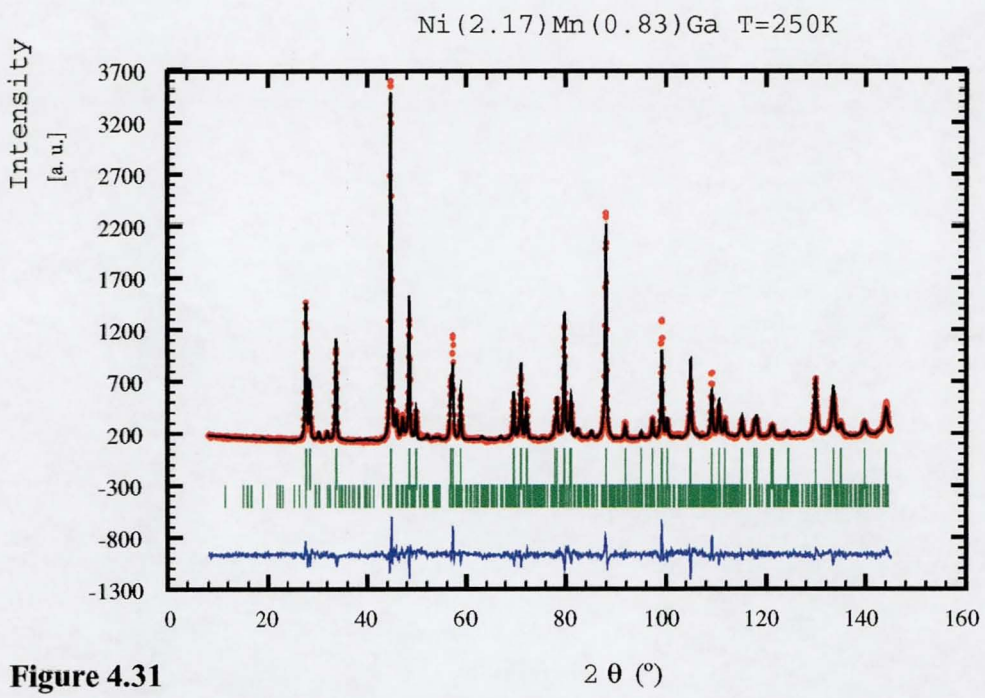

Figure 4.31

Neutron diffraction pattern of $Ni_{2.17}Mn_{0.83}Ga$ at 250 K. The model comprises the low temperature tetragonal phase (nuclear and ferromagnetic contributions) as well as a small contribution arising from the intermediate phase. This phase is a meta-stable phase which persists down to 250 K.

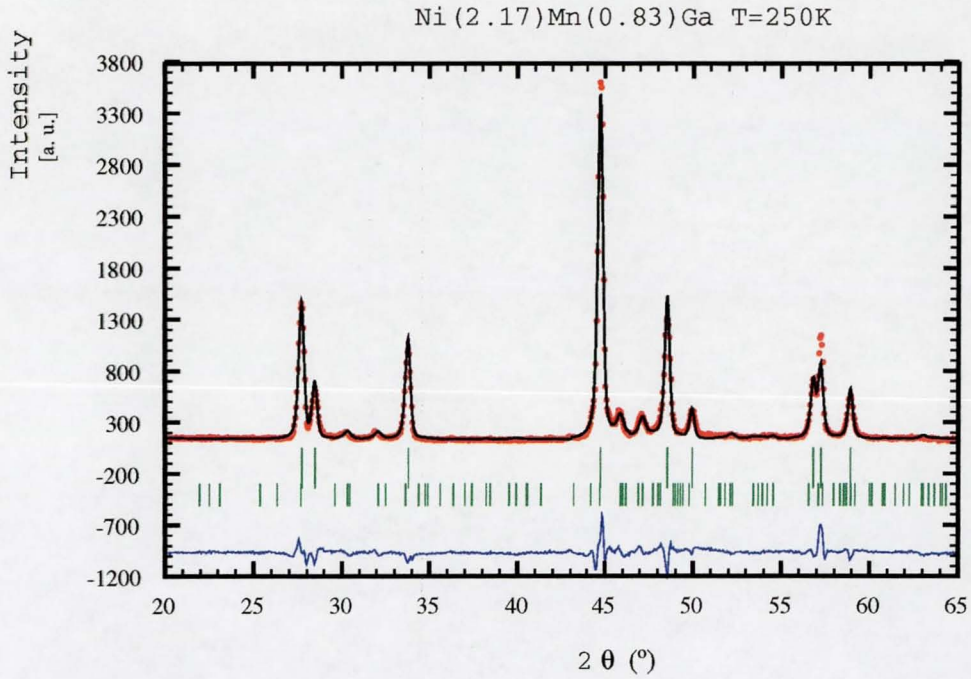

Figure 4.32

Low angle section of the diffraction pattern of figure (4.30). The major peaks arise due to the low temperature tetragonal phase, while the small additional reflections arise due to remnants of the intermediate phase.

Details of all the refined parameters can be read off the pcr file given in the appendix. For the low temperature tetragonal phase the length of the a- and b-axes decreases by 5.5 % in relation to the cubic phase, whereas the length of the c-axis increases by 11.7 %. The volume of the cubic austenite unit cell (194.10 $\AA^3$ at T = 310 K) corresponds well to the volume of the tetragonal martensite (96.90 $\AA^3$ at T = 250 K). A factor of 2 arises in the volume of these unit cells because the tetragonal unit cell contains only half as many atoms as the fcc unit cell.

It should be noted that the change in length of the lattice parameters is huge. However, almost no change is observed in the volume of a unit cell. Such a feature is connected with the details of the martensitic phase transformation. The martensitic phase transition is diffusionless and evolves via sheer displacement of atomic planes. For pure Ni_2MnGa the

transformation details have been investigated by Brown et al. [4]. For comparison the observed length changes in pure Ni_2MnGa are 2 % for the a- and b-axes and of 5 % for the c-axis. It has to be noted that the changes in length have a different sign. For pure Ni_2MnGa the c-axis shortens on transforming to the low temperature phase, while for $Ni_{2+x}Mn_{1-x}$ Ga the c-axis lengthens. For both compounds the volume of the unit cell per formula unit is not appreciably changed by the martensitic transformation.

The low temperature martensitic phase is different from that of the pure compound. At low temperatures Ni_2MnGa exhibits a 7-fold increase of the tetragonal unit cell and is orthorhombic, whereas the low temperature structure of $Ni_{2.17}Mn_{0.83}Ga$ can be explained by the non-modulated tetragonal structure.

The magnetic moment obtained from the diffraction experiment

The magnetic moment of Mn obtained from the refinement of the diffraction pattern at T = 250 K is $(2.05 \pm 0.06)\mu_B$/per Mn-atom. This value is larger than the value obtained at 310 K. This arises due to an increase in the degree of magnetic order when lowering the temperature. A comparison with the magnetisation data obtained from the Arrott plot at 250 K yields a magnetisation of (66 ± 1) $\frac{J}{kg \cdot T}$. This corresponds to (2.87 ± 0.04) μ_B/per Mn-atom.

The value of the magnetic moment obtained in the neutron scattering experiment is consistent with the value of 2.30 μ_B/Mn-atom obtained by Brown et al. [7] for pure Ni_2MnGa at a slightly lower temperature of 230 K. However, the magnetic moment deduced from magnetisation data

is significantly larger. If the model of a Ni-moment is adopted a Ni-moment on Ni-sites of 0.49 μ_B/Ni-atom is obtained. This value is substantially larger than the value deduced at the temperature of 310 K. However, as the high field part of the magnetisation curve has been used to extract the spontaneous magnetic moment it is possible that the application of a strong external magnetic field has changed the distribution of magnetic domains in favour of those domains which have their magnetic moments aligned close to the external magnetic field direction. Such a redistribution of domains would give rise to an enhanced value of the magnetic moment. In view of the variation of the magnetic moment in the low temperature martensitic phase on the conditions under which the magnetisation measurements have been carried out (see figures (4.14) and (4.15)) the macroscopic magnetic moment values in the martensitic phase have to be interpreted with care. Variations of up to 15 % are observed at 250K in figures (4.14) and (4.15).

Description of the intermediate phase in the region of the martensitic phase transition

The phase transition

The temperature dependence of diffraction patterns obtained in the transition region between 250 K and 310 K is shown in figure (4.33). A close inspection reveals that there are at least three phases present within the transition region. First some simple characteristics of these phases will be explored in more detail. Based on the temperature dependence of Bragg peaks in figure (4.33) their assignment to various phases is given.

For T = 310 K pattern the (2 0 0) Bragg peak occurs as a dominant feature at an angle of $\approx 32^{\circ}$ in 2θ. On cooling to 305 K the intensity of this peak drops slightly, and on further cooling to 300 K the intensity falls more rapidly towards zero. Its intensity diminishes but the peak intensity does not go to zero completely, even at a temperature of 250 K. This arises due to the fact that as the proportion of the cubic phase decreases a Bragg reflection of a low temperature phase emerges close to the position of the cubic (2 0 0) peak.

For the diffraction patterns at low temperatures a strong peak is also observed at a 2θ angle of 34°. However, with increasing temperature the peak intensity diminishes and merges into the background. At 310 K the peak intensity is essentially zero. The peak intensity is maximal at T = 250 K. Since at 250 K it is the low temperature phase that prevails it is argued that the peak at 34° in 2θ belongs to the low temperature phase.

In addition to the characteristics described above there are some smaller peaks, which appear only in an intermediate temperature range. These peaks are found to have substantially smaller intensities at high and at low temperatures as compared to a temperature located within the martensitic transition region.

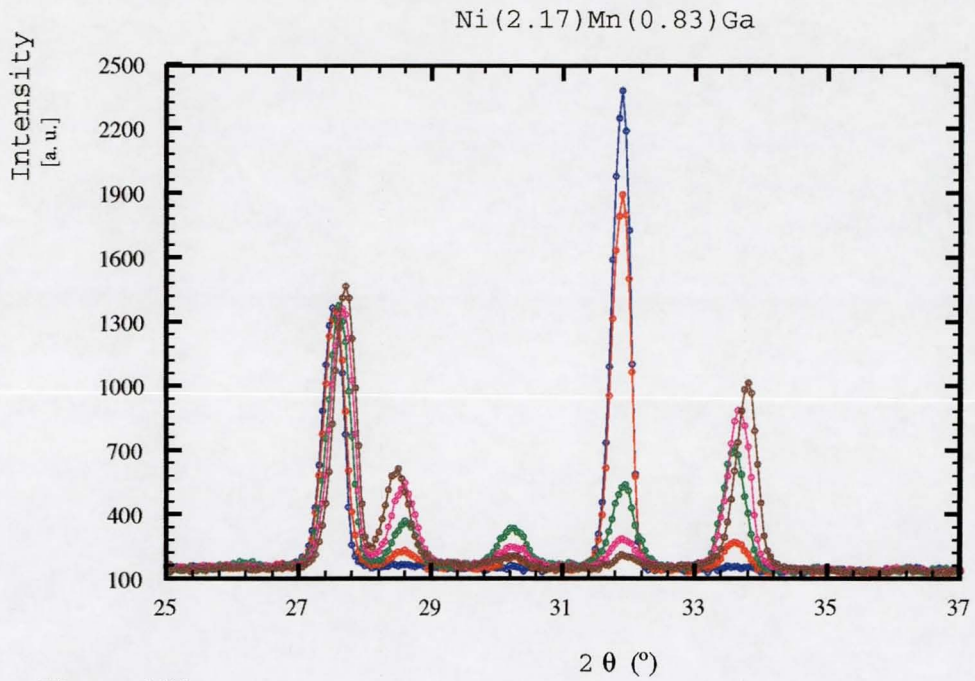

Figure 4.33

Temperature dependence of the low angle part of the neutron diffraction of $Ni_{2.17}Mn_{0.83}Ga$ in the martensitic transition region. The blue line shows the data observed at 310 K. The red line was measured at 305 K, the green line displays at 300 K, the pink line at 295 K and the brown line at 250 K.

For the interpretation of the additional peaks two different models can be invoked. For the first model a modulation of one phase can be considered. This modulation, e.g. via an increase of the unit cell as for the pure Ni_2MnGa compound, will yield additional Bragg reflections. If the modulation amplitude is small, those Bragg reflections, which reflect the change in symmetry of the unit cell, will also have low intensity. Alternatively, a model can be considered where the transition occurs via an intermediate phase. Due to the huge, but reversible, changes in lattice parameters between the low and high temperature phases of $Ni_{2.17}Mn_{0.83}Ga$ this is a real possibility.

Both models have been used as a working basis for the interpretation of the diffraction pattern in the transition region. Best agreement between a

model and observation was obtained using a combination of high temperature cubic phase, a low temperature tetragonal phase and an intermediate phase of orthorhombic symmetry. A modulation model, based either on the high temperature cubic or the low temperature tetragonal phases, had only limited success in accounting for the observed diffraction patterns. The best results were obtained using a combination of an additional intermediate phase plus a modulation. Details of the various models are given next.

The structure of the intermediate phase

The intermediate phase, which is of orthorhombic structure, is a distorted phase exhibiting a two fold modulation along the $[100]_{cubic}$ and $[010]_{cubic}$ axes. Almost all peaks, which are could not be accounted for by the high or low temperature phases, can be assigned using the intermediate phase described by the face centred space group *Cmmm*. The lattice parameters used are $a = 10.99$ Å, $b = 11.51$ Å and $c = 6.08$ Å. However, the calculated intensities at the observed peaks do not fully account for the observed peak intensities.

The second model based on a 5-fold modulation along the $[110]_{cubic}$ – axis with space group *Immm* and lattice parameters $a = 4.09$ Å, $b = 20.45$ Å and $c = 5.79$ Å is able to generate peaks with proper intensity at positions which were not fully captured within the model discussed above. A combination involving both models provides a good basic description yielding an overall $\chi^2 \approx 20$. Within the transition region no other model, which has been put forward in the literature, comes as close to the observed structure of $Ni_{2.17}Mn_{0.83}Ga$ as the one proposed here.

Next the neutron diffraction pattern at T = 300 K is shown. The black line is the calculation based on the models described above.

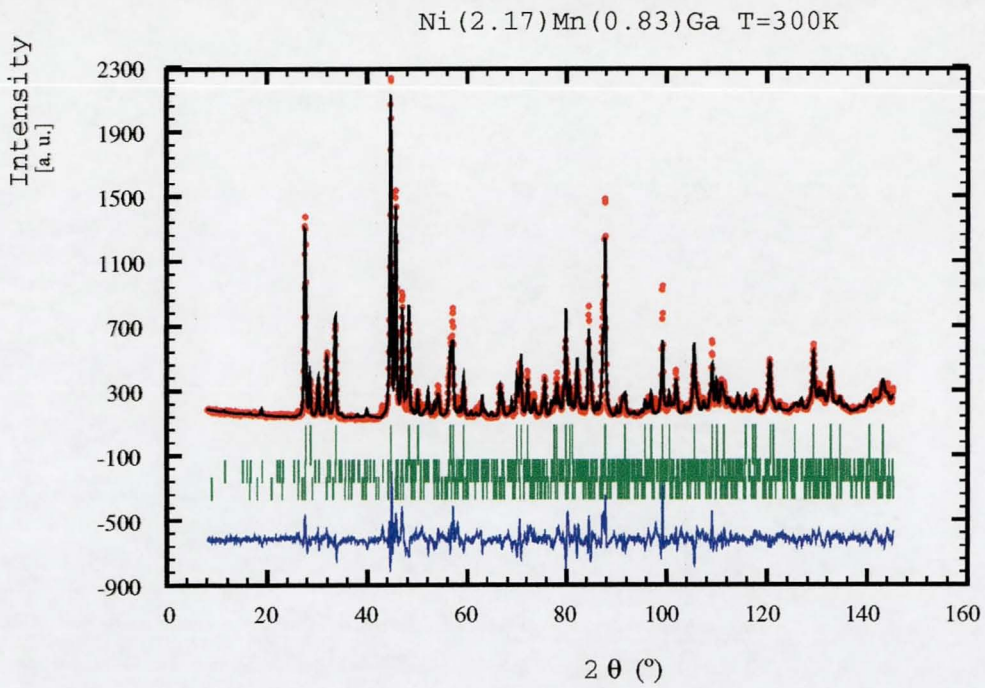

Figure 4.34

The calculated pattern based on the model of two intermediated phases described above is superimposed on the observed neutron diffraction pattern at 300 K. The green bars show the peak positions of each phase. The phases included are (from top to bottom): low temperature nuclear phase, low temperature magnetic phase, orthorhombic intermediate phase, cubic 5-fold modulated intermediate phase.

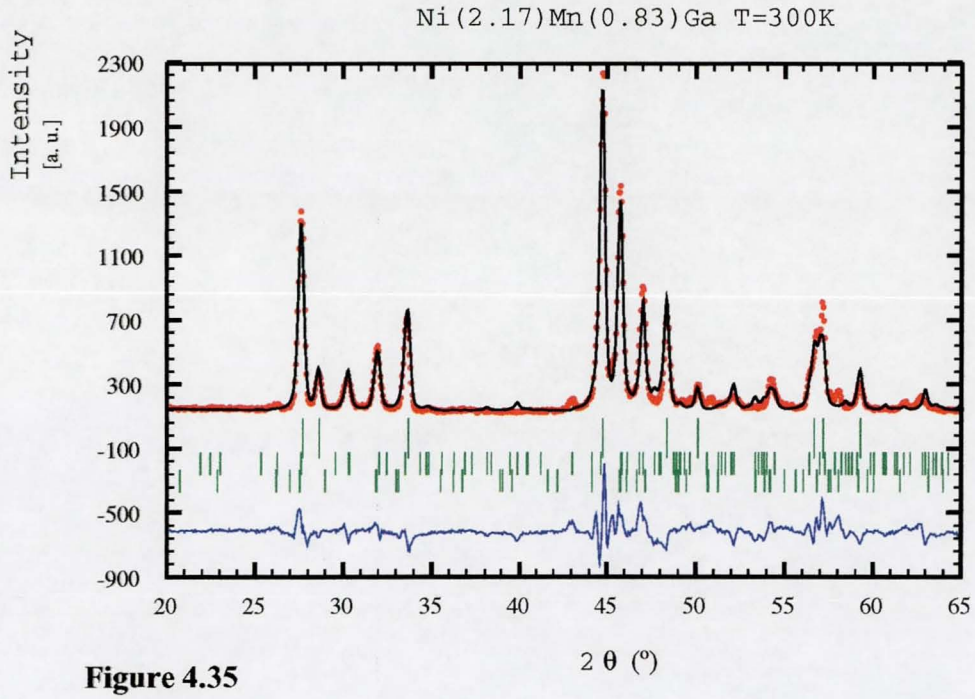

Figure 4.35

A section of the superposition of the observed and calculated pattern at T = 300 K.

An attempt to use only one phase as the intermediate phase was not successful. The best model description is obtained using an orthorhombic and the intermediate 5-fold modulated cubic structures. Also choosing a monoclinic [8, 9] or hexagonal structure as the intermediate phase have not resulted in an improvement on the model discussed above. Indeed a monoclinic model as proposed by [8] for a similar composition had significantly worse χ^2 values compared to the best model involving 2 intermediate phases. Models based on a different increase of the unit cell, i.e. a five-, seven-, ten-, or even twelve fold modulation, as proposed by [10], have been tried, but no satisfactory agreement with experimental observations could be obtained.

Towards an Understanding of the processes involved in the martensitic phase transition

The martensitic phase transition in $Ni_{2.17}Mn_{0.83}Ga$ is significantly different to that of Ni_2MnGa. Therefore the structure of the low temperature phases and the pre-martensitic phases of these two compounds are not implicitly related to each other. However, the high temperature phases have cubic face centred symmetry and can be described within the same space group using slightly different lattice constants.

In the stoichiometric case the pre-martensitic as well as the martensitic phase of Ni_2MnGa can be described using the orthorhombic space group *Pnnm* by a n-fold modulation along the $[110]_{cubic}$ axis (where $n = 3$ for the pre-martensitic phase and $n = 7$ for the martensitic phase at low temperatures). Therefore the martensitic transformation of the pure compound is driven by a rearrangement of atoms within the tetragonal unit cell. For the non-stoichiometric $Ni_{2.17}Mn_{0.83}Ga$ the martensitic transformation takes place by first shifting the atoms within the cubic Heusler setting. This is then followed by contraction and expansion of the lattice parameters resulting in a drastic loss of symmetry elements. The cubic high temperature phase has been described using the space group $Fm\bar{3}m$ containing 192 symmetry elements. The orthorhombic unit cell of the second intermediate phase has been described using the symmetry of the space group *Cmmm* which is characterised by 16 symmetry elements. This is a reduction by factor 12. The second intermediate phase is transformed into the low temperature tetragonal phase. The low temperature phase has been described using the space group $I4/mmm$ which contains 32 symmetry elements. This implies that the dramatic loss

of symmetry elements is followed by a new gain of symmetry elements on lowering the temperature towards 250 K. Such a sudden loss and regain of symmetry elements is unusual, but it is consistent with the interpretation of the intermediate phase being meta-stable.

In $Ni_{2.17}Mn_{0.83}Ga$ the transformation takes place over a large temperature range. Although the martensitic transformation start temperature obtained from magnetisation measurements is $\approx$ 305 K the neutron diffraction data show that a small amount of the low temperature martensitic phase is already present at 310 K. Furthermore at 250 K the coexistence of two phases (the low temperature and the orthorhombic intermediate phase) has been established. Therefore the martensitic transformation (on cooling) covers at least the temperature range between 310 K and 250 K. This, too, is different from the martensitic transformation observed for Ni_2MnGa, in which case the transformation from the pre-martensitic to the low temperature phase takes place "instantly" [4] without the involvement of an intermediate phase.

The distortion observed for Ni_2MnGa is 4.6% along the c-axis, 1.7 % along the b-axis and 2.4 % along the a-axis [4]. This is remarkably in itself but still less than those observed for $Ni_{2.17}Mn_{0.83}Ga$, where length changes were found to be twice as big. An overview over the observed length changes for $Ni_{2.17}Mn_{0.83}Ga$ is presented in table (4.9) and figure (4.36).

	Cubic	Intermediate (no doubling)	Tetragonal
a [Å]	5.790	5.495	5.473
b [Å]	5.790	5.755	5.473
c [Å]	5.790	6.080	6.466
Volume [Å^3]	194.1	192.3	193.7

Table 4.9

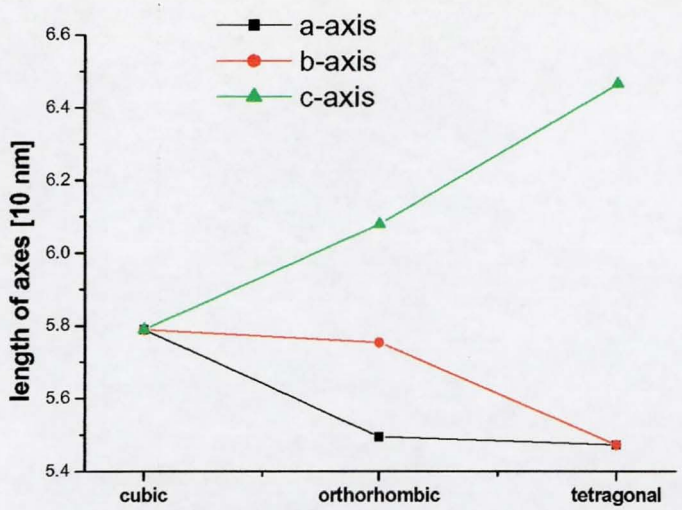

Figure 4.36

The lattice parameters as a function of the phase.

Figure (4.36) shows that the high length changes observed for $Ni_{2.17}Mn_{0.83}Ga$, and which are needed for the transition from the high temperature phase to the low temperature tetragonal structure, are realised by stepping towards the other phase via an intermediate structure. On cooling the cubic phase the length of the b-axis remains almost unaltered while the length of the c-axis is changed by half the length change involved for this axis in the whole martensitic transformation. The a-axis changes such that the volume of the unit cell is effectively constant for the first transformation step. For the second step, i.e. when transforming from the intermediate phase to the low temperature tetragonal phase, the

c-axis changes again by a similar amount as in the first transition step. The a-axis remains unchanged in length for the second transformation step, while the b-axis changes its length to coincide with the length of the a-axis. Thus the whole transformation process is split into 2 transition steps. This step-wise martensitic phase transformation as observed for $Ni_{2.17}Mn_{0.83}Ga$ enables these enormous length changes to occur while at the same time keeping the volume of the unit cell unchanged.

Details of the transformation have been checked using X-ray scattering as a function of temperature. However, only the neutron data has been used and presented here due to its superior quality.

Details of the refinement and additional information on the phases involved in the refinement can be found in the pcr-files. These have been used as input files for the refinement using the FullProf- programme. The files are attached in the appendix and should be consulted for more detailed information on particular parameters.

References:

[1] The electrical resistivity of metals and alloys: P. L. Rossiter, Cambridge Solid State Science Series, 1991

[2] Solid State Physics: N. W. Ashcroft, N. D. Mermin, HRW International Editions, 1976

[3] The Electronic Structure of Rare-Earth Metals and Alloys: the Magnetic Heavy Rare-Earths: B. Coqblin, Academic Press, 1977

[4] P. J. Brown, J. Crangle, T. Kanomata, M. Matsumoto, K.-U. Neumann, B. Ouladdiaf, K. R. A. Ziebeck, J. Phys.: Condensed Matter **14**, 10159-10171, 2002

[5] M. Matsumoto, T. Takagi, T. Kanomata, N. Muramatsu, A. N. Vasil'ev, Mater. Science and Engineering **A273-275**, 1999, 326-328

[6] Thermal neutron scattering length and cross sections for condensed matter research: V. F. Sears, Chalk River Nuclear Laboratories, 1984

[7] P. J. Brown, A. Y. Bargawi, J. Crangle, K.-U. Neumann, K. R. A. Ziebeck, J. Phys.: Condensed Matter **11**, 4715-4722, 1999

[8] K. Inoue, K. Enami, M. Igawa, K. Inoue, Y. Yamaguchi, K. Ohoyama, Proc. of the int. Conf. on Solid-Solid Phase Transf., 1120-1123, 1999

[9] Ni Excess and Electronic Structures of Multi Functional $Ni_{2.17}Mn_{0.83}Ga$, S. Ishida, M. Furugen, S. Asano, Int. J. Appl. Electromagn., 12, 14360-14365, 2000

[10] K. Oikawa, T. Ota, T. Ohmori, Y. Tanaka, H. Morito, A. Fujita, R. Kainuma, K. Fukamichi, K. Ishida, Appl. Phys. Lett., 81, 5201-5203, 2002

5) Discussion

The investigations in this thesis have centred on Ni rich samples of composition $Ni_{2+x}Mn_{1-x}Ga$ with $0 < x < 0.2$. For samples within this compositional range ferromagnetic order exists and a martensitic phase transition is observed within the ferromagnetically ordered state. Structural investigations using X-ray and neutron scattering have been used in order to clarify the crystallographic details of the various phases. While for the pure Ni_2MnGa compound a transition to a low temperature modulated structure is observed, for the Ni-rich compound with $x = 0.17$ the transition occurs to a tetragonal structure. In the transition the length of the axes change substantially. However, for the pure Ni_2MnGa compound the c-axis shortens, while for the $x = 0.17$ alloy it lengthens. This implies that the mechanism is slightly different for the Ni-rich compound. The shears driving the martensitic phase transition for pure Ni_2MnGa have been identified by Brown et al. For $x = 0.17$, however, the mechanism must be different, as the deformation leaves the c-axis lengthened rather than shortened. On the basis of the neutron diffraction data taken on a powder it was feasible to make detailed statements regarding the transition mechanism. However, measurements in the transition region and as a function of temperature indicate that an intermediate phase is involved. This phase has orthorhombic symmetry with lattice parameters which can be considered to be 'in between' the high temperature cubic and the low temperature tetragonal phases. Such an intermediate phase seems to assist in the completion of the martensitic phase transition. For all Ni_2MnGa compounds the unit cell volume does not change appreciably in the phase transition. This lends support to the notion that volume conserving shears are responsible for this phase

transition. For the x = 0 compound this has been shown by single crystal investigations. It will be of interest to see whether or not this is also the case for the Ni-rich compounds.

The presence of an intermediate phase in the martensitic phase transformation process also contributes to the hysteretic nature of the phase transformation. This has been evidenced in DSC measurement with a considerable difference in transition temperatures observed while heating and cooling. These measurements support the interpretation of the phase transition as being of 1st order by the observation of a considerable temperature hysteresis and by the observation of a latent heat contribution to the DSC measurements. For the transition itself magnetisation measurements are more sensitive. SQUID measurements reveal a much sharper feature for the martensitic phase transformation than DSC measurements.

The magnetisation of Ni-rich samples reveals that the structural changes are coupled to the ferromagnetism of the sample. Structural transitions are evidenced by a change in the magnetisation either as a step feature or a kink. Large fields are able to align crystallographic domains due to forcing the magnetic moment into the external magnetic field direction. This change of magnetic moment direction is accompanied by a change of the orientation of the crystallographic domain. The axes are redistributed such that the easy axis of magnetisation is oriented closer to the external magnetic field direction. The observations in magnetisation measurements support this point of view. However, it is surprising that the coupling to the lattice is so strong for these compounds. The magnetic moment of Mn-atoms is dominated by the electronic spin contribution. In order to couple the spin to the lattice degrees of freedom an orbital

moment contribution is also needed. Both the spin and the orbital contributions are coupled to one another via the spin orbit coupling constant. This constant is of relativistic origin, and its value is expected to be small for 3d transition metals. However, from an experimental point of view the magnetic moment is found to be strongly coupled to the lattice. This may be assisted firstly by the fact that the energy barrier for the motion of crystallographic domain walls is particularly low, and secondly by the observation that the anisotropy develops in the low temperature phase, for which the crystallographic symmetry is reduced from the cubic structure at high temperatures.

Brown et al. have also proposed that the martensitic phase transformation for pure Ni_2MnGa is driven by a band Jahn-Teller effect. Such a mechanism would, of course, give rise to some anisotropy due to changes in the symmetry of the electron distribution in the phase transformation. An external magnetic field of sufficient magnitude could influence the distribution of magnetic electrons on the symmetry adapted orbitals located on the Mn-atoms. Within such an interpretation the coupling would arise due to a magnetic field induced shifting of energy levels on manganese, akin to a crystal field splitting. This splitting is then exploited by the lattice such that it adopts a more favourable configuration with an overall reduction in the free energy of the system. It will be of interest to investigate the changes of the magnetisation density on undergoing the martensitic phase transformation. For such an experiment single crystal magnetic form factor measurements have to be carried out. It is expected that such an experiment is entirely feasible as the changes in lattice parameter are even larger for $Ni_{2.17}Mn_{0.83}Ga$ than for the pure Ni_2MnGa compound, thus allowing the contribution of various low temperature crystallographic domains to be separated from one another.

In this context it is of interest to observe that resistivity measurements have a temperature dependence more consistent with an electronic scattering mechanism than with a lattice contribution. This indicates that those electrons responsible for the conduction of an electrical current are also strongly influenced by the magnetic moments located on Mn-atoms. For a magnetic moment of fixed magnitude the influence is exerted via a contact polarisation. For such a case the simple model used for the analysis of the electric resistance measurement is expected to be a reasonable model. If, however, the manganese d-electrons participate at the Fermi surface it is not possible to readily disentangle their contribution to the conduction current. However, the correct analysis of the resistivity data requires more information than is available at present.

The nature of the magnetic moment can be, at least partly, inferred from neutron and magnetisation measurements. The values obtained from magnetisation measurements for the value of the ground state magnetic moment seems to indicate that the moment is not an integer multiple of a Bohr magneton. This interpretation, however, rests on the assumption that the magnetic moment is only carried by manganese atoms. As indicated above in the discussion of the magnetisation data, there are some strong hints of a small, but non-zero, magnetic contribution of Ni-atoms located on Ni-sites. The measurement at T = 310 K and the small difference between magnetic moments determined using magnetisation and neutron data is strongly supportive of such an interpretation. The much larger discrepancy at T = 250 K is less certain due to the effect a strong magnetic field has on the alignment of crystallographic domains. Thus the strong field magnetisation measurement will overestimate the magnetic moment due to the deviation of crystallographic domains from a

random and spherical distribution in the sample. Based on this observation the magnetisation measurements will overestimate the size of the magnetic moment. Neutron measurements do not need an external magnetic field and as a consequence they do not suffer from the problems highlighted here for the magnetisation measurements.

This open question of a magnetic moment located on Ni-atoms can also be answered by magnetic form factor measurements. Here site-specific magnetisation values can be determined. Such a magnetisation density determination experiment carried out on a Ni-rich Ni_2MnGa sample will be a very revealing and informative experiment.

The physics of the Ni-rich Ni_2MnGa samples has been investigated in some detail. Structural and magnetic properties have been determined for a variety of samples and under various conditions. The characteristics of the magnetic and martensitic phase transformations have been investigated. The huge changes of the lattice parameters observed for the $x = 0.17$ compound are surprising. In particular in view of the fact that such form and length changes can also occur in bulk materials and single crystal without a degradation of the material. The observation that the transformation takes place via an intermediate phase gives some clues as to the mechanism via which the phase transformation takes place. The coupling of the magnetic moment to the lattice is also puzzling. The investigation presented here has indicated that the coupling does exist and that it can be used to align crystallographic domains within the low temperature martensitic phase. However, more work is needed before a full understanding of the transformation and low temperature properties of $Ni_{2+x}Mn_{1-x}Ga$ compounds is achieved.

Appendix A: C^{++}-program for mean field calculation

A small C^{++}-program was written to solve the self-consistent equation (3.53). The results of this calculation are shown in figures (3.8) and (3.9). The content of the program is shown next:

```
// routine to calculate magnetisation of spin 1/2 system
// in mean field approximation
//
// K. Fröhlich, Jan 2004
//
#include <conio.h>      // load header files
#include <iostream.h>
#include <math.h>

float main()
{
 float m,b,t,Mold;
 int irun,itest;

 for(t=0.0000001; t<=2.51; t=t+0.1)    // temperature loop
 {
  itest=0;
  cout<< "  t = "<< t<<endl;
  for(b=0.0001; b<=0.81; b=b+0.02)        // magnetic field loop
   {
   m=0.2;  // initialize iteration
   irun=0;
      do
      {
       Mold=m;
```

```
        m=tanh((b+m)/t);
        irun +=1;
       }while(1000000*fabs(Mold-m) > 0.00000001 || irun < 10000);
    itest+=1;
       if(itest==4)
       {
        itest=0;
         cout<<endl;
       }
    // cout<<"["<<b/m<<","<<m*m<<"],";
    cout<< "["<<b<<","<<m<<"],";
   }
  cout<<endl;
  getch();
 }
 getch();
 return(0);
}
```

Appendix B: FullProf Data files

The following pcr files have been used in the structural refinement of neutron data. The various parameters are listed according to the contributing phases. For details of their interpretation and the refinement the reader is referred to the FullProf manual (http://www-llb.cea.fr/fullweb/fp2k/fp2k.htm).

Content of the pcr file of the refinement at T = 310 K

```
COMM Ni(2.17)Mn(0.83)Ga 310K
! Current global Chi2 (Bragg contrib.) =     7.047
! Files => DAT-file: nmg7310,  PCR-file: ni217_310k_2phases
!Job Npr Nph Nba Nex Nsc Nor Dum Iwg Ilo Ias Res Ste Nre Cry Uni Cor Opt Aut
  1  5  3  0  2  0  0  1  1  0  0  0  0  0  0  0  0  0  0
!
!Ipr Ppl Ioc Mat Pcr Ls1 Ls2 Ls3 NLI Prf Ins Rpa Sym Hkl Fou Sho Ana
  0  0  1  1  1  0  0  0  0  1  6  0  0  0  0  0  0
!
! lambda1 Lambda2    Ratio   Bkpos   Wdt    Cthm    muR   AsyLim   Rpolarz ->Patt# 1
 1.590000 1.590000  1.0000   49.000 5.0000 0.0000 0.0000   50.00    0.0000
!
!NCY  Eps  R_at  R_an  R_pr  R_gl    Thmin      Step      Thmax    PSD    Sent0
 7  0.10  0.80  0.80  0.80  0.80    -7.4500    0.0500   162.0000   0.000  0.000
!
! Excluded regions (LowT  HighT) for Pattern#  1
   -100.50       8.00
    147.20     180.00
!
!
    21    !Number of refined parameters
!
! Zero    Code    Sycos    Code   Sysin    Code  Lambda     Code MORE ->Patt# 1
 0.00913  11.00  0.00000   0.00  0.00000   0.00 0.000000    0.00   0
```

```
! Background coefficients/codes for Pattern# 1
 141.67   -1.3741    37.242   -23.781    5.6990    0.0000
   41.000    51.000    61.000    71.000    81.000    0.000
!-------------------------------------------------------------------------------
! Data for PHASE number:  1 ==> Current R_Bragg for Pattern# 1:   4.18
!-------------------------------------------------------------------------------
Ni2MnGa
!
!Nat Dis Ang Pr1 Pr2 Pr3 Jbt Irf Isy Str Furth    ATZ   Nvk Npr More
  3   0   0 0.0 0.0 1.0   0   0   0   0   0     968.23   0   5   0
!
F m 3 m              <--Space group symbol
!Atom Typ      X       Y       Z     Biso      Occ     In Fin N_t Spc /Codes
Ni8c NI     0.25000 0.25000 0.25000 0.72645 0.41667  0  0  0   0
            0.00    0.00    0.00   141.00    0.00
Mn4a MN     0.00000 0.00000 0.00000 0.72645 0.07512  0  0  0   0
            0.00    0.00    0.00   141.00    0.00
Ga4b GA     0.00000 0.00000 0.50000 0.67624 0.20833  0  0  0   0
            0.00    0.00    0.00   161.00    0.00
!-------> Profile Parameters for Pattern #  1
! Scale      Shape1     Bov      Str1      Str2      Str3   Strain-Model
 0.46776E-02 -0.07087  0.00000   0.00000   0.00000   0.00000      1
   21.00000  131.000    0.000     0.000     0.000     0.000
!    U        V        W        X        Y      GauSiz  LorSiz Size-Model
  0.063270 -0.133062  0.125524  0.003270  0.000000  0.000000  0.000000   0
    91.000   101.000   111.000   121.000    0.000     0.000     0.000
!   a        b        c       alpha    beta     gamma
  5.792132  5.792132  5.792132 90.000000 90.000000 90.000000
  31.00000  31.00000  31.00000  0.00000   0.00000   0.00000
! Pref1    Pref2     Asy1     Asy2     Asy3     Asy4
 0.00000  0.00000  0.00000  0.00000  0.00000  0.00000
   0.00     0.00     0.00     0.00     0.00     0.00
!-------------------------------------------------------------------------------
! Data for PHASE number:  2 ==> Current R_Bragg for Pattern# 1:   7.45
!-------------------------------------------------------------------------------
Ni2.17Mn.83Ga
!
!Nat Dis Mom Pr1 Pr2 Pr3 Jbt Irf Isy Str Furth    ATZ   Nvk Npr More
  1   0   0 0.0 0.0 1.0  -1   0  -1   0   0       0.00   0   5   0
!
```

```
F 1                <--Space group symbol
!Nsym Cen Laue MagMat
  4  2  1  1
!
SYMM  X,Y,Z
MSYM  U,V,W, .0
SYMM  X+0.5,Y+0.5,Z
MSYM  U,V,W, .0
SYMM  X+0.5,Y,Z+0.5
MSYM  U,V,W, .0
SYMM  X,Y+0.5,Z+0.5
MSYM  U,V,W, .0
!
!Atom Typ  Mag Vek   X     Y     Z     Biso  Occ     Rm     Rphi  Rtheta
!    Im   Iphi  Itheta  beta11  beta22  beta33   MagPh
MN   MMN2  1  0  0.00000 0.00000 0.00000 0.72645 8.30000   1.536   0.000   0.000
             0.00   0.00   0.00  141.00   0.00  151.00   0.00   0.00
  0.000   0.000   0.000   0.000   0.000   0.000 0.00000
   0.00    0.00    0.00    0.00    0.00    0.00    0.00
!-------> Profile Parameters for Pattern #  1
! Scale      Shape1      Bov      Str1      Str2      Str3   Strain-Model
 0.46776E-02 -0.07087  0.00000   0.00000   0.00000   0.00000      1
   21.00000   131.000    0.000     0.000     0.000     0.000
!    U        V        W        X        Y      GauSiz   LorSiz Size-Model
  0.063270 -0.133062  0.125524  0.003270  0.000000  0.000000  0.000000   0
    91.000   101.000   111.000   121.000     0.000     0.000     0.000
!   a        b        c       alpha     beta      gamma
  5.792132  5.792132  5.792132 90.000000 90.000000 90.000000
  31.00000  31.00000  31.00000   0.00000   0.00000   0.00000
! Pref1    Pref2     Asy1     Asy2     Asy3     Asy4
 0.00000  0.00000  0.00000  0.00000  0.00000  0.00000
   0.00     0.00     0.00     0.00     0.00     0.00
!------------------------------------------------------------------------------
! Data for PHASE number:  3 ==> Current R_Bragg for Pattern#  1:   44.64
!------------------------------------------------------------------------------
Ni2MnGa
!
!Nat Dis Ang Pr1 Pr2 Pr3 Jbt Irf Isy Str Furth     ATZ   Nvk Npr More
  3   0   0 0.0 0.0 1.0   0   0   0   0   0     968.23   0   5   0
!
```

```
P n n m              <--Space group symbol
!Atom Typ     X       Y       Z     Biso      Occ    In Fin N_t Spc /Codes
Ni4f NI     0.00000 0.50000 0.25000 0.00000 0.20833  0  0  0   0
          0.00    0.00    0.00    0.00    0.00
Mn2a MN     0.00000 0.00000 0.00000 0.00000 0.00375  0  0  0   0
          0.00    0.00    0.00    0.00    0.00
Ga2b GA     0.00000 0.00000 0.50000 0.00000 0.10417  0  0  0   0
          0.00    0.00    0.00    0.00    0.00
!-------> Profile Parameters for Pattern #  1
! Scale      Shape1     Bov      Str1      Str2      Str3   Strain-Model
 0.37665     1.08098  0.03832  0.00000   0.00000   0.00000      1
  211.00000  191.000  201.000    0.000     0.000     0.000
!    U        V        W        X         Y       GauSiz   LorSiz Size-Model
  0.063270 -0.133062  0.125524  0.003270  0.000000  0.000000  0.000000   0
   91.000   101.000   111.000   121.000     0.000     0.000     0.000
!   a        b        c       alpha      beta       gamma
  3.880890  3.880890  6.436859 90.000000 90.000000 90.000000
 171.00000 171.00000 181.00000   0.00000   0.00000   0.00000
! Pref1    Pref2     Asy1     Asy2     Asy3     Asy4
 0.00000  0.00000  0.00000  0.00000  0.00000  0.00000
   0.00     0.00     0.00     0.00     0.00     0.00
```

Content of the pcr file of the refinement at T = 300 K

```
COMM Ni2MnGa 3 phase, 300K
! Current global Chi2 (Bragg contrib.) =      23.86
! Files => DAT-file: nmg7309,  PCR-file: ni217_3phases1
!Job Npr Nph Nba Nex Nsc Nor Dum Iwg Ilo Ias Res Ste Nre Cry Uni Cor Opt Aut
  1  5  4  0  2  0  0  1  1  0  0  0  0  0  0  0  0  0  0
!
!Ipr Ppl Ioc Mat Pcr Ls1 Ls2 Ls3 NLI Prf Ins Rpa Sym Hkl Fou Sho Ana
  0  0  1  1  1  0  0  0  0  1  6  0  0  0  0  0  0
!
! lambda1 Lambda2    Ratio    Bkpos    Wdt    Cthm     muR    AsyLim   Rpolarz ->Patt# 1
 1.590000 1.590000  1.0000   49.000  5.0000  0.0000  0.0000   50.00    0.0000
!
!NCY  Eps  R_at  R_an  R_pr  R_gl    Thmin      Step      Thmax     PSD    Sent0
 17 0.01  0.08  0.80  0.80  0.80    -7.4500    0.0500   162.0000   0.000   0.000
```

```
!
! Excluded regions (LowT  HighT) for Pattern#  1
   -100.50       8.00
    147.20     180.00
!
!
    33   !Number of refined parameters
!
! Zero   Code   Sycos   Code  Sysin   Code  Lambda    Code MORE ->Patt# 1
 0.00280 11.00 0.00000  0.00 0.00000  0.00 0.000000   0.00  0
!  Background coefficients/codes  for Pattern#  1
 131.89    -4.3539     32.759    -25.033     6.9738     0.0000
   131.000    141.000    151.000    161.000    171.000      0.000
!-------------------------------------------------------------------------------
! Data for PHASE number:  1  ==> Current R_Bragg for Pattern#  1:   12.10
!-------------------------------------------------------------------------------
Ni2MnGa
!
!Nat Dis Ang Pr1 Pr2 Pr3 Jbt Irf Isy Str Furth    ATZ   Nvk Npr More
  3  0   0 0.0 0.0 1.0   0   0   0   0   0     968.23   0   5   0
!
I 4/m m m             <--Space group symbol
!Atom Typ      X       Y       Z     Biso      Occ     In Fin N_t Spc /Codes
Ni4f NI     0.00000 0.50000 0.25000 0.00000 1.25000  0  0  0   0
          0.00    0.00    0.00    0.00    0.00
Mn2a MN     0.00000 0.00000 0.00000 0.00000 0.22535  0  0  0   0
          0.00    0.00    0.00    0.00    0.00
Ga2b GA     0.00000 0.00000 0.50000 0.00000 0.62500  0  0  0   0
          0.00    0.00    0.00    0.00    0.00
!-------> Profile Parameters for Pattern #  1
! Scale      Shape1      Bov      Str1      Str2      Str3   Strain-Model
0.72169E-02  0.12810  0.19531  0.00000  0.00000  0.00000      1
  21.00000  221.000  231.000    0.000    0.000    0.000
!    U        V        W        X        Y      GauSiz   LorSiz Size-Model
 0.059681 -0.127074  0.161483  0.009923  0.000000  0.000000  0.000000   0
  181.000   191.000   201.000   211.000     0.000     0.000     0.000
!   a        b        c       alpha     beta      gamma
 3.881999  3.881999  6.434086 90.000000 90.000000 90.000000
 31.00000  31.00000  41.00000   0.00000   0.00000   0.00000
! Pref1   Pref2     Asy1     Asy2     Asy3     Asy4
```

```
 0.00000  0.00000  0.07691  0.01492  0.00000  0.00000
   0.00     0.00     0.00     0.00     0.00     0.00
!------------------------------------------------------------------------------
! Data for PHASE number:  2 ==> Current R_Bragg for Pattern#  1:   15.15
!------------------------------------------------------------------------------
Ni2MnGa
!
!Nat Dis Ang Pr1 Pr2 Pr3 Jbt Irf Isy Str Furth    ATZ   Nvk Npr More
  12   0   0 0.0 0.0 1.0   0   0   0   0   0     968.23   0   5   0
!
C m m m              <--Space group symbol
!Atom Typ      X        Y        Z      Biso      Occ     In Fin N_t Spc /Codes
Ni4f NI     0.12889  0.13633  0.22615  0.00000  8.00000   0   0   0   0
            0.00     0.00     0.00     0.00     0.00
Ni4f NI     0.13519  0.38762  0.29163  0.00000  8.00000   0   0   0   0
            0.00     0.00     0.00     0.00     0.00
Mn2a MN     0.00000  0.00000  0.00000  0.00000  0.36056   0   0   0   0
            0.00     0.00     0.00     0.00     0.00
Mn2b MN     0.50000  0.00000  0.00000  0.00000  0.36056   0   0   0   0
            0.00     0.00     0.00     0.00     0.00
Mn4e MN     0.25000  0.25000  0.00000  0.00000  0.72112   0   0   0   0
            0.00     0.00     0.00     0.00     0.00
Mn4h MN     0.24142  0.00000  0.50000  0.00000  0.72112   0   0   0   0
            0.00     0.00     0.00     0.00     0.00
Mn4j MN     0.00000  0.23100  0.50000  0.00000  0.72112   0   0   0   0
            0.00     0.00     0.00     0.00     0.00
Ga2d GA     0.00000  0.00000  0.50000  0.00000  1.00000   0   0   0   0
            0.00     0.00     0.00     0.00     0.00
Ga2c GA     0.50000  0.00000  0.50000  0.00000  1.00000   0   0   0   0
            0.00     0.00     0.00     0.00     0.00
Ga4f GA     0.25000  0.25000  0.50000  0.00000  2.00000   0   0   0   0
            0.00     0.00     0.00     0.00     0.00
Ga4g GA     0.23299  0.00000  0.00000  0.00000  2.00000   0   0   0   0
            0.00     0.00     0.00     0.00     0.00
Ga4i GA     0.00000  0.28492  0.00000  0.00000  2.00000   0   0   0   0
            0.00     0.00     0.00     0.00     0.00
!-------> Profile Parameters for Pattern #  1
! Scale      Shape1      Bov      Str1      Str2      Str3   Strain-Model
 0.26616E-03  0.45309  0.52086  0.00000  0.00000  0.00000      1
   51.00000  241.000  251.000    0.000     0.000     0.000
```

```
!    U        V        W        X        Y      GauSiz  LorSiz Size-Model
  0.059681 -0.127074  0.161483  0.009923  0.000000  0.000000  0.000000   0
   181.000   191.000   201.000   211.000     0.000     0.000     0.000
! a        b        c        alpha    beta     gamma
 11.029306 11.527459  6.088085 90.000000 90.000000 90.000000
 61.00000  71.00000  81.00000   0.00000   0.00000   0.00000
! Pref1   Pref2    Asy1    Asy2    Asy3    Asy4
 0.00000 0.00000 0.00000 0.00000 0.00000 0.00000
  0.00    0.00    0.00    0.00    0.00    0.00
!-------------------------------------------------------------------------------
! Data for PHASE number:  3 ==> Current R_Bragg for Pattern# 1:   12.56
!-------------------------------------------------------------------------------
Ni2MnGa
!
!Nat Dis Ang Pr1 Pr2 Pr3 Jbt Irf Isy Str Furth    ATZ   Nvk Npr More
  9  0  0 0.0 0.0 1.0  0  0  0  0  0  0    968.23  0  5  0
!
P n n m              <--Space group symbol
!Atom Typ     X       Y       Z     Biso      Occ    In Fin N_t Spc /Codes
Ni4f NI     0.00000 0.50000 0.24836 0.00000 2.00000  0  0  0   0
          0.00    0.00  291.00    0.00    0.00
Ni8h NI    -0.00122 0.10000 0.25285 0.00000 4.00000  0  0  0   0
         301.00    0.00  311.00    0.00    0.00
Ni8h NI     0.08080 0.30000 0.24273 0.00000 4.00000  0  0  0   0
         321.00    0.00  331.00    0.00    0.00
Mn2a MN     0.00100 0.00000 0.00000 0.00000 0.36056  0  0  0   0
          0.00    0.00    0.00    0.00    0.00
Mn4g MN     0.00000 0.20000 0.00000 0.00000 0.72112  0  0  0   0
          0.00    0.00    0.00    0.00    0.00
Mn4g MN     0.00000 0.40000 0.00000 0.00000 0.72112  0  0  0   0
          0.00    0.00    0.00    0.00    0.00
Ga2b GA     0.50000 0.50000 0.00000 0.00000 1.00000  0  0  0   0
          0.00    0.00    0.00    0.00    0.00
Ga4g GA     0.50000 0.10000 0.00000 0.00000 2.00000  0  0  0   0
          0.00    0.00    0.00    0.00    0.00
Ga4g GA     0.50000 0.30000 0.00000 0.00000 2.00000  0  0  0   0
          0.00    0.00    0.00    0.00    0.00
!-------> Profile Parameters for Pattern #  1
! Scale      Shape1     Bov      Str1     Str2     Str3  Strain-Model
 0.75821E-03 -0.22072  0.69512  0.00000  0.00000  0.00000      1
```

```
   91.00000  261.000  271.000    0.000    0.000    0.000
!    U        V        W        X        Y      GauSiz  LorSiz Size-Model
  0.059681 -0.127074  0.161483  0.009923  0.000000  0.000000  0.000000   0
   181.000   191.000   201.000   211.000    0.000    0.000    0.000
!  a        b        c       alpha     beta      gamma
  4.096430 20.481590  5.789271 90.000000 90.000000 90.000000
 101.00000 111.00000 121.00000   0.00000   0.00000   0.00000
! Pref1   Pref2    Asy1    Asy2    Asy3    Asy4
 0.00000 0.00000 0.00000 0.00000 0.00000 0.00000
   0.00    0.00    0.00    0.00    0.00    0.00
!-------------------------------------------------------------------------------
! Data for PHASE number:  4 ==> Current R_Bragg for Pattern#  1:   13.89
!-------------------------------------------------------------------------------
Ni2.17Mn.83Ga
!
!Nat Dis Mom Pr1 Pr2 Pr3 Jbt Irf Isy Str Furth    ATZ   Nvk Npr More
  1  0   0 0.0 0.0 1.0  -1   0  -1   0   0       0.00   0   5   0
!
P 1                <--Space group symbol
!Nsym Cen Laue MagMat
  2  2  1  1
!
SYMM  -X,-Y,-Z
MSYM  U,V,W, .0
SYMM  -X+0.5,-Y+0.5,-Z+0.5
MSYM  U,V,W, .0
!
!Atom Typ  Mag Vek   X     Y     Z     Biso  Occ     Rm     Rphi  Rtheta
!   Im   Iphi  Itheta  beta11  beta22  beta33  MagPh
MN   MMN2  1  0  0.00000 0.00000 0.00000 0.00000 8.30000   2.906   0.000  90.000
             0.00    0.00    0.00    0.00    0.00  281.00    0.00    0.00
  0.000   0.000   0.000   0.000   0.000   0.000 0.00000
   0.00    0.00    0.00    0.00    0.00    0.00    0.00
!-------> Profile Parameters for Pattern #  1
! Scale      Shape1      Bov      Str1      Str2      Str3   Strain-Model
0.72169E-02  0.12810  0.64255  0.00000  0.00000  0.00000      1
  21.00000  221.000  231.000    0.000    0.000    0.000
!    U        V        W        X        Y      GauSiz  LorSiz Size-Model
  0.059681 -0.127074  0.161483  0.009923  0.000000  0.000000  0.000000   0
   181.000   191.000   201.000   211.000    0.000    0.000    0.000
```

```
!   a        b        c       alpha     beta      gamma
  3.881999  3.881999  6.434086 90.000000 90.000000 90.000000
  31.00000  31.00000  41.00000  0.00000  0.00000  0.00000
! Pref1   Pref2    Asy1    Asy2    Asy3    Asy4
 0.00000 0.00000 0.07691 0.01492 0.00000 0.00000
   0.00    0.00    0.00    0.00    0.00    0.00
```

Content of the pcr file of the refinement at T = 250 K

```
COMM Ni(2.17)Mn(0.83)Ga T=250K
! Current global Chi2 (Bragg contrib.) =     8.895
! Files => DAT-file: Ni2P17_250,  PCR-file: ni217_250k_2phases
!Job Npr Nph Nba Nex Nsc Nor Dum Iwg Ilo Ias Res Ste Nre Cry Uni Cor Opt Aut
  1  5  3  0  2  0  0  1  1  0  0  0  0  0  0  0  0  0  0
!
!Ipr Ppl Ioc Mat Pcr Ls1 Ls2 Ls3 NLI Prf Ins Rpa Sym Hkl Fou Sho Ana
  0  0  1  1  1  0  0  0  0  1  6  0  0  0  0  0  0
!
! lambda1 Lambda2   Ratio   Bkpos   Wdt   Cthm    muR   AsyLim   Rpolarz ->Patt# 1
 1.590000 1.590000  1.0000   59.000 5.0000 0.0000 0.0000   55.00    0.0000
!
!NCY  Eps  R_at  R_an  R_pr  R_gl    Thmin      Step      Thmax    PSD    Sent0
 17 0.01  0.18  0.80  0.80  0.80    -7.4500    0.0500   162.0000  0.000  0.000
!
! Excluded regions (LowT  HighT) for Pattern#  1
    -100.50       8.00
     145.20     180.00
!
!
    36   !Number of refined parameters
!
! Zero   Code   Sycos   Code  Sysin   Code  Lambda    Code MORE ->Patt# 1
 0.01770  11.00  0.00000   0.00  0.00000   0.00 0.000000   0.00   0
!  Background coefficients/codes  for Pattern#  1
 135.93     2.4269    -19.289    -4.2098     76.360    -42.542
   131.000    141.000    151.000    161.000    171.000    181.000
!-------------------------------------------------------------------------------
! Data for PHASE number:  1  ==> Current R_Bragg for Pattern#  1:    4.24
!-------------------------------------------------------------------------------
```

```
Ni2MnGa
!
!Nat Dis Ang Pr1 Pr2 Pr3 Jbt Irf Isy Str Furth    ATZ   Nvk Npr More
  3   0   0 0.0 0.0 1.0   0   0   0   0   0   0     968.23   0   5   0
!
I 4/m m m              <--Space group symbol
!Atom Typ      X       Y       Z      Biso      Occ     In Fin N_t Spc /Codes
Ni4f NI     0.00000 0.50000 0.25000 0.00000 1.25000  0  0  0   0
            0.00    0.00    0.00    0.00    0.00
Mn2a MN     0.00000 0.00000 0.00000 0.00000 0.22535  0  0  0   0
            0.00    0.00    0.00    0.00    0.00
Ga2b GA     0.00000 0.00000 0.50000 0.00000 0.62500  0  0  0   0
            0.00    0.00    0.00    0.00    0.00
!-------> Profile Parameters for Pattern #  1
! Scale      Shape1      Bov      Str1      Str2      Str3   Strain-Model
 0.16294E-01  0.28955  0.27791  0.00000  0.00000  0.00000      1
  21.00000  201.000  191.000    0.000    0.000    0.000
!    U        V        W        X        Y      GauSiz   LorSiz Size-Model
  0.103768 -0.149351  0.156234  0.005421  0.000000  0.000000  0.000000   0
   241.000   251.000   261.000   211.000     0.000     0.000     0.000
!   a        b        c       alpha    beta     gamma
  3.868827  3.868827  6.466137 90.000000 90.000000 90.000000
  31.00000  31.00000  41.00000   0.00000   0.00000   0.00000
! Pref1    Pref2     Asy1     Asy2     Asy3     Asy4
 0.00000  0.00000  0.07689  0.01492  0.00000  0.00000
   0.00     0.00   111.00   121.00     0.00     0.00
!------------------------------------------------------------------------------
! Data for PHASE number:  2 ==> Current R_Bragg for Pattern#  1:    4.23
!------------------------------------------------------------------------------
Ni2.17Mn.83Ga
!
!Nat Dis Mom Pr1 Pr2 Pr3 Jbt Irf Isy Str Furth    ATZ   Nvk Npr More
  1   0   0 0.0 0.0 1.0  -1   0  -1   0   0       0.00   0   5   0
!
I 1                    <--Space group symbol
!Nsym Cen Laue MagMat
  4   2   1   1
!
SYMM  X,Y,Z
MSYM  U,V,W, .0
```

```
SYMM -X+0.5,Y+0.5,-Z+0.5
MSYM U,V,W, .0
SYMM -X,-Y,Z
MSYM U,V,W, .0
SYMM X+0.5,-Y+0.5,-Z+0.5
MSYM U,V,W, .0
!
!Atom Typ  Mag Vek   X     Y     Z     Biso  Occ     Rm     Rphi  Rtheta
!    Im   Iphi  Itheta beta11 beta22 beta33  MagPh
MN   MMN2  1  0  0.00000 0.00000 0.00000 0.00000 4.15000  2.047  0.000  0.000
             0.00   0.00   0.00   0.00   0.00  51.00   0.00   0.00
  0.000  0.000  0.000  0.000  0.000  0.000 0.00000
   0.00   0.00   0.00   0.00   0.00   0.00   0.00
!-------> Profile Parameters for Pattern #  1
! Scale      Shape1     Bov     Str1     Str2     Str3  Strain-Model
 0.16294E-01  0.28955  0.27791  0.00000  0.00000  0.00000     1
   21.00000  201.000  191.000    0.000    0.000    0.000
!    U        V        W        X        Y      GauSiz   LorSiz Size-Model
  0.103768 -0.149351  0.156234  0.005421  0.000000  0.000000  0.000000   0
   241.000   251.000   261.000   211.000    0.000    0.000    0.000
!   a        b        c       alpha    beta     gamma
  3.868827  3.868827  6.466137 90.000000 90.000000 90.000000
  31.00000  31.00000  41.00000   0.00000   0.00000   0.00000
! Pref1    Pref2     Asy1     Asy2     Asy3     Asy4
 0.00000  0.00000  0.07689  0.01492  0.00000  0.00000
   0.00     0.00   111.00   121.00     0.00     0.00
!------------------------------------------------------------------------------
! Data for PHASE number:  3 ==> Current R_Bragg for Pattern#  1:   11.39
!------------------------------------------------------------------------------
Ni2MnGa
!
!Nat Dis Ang Pr1 Pr2 Pr3 Jbt Irf Isy Str Furth     ATZ   Nvk Npr More
 12   0   0 0.0 0.0 1.0   0   0   0   0   0     968.23   0   5   0
!
C m m m              <--Space group symbol
!Atom Typ      X       Y       Z     Biso      Occ     In Fin N_t Spc /Codes
Ni4f NI     0.12889 0.13633 0.22615 0.00000 8.00000  0  0  0   0
          331.00  291.00  311.00    0.00    0.00
Ni4f NI     0.13519 0.38762 0.29163 0.00000 8.00000  0  0  0   0
          341.00  301.00  321.00    0.00    0.00
```

```
Mn2a MN     0.00000 0.00000 0.00000 0.00000 0.36056  0  0  0   0
          0.00    0.00    0.00    0.00    0.00
Mn2b MN     0.50000 0.00000 0.00000 0.00000 0.36056  0  0  0   0
          0.00    0.00    0.00    0.00    0.00
Mn4e MN     0.25000 0.25000 0.00000 0.00000 0.72112  0  0  0   0
          0.00    0.00    0.00    0.00    0.00
Mn4h MN     0.24142 0.00000 0.50000 0.00000 0.72112  0  0  0   0
         101.00    0.00    0.00    0.00    0.00
Mn4j MN     0.00000 0.23100 0.50000 0.00000 0.72112  0  0  0   0
          0.00  271.00    0.00    0.00    0.00
Ga2d GA     0.00000 0.00000 0.50000 0.00000 1.00000  0  0  0   0
          0.00    0.00    0.00    0.00    0.00
Ga2c GA     0.50000 0.00000 0.50000 0.00000 1.00000  0  0  0   0
          0.00    0.00    0.00    0.00    0.00
Ga4f GA     0.25000 0.25000 0.50000 0.00000 2.00000  0  0  0   0
          0.00    0.00    0.00    0.00    0.00
Ga4g GA     0.23299 0.00000 0.00000 0.00000 2.00000  0  0  0   0
        351.00    0.00    0.00    0.00    0.00
Ga4i GA     0.00000 0.28492 0.00000 0.00000 2.00000  0  0  0   0
          0.00  361.00    0.00    0.00    0.00
!-------> Profile Parameters for Pattern #  1
! Scale      Shape1     Bov     Str1     Str2     Str3  Strain-Model
 0.11076E-03  0.72047  0.14238  0.00000  0.00000  0.00000     1
   61.00000  221.000  231.000    0.000    0.000    0.000
!    U        V        W        X        Y      GauSiz  LorSiz Size-Model
  0.103768 -0.149351  0.156234  0.005421  0.000000  0.090291  0.000000   0
   241.000   251.000   261.000   211.000    0.000   281.000    0.000
!  a        b        c       alpha    beta     gamma
 10.993261 11.508169  6.082433 90.000000 90.000000 90.000000
  71.00000  81.00000  91.00000   0.00000   0.00000   0.00000
! Pref1   Pref2    Asy1    Asy2    Asy3    Asy4
 0.00000 0.00000 0.07689 0.01492 0.00000 0.00000
   0.00    0.00  111.00  121.00    0.00    0.00
```

Appendix C: Structural Relationships between various phases

The relationship between possible phases have been studied in an attempt to systematically evaluate their potential for explaining details of the observed diffraction patterns.

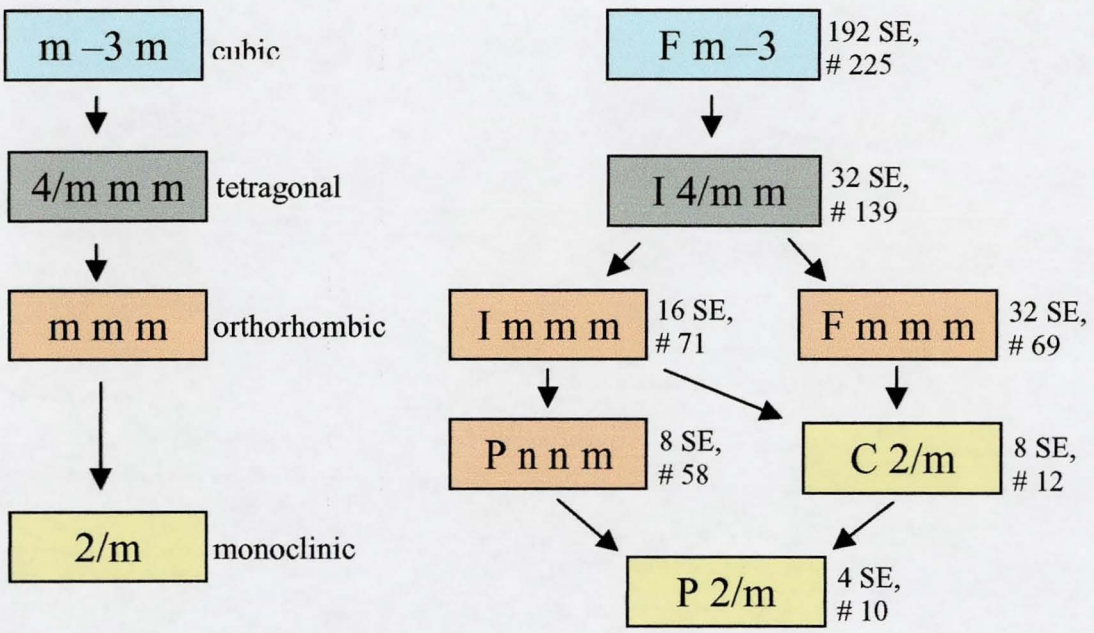

The position of atoms of the Heusler structure in unconventional setting of various space groups and unit cells

Here the position of atoms are discussed when the description is transformed from the conventional Heusler structure to a different space group. This transformation is relevant for structure determinations such as the one which is of interest here for the various phases of $Ni_{2.17}Mn_{0.83}Ga$.

The Heusler structure can be described using the space group symbol $Fm\bar{3}m$. The number behind the space group symbol is the number according to [International Tables For Crystallography, volume A, Space Group Symmetry: Theo Hahn (editor), D. Reidel Publishing Company, 2nd edition, 1987].

A comment is given in brackets there in order to identify particular features of the chosen unit cell. This is followed by a graphical representation of the relationships between the various space groups. Only those space groups have been considered which might be of relevance for structural transformation.

F m –3 m #225 (no increase along any axis):

Mn	4a	$(0,0,0)$	$\left(0,\frac{1}{2},\frac{1}{2}\right)$	$\left(\frac{1}{2},0,\frac{1}{2}\right)$	$\left(\frac{1}{2},\frac{1}{2},0\right)$
Ga	4b	$\left(\frac{1}{2},\frac{1}{2},\frac{1}{2}\right)$	$\left(\frac{1}{2},0,0\right)$	$\left(0,\frac{1}{2},0\right)$	$\left(0,0,\frac{1}{2}\right)$
Ni	8c	$\left(\frac{1}{4},\frac{1}{4},\frac{1}{4}\right)$	$\left(\frac{1}{4},\frac{1}{4},\frac{3}{4}\right)$	$\left(\frac{1}{4},\frac{3}{4},\frac{1}{4}\right)$	$\left(\frac{1}{4},\frac{3}{4},\frac{3}{4}\right)$
		$\left(\frac{3}{4},\frac{1}{4},\frac{1}{4}\right)$	$\left(\frac{3}{4},\frac{1}{4},\frac{3}{4}\right)$	$\left(\frac{3}{4},\frac{3}{4},\frac{1}{4}\right)$	$\left(\frac{3}{4},\frac{3}{4},\frac{3}{4}\right)$

F m m m #69 (3-fold increase along b-axis):

Mn	4a	$(0,0,0)$	$\left(0,\frac{1}{2},\frac{1}{2}\right)$	$\left(\frac{1}{2},0,\frac{1}{2}\right)$	$\left(\frac{1}{2},\frac{1}{2},0\right)$
	8h	$\left(0,\frac{1}{3},0\right)$	$\left(0,\frac{2}{3},0\right)$	$\left(\frac{1}{2},\frac{5}{6},0\right)$	$\left(\frac{1}{2},\frac{1}{6},0\right)$
		$\left(0,\frac{1}{6},\frac{1}{2}\right)$	$\left(0,\frac{5}{6},\frac{1}{2}\right)$	$\left(\frac{1}{2},\frac{2}{3},\frac{1}{2}\right)$	$\left(\frac{1}{2},\frac{2}{3},\frac{1}{2}\right)$
Ga	4b	$\left(\frac{1}{2},\frac{1}{2},\frac{1}{2}\right)$	$\left(\frac{1}{2},0,0\right)$	$\left(0,\frac{1}{2},0\right)$	$\left(0,0,\frac{1}{2}\right)$
	8h	$\left(\frac{1}{2},\frac{1}{6},\frac{1}{6}\right)$	$\left(\frac{1}{2},\frac{1}{6},0\right)$	$\left(0,\frac{1}{6},0\right)$	$\left(0,\frac{1}{6},\frac{1}{2}\right)$
		$\left(\frac{1}{2},\frac{5}{6},\frac{1}{2}\right)$	$\left(\frac{1}{2},\frac{5}{6},0\right)$	$\left(0,\frac{5}{6},0\right)$	$\left(0,\frac{5}{6},\frac{1}{2}\right)$
Ni	8f	$\left(\frac{1}{4},\frac{1}{4},\frac{1}{4}\right)$	$\left(\frac{1}{4},\frac{1}{4},\frac{3}{4}\right)$	$\left(\frac{1}{4},\frac{3}{4},\frac{1}{4}\right)$	$\left(\frac{1}{4},\frac{3}{4},\frac{3}{4}\right)$
		$\left(\frac{3}{4},\frac{1}{4},\frac{1}{4}\right)$	$\left(\frac{3}{4},\frac{1}{4},\frac{3}{4}\right)$	$\left(\frac{3}{4},\frac{3}{4},\frac{1}{4}\right)$	$\left(\frac{3}{4},\frac{3}{4},\frac{3}{4}\right)$
	16k	$\left(\frac{1}{4},\frac{1}{12},\frac{1}{4}\right)$	$\left(\frac{1}{4},\frac{1}{12},\frac{3}{4}\right)$	$\left(\frac{1}{4},\frac{11}{12},\frac{1}{4}\right)$	$\left(\frac{1}{4},\frac{11}{12},\frac{3}{4}\right)$

$\left(\frac{1}{4},\frac{7}{12},\frac{1}{4}\right)$ $\left(\frac{1}{4},\frac{7}{12},\frac{3}{4}\right)$ $\left(\frac{1}{4},\frac{5}{12},\frac{1}{4}\right)$ $\left(\frac{1}{4},\frac{5}{12},\frac{3}{4}\right)$

$\left(\frac{3}{4},\frac{1}{12},\frac{3}{4}\right)$ $\left(\frac{3}{4},\frac{1}{12},\frac{1}{4}\right)$ $\left(\frac{3}{4},\frac{11}{12},\frac{3}{4}\right)$ $\left(\frac{3}{4},\frac{11}{12},\frac{1}{4}\right)$

$\left(\frac{3}{4},\frac{7}{12},\frac{1}{4}\right)$ $\left(\frac{3}{4},\frac{7}{12},\frac{3}{4}\right)$ $\left(\frac{3}{4},\frac{5}{12},\frac{1}{4}\right)$ $\left(\frac{3}{4},\frac{5}{12},\frac{3}{4}\right)$

I 4/m m m #139 (no increase along any axis):

Mn 2a $(0,0,0)$ $\left(\frac{1}{2},\frac{1}{2},\frac{1}{2}\right)$

Ga 2b $\left(0,0,\frac{1}{2}\right)$ $\left(\frac{1}{2},\frac{1}{2},0\right)$

Ni 4d $\left(0,\frac{1}{2},\frac{1}{4}\right)$ $\left(0,\frac{1}{2},\frac{3}{4}\right)$ $\left(\frac{1}{2},0,\frac{1}{4}\right)$ $\left(\frac{1}{2},0,\frac{3}{4}\right)$

I m m m #71 (3-fold increase along b-axis):

Mn	2a	$(0,0,0)$	$\left(\frac{1}{2},\frac{1}{2},\frac{1}{2}\right)$		
	4g	$\left(0,\frac{1}{3},0\right)$	$\left(0,\frac{2}{3},0\right)$	$\left(\frac{1}{2},\frac{5}{6},\frac{1}{2}\right)$	$\left(\frac{1}{2},\frac{1}{6},\frac{1}{2}\right)$
Ga	2c	$\left(0,0,\frac{1}{2}\right)$	$\left(\frac{1}{2},\frac{1}{2},0\right)$		
	4h	$\left(0,\frac{1}{3},\frac{1}{2}\right)$	$\left(0,\frac{2}{3},\frac{1}{2}\right)$	$\left(\frac{1}{2},\frac{5}{6},0\right)$	$\left(\frac{1}{2},\frac{1}{6},0\right)$
Ni	4j	$\left(0,\frac{1}{2},\frac{1}{4}\right)$	$\left(0,\frac{1}{2},\frac{3}{4}\right)$	$\left(\frac{1}{2},0,\frac{1}{4}\right)$	$\left(\frac{1}{2},0,\frac{3}{4}\right)$
	8l	$\left(0,\frac{1}{6},\frac{1}{4}\right)$	$\left(0,\frac{1}{6},\frac{3}{4}\right)$	$\left(0,\frac{5}{6},\frac{1}{4}\right)$	$\left(0,\frac{5}{6},\frac{3}{4}\right)$
		$\left(\frac{1}{2},\frac{2}{3},\frac{1}{4}\right)$	$\left(\frac{1}{2},\frac{2}{3},\frac{3}{4}\right)$	$\left(\frac{1}{2},\frac{1}{3},\frac{1}{4}\right)$	$\left(\frac{1}{2},\frac{2}{3},\frac{3}{4}\right)$

P n n m #58 (3-fold increase along b-axis):

Mn	2a	$(0,0,0)$	$\left(\frac{1}{2},\frac{1}{2},\frac{1}{2}\right)$			
	4g	$\left(0,\frac{1}{3},0\right)$	$\left(0,\frac{2}{3},0\right)$	$\left(\frac{1}{2},\frac{5}{6},\frac{1}{2}\right)$	$\left(\frac{1}{2},\frac{1}{6},\frac{1}{2}\right)$	
Ga	2b	$\left(0,0,\frac{1}{2}\right)$	$\left(\frac{1}{2},\frac{1}{2},0\right)$			
	4g	$\left(0,\frac{1}{3},\frac{1}{2}\right)$	$\left(0,\frac{2}{3},\frac{1}{2}\right)$	$\left(\frac{1}{2},\frac{5}{6},0\right)$	$\left(\frac{1}{2},\frac{1}{6},0\right)$	
Ni	4f	$\left(0,\frac{1}{2},\frac{1}{4}\right)$	$\left(0,\frac{1}{2},\frac{3}{4}\right)$	$\left(\frac{1}{2},0,\frac{1}{4}\right)$	$\left(\frac{1}{2},0,\frac{3}{4}\right)$	
	8h	$\left(0,\frac{1}{6},\frac{1}{4}\right)$	$\left(0,\frac{1}{6},\frac{3}{4}\right)$	$\left(0,\frac{5}{6},\frac{1}{4}\right)$	$\left(0,\frac{5}{6},\frac{3}{4}\right)$	
		$\left(\frac{1}{2},\frac{2}{3},\frac{1}{4}\right)$	$\left(\frac{1}{2},\frac{2}{3},\frac{3}{4}\right)$	$\left(\frac{1}{2},\frac{1}{3},\frac{1}{4}\right)$	$\left(\frac{1}{2},\frac{2}{3},\frac{3}{4}\right)$	

P m m m #47 (2-fold increase along b-axis):

Mn	1a	$(0,0,0)$			
	1e	$\left(0,\frac{1}{2},0\right)$			
	2p	$\left(\frac{1}{2},\frac{1}{4},\frac{1}{2}\right)$	$\left(\frac{1}{2},\frac{3}{4},\frac{1}{2}\right)$		
Ga	1c	$\left(0,0,\frac{1}{2}\right)$			
	1g	$\left(0,\frac{1}{2},\frac{1}{2}\right)$			
	2o	$\left(\frac{1}{2},\frac{1}{4},0\right)$	$\left(\frac{1}{2},\frac{3}{4},0\right)$		
Ni	2s	$\left(\frac{1}{2},0,\frac{1}{4}\right)$	$\left(\frac{1}{2},0,\frac{3}{4}\right)$		
	2t	$\left(\frac{1}{2},\frac{1}{2},\frac{1}{4}\right)$	$\left(\frac{1}{2},\frac{1}{2},\frac{3}{4}\right)$		
	4u	$\left(0,\frac{1}{4},\frac{1}{4}\right)$	$\left(0,\frac{1}{4},\frac{3}{4}\right)$	$\left(0,\frac{3}{4},\frac{1}{4}\right)$	$\left(0,\frac{3}{4},\frac{3}{4}\right)$

Acknowledgement

I wish to thank my supervisor Professor Kurt Ziebeck for his enthusiastic and untiring support during the various stages of the project. His encouragement has been vital for ensuring steady progress and the timely completion of the project. I also wish to thank Bryan Dennis for his excellent technical support and Maureen McKenzie for being the 'angel' of the Physics Department.

My thanks also extends to my fellow students Özhan Ünverdi, Tamsin Stevens, Yang Yu, Nina Steinke, Julia Rasch and Stefan Becker. It has been a pleasure having them around and enjoying various discussions.

I am grateful for the hospitality of the Department of Physics and the opportunity for carrying out the scientific work at Loughborough. I wish to thank all members of the Physics Department.

My sincere thanks also goes to the 'Friedrich Naumann Stiftung' who enabled me to embark on this endeavour. I am grateful for their financial support as well as for providing me with the framework for pursuing my interests also beyond the field of science.

My friend, mentor and 'Vertrauensdozent' Jörg Röseler has been a constant source of inspiration. He has accompanied my progression with advice and encouragement. I wish to thank him for believing in me.

In particular, I wish to thank a fellow student of the 'Friedrich Naumann Stiftung', Tilmann Hickel, for being a friend. His advice and support was always very helpful.

Last but not least I wish to thank my family. They have believed in me all the time and have provided continuous encouragement throughout.

And finally I wish to thank Klaus for being my friend and for teaching me a lot of physics.